Title

A Sparse Orthogonal Collimator for Small Animal Intensity Modulated Radiation Therapy Using Rectangular Aperture Optimization

Author

Woods, Kaley Elizabeth

Publication Date

2019

Peer reviewed|Thesis/dissertation

UNIVERSITY OF CALIFORNIA

Los Angeles

A Sparse Orthogonal Collimator for Small Animal Intensity Modulated Radiation Therapy Using Rectangular Aperture Optimization

A dissertation submitted in partial satisfaction of the

requirements for the degree Doctor of Philosophy

in Biomedical Physics

by

Kaley Elizabeth Woods

2019

ABSTRACT OF THE DISSERTATION

A Sparse Orthogonal Collimator for Small Animal Intensity Modulated Radiation Therapy Using Rectangular Aperture Optimization

by

Kaley Elizabeth Woods

Doctor of Philosophy in Biomedical Physics

University of California, Los Angeles, 2019

Professor Ke Sheng, Chair

To achieve more translatable preclinical research results, small animal irradiation needs to more closely simulate human radiation therapy. Although the clinical gold standard is intensity modulated radiation therapy (IMRT), the direct translation of this method for small animals is impractical. To address this challenge, the Sparse Orthogonal Collimator (SOC), a dose-modulating device based on the novel Rectangular Aperture Optimization (RAO) approach, was developed to deliver IMRT on the small animal scale using an image-guided small animal irradiator.

A treatment planning system was developed based on RAO, and several planning experiments were performed for evaluation. RAO achieved highly conformal doses to concave and complex targets, with SOC-based plans achieving superior dosimetry to those optimized for a hypothetical miniature multileaf collimator. Beam commissioning data, including output factors, off-axis factors, and percent depth dose curves, were acquired for our small animal irradiator and incorporated into the treatment planning system. A plan post-processing step was implemented for aperture-size-specific dose recalculation and aperture weighting reoptimization.

The SOC system, with four orthogonal, double-focused tungsten leaf pairs, was designed and fabricated, and control software was developed. The SOC was installed on the small animal irradiator and the alignment was evaluated, with submillimeter shifts measured between the SOC and primary collimator axes over the full gantry rotation. Abutting field and grid dose patterns were created to analyze leaf positioning error, with measured deviations within recommended guidelines. Extremely low leaf transmission was measured, and penumbra was independent of leaf position. Three RAO IMRT plans were delivered and analyzed, with good agreement between the intended and measured dose distributions.

By using advanced optimization techniques, complex IMRT plans were achieved using a simple dose modulation device. The sparse orthogonal collimator was developed and commissioned, with promising preliminary dosimetry results. This platform considerably reduces the gap in treatment plan quality between clinical and preclinical radiotherapy, potentially improving the translation of small animal research results.

The dissertation of Kaley Elizabeth Woods is approved.

Keisuke Steven Iwamoto

Dan Ruan

Erik Tryggestad

Ke Sheng, Committee Chair

University of California, Los Angeles

2019

To Mom, Dad, and Kris

TABLE OF CONTENTS

LIST OF TABLES IX

LIST OF FIGURES X

LIST OF EQUATIONS XV

ACKNOWLEDGEMENTS XVI

VITA XVII

1 INTRODUCTION 1

1.1 4π RADIOTHERAPY 2

1.2 PRECLINICAL RADIOTHERAPY 3

1.3 OVERVIEW 4

2 4Π RADIOTHERAPY 7

2.1 VIABILITY OF NONCOPLANAR VMAT FOR LIVER SBRT COMPARED WITH COPLANAR VMAT AND BEAM ORIENTATION OPTIMIZED 4π IMRT[26] 7

2.1.1 Introduction 7

2.1.2 Methods 8

2.1.3 Results 15

2.1.4 Discussion 21

2.1.5 Conclusions 24

2.2 COCHLEA-SPARING ACOUSTIC NEUROMA TREATMENT WITH 4π RADIATION THERAPY[27] 25

2.2.1 Introduction 25

2.2.2 Methods 27

2.2.3 Results 33

2.2.4 Discussion 37

2.2.5 Conclusions 40

2.3 4π PLAN OPTIMIZATION FOR CORTICAL-SPARING BRAIN RADIOTHERAPY[28] 41

2.3.1 Introduction 41

2.3.2 Methods 42

2.3.3 Results 44

2.3.4 Discussion 47

2.3.5 Conclusions 48

3 DOSIMETRIC EVALUATION TOOLS FOR PRECLINICAL RADIOTHERAPY 49
3.1 SMALL ANIMAL IRRADIATION STANDARDIZATION PROJECT 49
3.1.1 Introduction 49
3.1.2 Methods 50
3.1.3 Results and Discussion 56
3.1.4 Conclusions 59
3.2 A 3D PRINTED, CT-GENERATED MONKEY PHANTOM WITH TISSUE AND BONE EQUIVALENT MATERIALS 60
3.2.1 Introduction 60
3.2.2 Methods 60
3.2.3 Results 62
3.2.4 Discussion 64
3.2.5 Conclusions 64
4 SOC PLANNING SYSTEM DEVELOPMENT AND COMMISSIONING 66
4.1 INTRODUCTION 66
4.2 METHODS 69
4.2.1 Rectangular Aperture Optimization 69
4.2.2 RAO Evaluation 71
4.2.3 Beam Commissioning Measurements 73
4.2.4 Plan Post-Processing 76
4.3 RESULTS 78
4.3.1 RAO Plan Analysis 78
4.3.2 Beam Commissioning 81
4.3.3 Dose Recalculation 85
4.4 DISCUSSION 87
4.5 CONCLUSIONS 90
5 SOC HARDWARE DEVELOPMENT AND COMMISSIONING 91
5.1 INTRODUCTION 91
5.2 METHODS 93
5.2.1 SOC Design 93

5.2.2 SOC Fabrication *97*
5.2.3 SOC Control Software *99*
5.2.4 SOC Installation *100*
5.2.5 SOC Commissioning Measurements *103*
5.2.6 Dosimetric Testing *105*
5.3 RESULTS 107
5.3.1 SOC Commissioning *107*
5.3.2 Dosimetric Testing *112*
5.4 DISCUSSION 115
5.5 CONCLUSIONS 120
6 REFERENCES 121

LIST OF TABLES

Table 2-1 Patient Data 9

Table 2-2 Average dose statistics for coplanar VMAT, noncoplanar VMAT, and 4π plans for all 20 patients (HI: homogeneity index, CN: conformation number) 16

Table 2-3 Biological modeling parameter results for cVMAT, nVMAT, and 4π plans for all 20 patients (standard deviation in parentheses) 19

Table 2-4 Dose escalation based on the normal liver effective volume and desired normal liver LKB NTCP for all 20 patients (standard deviation in parentheses) 20

Table 2-5 Patient data 28

Table 2-6 TCP and NTCP model parameters 32

Table 2-7 OAR doses and conformity measures for both plan types 34

Table 2-8 Results of the radiobiological modeling and dose escalation study 36

Table 2-9 Dose statistics for clinical and 4π plans for the 15 high-grade glioma patients in this study 45

Table 3-1 Energy correction factors for TLD, OSLD, and EBT3 film measurements 55

Table 4-1 SmART system beam commissioning measurement parameters 75

Table 4-2 Dose evaluation metrics for the mouse test cases (R50: 50% dose spillage; CN: Conformation Number) 79

Table 4-3 Simplified off-axis factor measurements for 1, 2.5, and 5 mm square SOC fields on the SmART system, averaged over nine equal regions for comparison 83

Table 4-4 Field flatness for a 40 mm square field on the SmART system 85

Table 4-5 Error comparison for plans optimized with different dose calculation spectra 86

Table 5-1 SOC test plan parameters 106

Table 5-2 Leaf positioning accuracy and repeatability measurements 109

Table 5-3 SOC leaf transmission and penumbra measurements 111

Table 5-4 Comparisons between the measured and intended dose distributions for the C-shaped target plan and the mouse phantom whole liver plan[a] 114

LIST OF FIGURES

Figure 2-1 Beam geometry comparison for a typical liver SBRT case. Beam orientation is shown for the coplanar VMAT plan (left), 3 to 4 noncoplanar partial arcs (center) and 20 noncoplanar, optimized beams (right). 12

Figure 2-2 Individual patient dosimetric results comparison between cVMAT, nVMAT, and 4π static. 17

Figure 2-3 (Top) Dose-volume histograms for a typical liver SBRT case. (Bottom) Dose color washes for each plan type. The orange contours represent the PTV volume and the blue represent the 50% isodose lines. 18

Figure 2-4 Average survival predicted with the model from Tai et al[49] for the maximum tolerable doses yielding 1%, 5%, and 10% normal liver NTCPs. All fractions for nVMAT and cVMAT were significantly different than 4π static at the 5% significance level (paired, 2-tailed t-test). 21

Figure 2-5 Examples of typical beam orientations for the clinical plans with 7 to 11 static beams (left), clinical plans with 2 to 5 arcs (middle), and 4π plans with 20 static beams (right). From Table 2-5, these are patients 16, 4, and 1, respectively. 30

Figure 2-6 Mean (top) and maximum (bottom) doses to the cochlea (SRS, SRT, and IMRT groups), brainstem, and chiasm with the 4π plans (red) and clinical plans (blue). All differences between the 4π and clinical plans were statistically significant (2-tailed t-test, 5% significance level), except the maximum dose to the chiasm. 34

Figure 2-7 Dose color wash for a patient (patient 3 in Table 2-5) who was treated to a prescription dose of 12 Gy in a single fraction. Structures: PTV (blue), brainstem (green), and cochlea (red). 35

Figure 2-8 Dose volume histograms (solid line: clinical plan; dashed line: 4π plan) for one of the patients who received SRS in this study (patient 2 in Table 2-5) with a prescription dose of 12 Gy. 37

Figure 2-9 A representation of the cortical surface from Karunamuni et al[90] showing the dose delivered (A) and the extent of cortical thinning one year post-irradiation (B) for an example patient. 41

Figure 2-10 Orientation of the beams used in the clinical IMRT plan (left) and the 20 optimal beams selected by the 4π algorithm (right) for one patient in the study. 44

Figure 2-11 Dose volume histograms of the 4π (dashed) and clinical (solid) plans for the patient in Figure 2-10. 46

Figure 2-12 Dose washes of the 4π and clinical plans for the patient in Figure 2-10. Structures: 54 Gy PTV (green), 60 Gy PTV (blue), and cerebral cortex (gray). 46

Figure 2-13 Dose volume histograms of the cortex and PTV (60 Gy prescription level) for the 4π (dashed) and clinical (solid) plans averaged over all 15 patients. 47

Figure 3-1 Photograph (left) and CT scan (right: coronal view of the lower (A) and upper (B) phantom halves; axial view through the lungs (C)) of the cylindrical polystyrene mouse phantoms, with higher density inserts in the spine and legs and lower density foam inserts in the lungs. It has groups of three TLD slots in the head, spine, left and right abdomen, and pelvis. Custom die-cut film is inserted between the two halves. 50

Figure 3-2 CAD models of the full mousemorphic phantom with dimensions (upper left) and the design variations for TLD, OSLD, and Alanine dosimetry. 52

Figure 3-3 Phantoms 3D printed out of ABS from the CAD model shown in Figure 3-2. The weight of the phantom is 24.5 ± 0.1 g. 52

Figure 3-4 Monte Carlo dose calculation in the SmART-ATP system assuming tissue equivalence (left) and measured phantom film dose (right). 53

Figure 3-5 Film measurement from one of the cylindrical mouse phantoms. Average dose was measured within the four regions indicated by red squares. 56

Figure 3-6 Dosimetric harmonization test results. Measured dose is given as the average dose from the four regions-of-interest of the cylindrical phantom film (as shown in Figure 3-5) with error bars indicating the standard deviation. Irradiators #6 and #8 did not participate in the first survey, and the harmonization result of #3 was not valid. The exposure parameter for #5 was not adjusted. 57

Figure 3-7 CAD model of the portable phantom developed for beam energy spectrum characterization. Each region of the phantom has the same thickness of plastic (left), above four different thickness of copper (center). Below the copper there are inserts for three TLDs in each region, including the 0 mm region (right). Film is inserted above the TLDs, with a shim in between to prevent scatter. 58

Figure 3-8 (Left) The measured film distribution for one of the half-value layer (HVL) experiments, with labels for the copper thickness above each region. (Right) Measured film doses (normalized to 1) and best-fit exponential curves for the HVL phantom irradiated with 300 kV x-rays, 225 kV x-rays with an aluminum filter, and 225 kV x-rays with a copper filter. A simple exponential relationship cannot accurately model the attenuation of polyenergetic beams, which is most evident for the 225 kV beam with aluminum filtration. 59

Figure 3-9 3D printed monkey phantom parts. The bone segments were printed out of Ceramic Resin (left) and soft tissue out of Flexible Resin (center). Inserts in the phantom abdomen and chest were designed for TLD dosimetry (right). 62

Figure 3-10 CT images for the real monkey (left) and phantom (right) in the pelvis (upper) and spine (lower). The center slit in the phantom pelvis was designed for film insertion. Measured HU values for ROIs in the soft tissue and bone (shown in green) are given on the right. (HU: Hounsfield Units) 63

Figure 3-11 (Left) Calculated dose for the phantom test plan, with a prescription dose of 8 Gy to a 10 mm target in the phantom chest delivered in one full arc. Real tissue, lung, and bone material properties were used for dose calculation. (Right) Measured dose from film inserted into the midsagittal slit in the phantom chest, at the same plane as the calculated dose shown in the center. 63

Figure 4-1 (Upper) Calculated concave dose distribution (with colorbar units in Gy) in the mouse brain delivered with a hypothetical MLC (A) and the SOC (B). Simultaneous integrated boost SOC plan (C) with a 125% dose boost to the overlapping target region. (Lower) Dose volume histogram comparisons for plans in (A-C). The SOC plans show a more homogeneous dose with less high dose spillage using the same number of segments. 79

Figure 4-2 Dose volume histograms (left) and dose wash (right) for the mouse phantom whole liver irradiation plan, optimized with RAO. In both images, the liver (target) is shown in teal, body in yellow, and kidneys in red. 80

Figure 4-3 (Left) Target image for the Audrey Hepburn plan, with 4 dose levels of 0, 2, 4, and 6 Gy. (Right) Optimized dose distribution from RAO with 1 mm beamlet and minimum aperture size. The optimized plan used 551 apertures with an average size of 2.4 mm. 81

Figure 4-4 Measured output factors (average and standard deviation shown for 4 measurements) for the SmART system, calculated as a fraction of the full 26 mm SOC field 82

Figure 4-5 The 2.5 mm field off-axis dose film map (left), mean dose measurement map (center), and final interpolated off-axis factor map (right). 83

Figure 4-6 Measured percent depth dose curves for different field sizes on the SmART (solid lines) and for the energy spectra optimized to match each measured curve (dashed lines). 84

Figure 4-7 (Upper) Difference from the recalculated (field size-specific) dose for each optimization spectrum. (Lower) Dose optimized with the 1 mm field calculation spectrum (left), difference between the optimized dose and the recalculated dose, with

a mean of 1.2% and maximum of 11.0% of the maximum plan dose (middle), difference between the optimized dose and the dose after reoptimization of the aperture weightings, with a mean of 1.2% and a maximum of 7.3% of the maximum plan dose (right). All dose distributions are shown at the target depth of 2 mm. (D_{opt}: original optimized dose; D_{recalc}: optimized dose recalculated based on aperture size; D_{reopt}: dose after reoptimization of aperture weightings) 87

Figure 5-1 Leaf designs for the SOC, with dimensions shown in millimeters. Upper and lower leaf sets feature different radii of curvature and different geometry for the outer stabilizing tongues (along the top/bottom for upper/lower leaves, respectively). Each tongue and groove pair also has a mirroring pair with the tab on the opposite end..... 95

Figure 5-2 CAD model of the SOC. (A) Leaves connected to motor shafts with 3D printed rods and pins. (B) Stepper motor pair screwed into housing. (C) Outer leaf tongues slide along rails in housing. Shown in each corner of the SOC field are tungsten inserts for shielding the corners of the larger 4 x 4 cm primary collimator field. (D) All four orthogonal leaf banks. (E) Covers slide into the housing over each motor bank. (F) Main housing top attached, with mount for square primary collimator. (G) Complete SOC system with adapter to the primary 4x4 cm square SmART collimator. The collimator slides tightly into the adapter with a screw clamp for added support. The C-shaped attachment around the adapter guides the motor cables to the main socket on the back of the SOC. 96

Figure 5-3 The SOC mounted onto the gantry of the SmART system via the primary 4 cm fixed collimator..... 97

Figure 5-4 Machining of the prototype tungsten alloy leaves for the SOC. 97

Figure 5-5 3D printed SOC housing: main SOC leaf housing (upper left); outer leaf tongues slide along housing rails (upper middle); leaves attached to motors with 3D printed rods and pins (upper right); housing with all 8 SOC leaves (lower left); housing top with opening for 4 x 4 cm primary collimator and cable guide attachment (lower middle); housing for Arduino board and motor driver boards (lower right). 98

Figure 5-6 Graphic user interface for SOC control, with an aperture sequence loaded from a JavaScript Object Notation (JSON) file. Apertures can be edited and saved using the Sequence Item Editor shown. Leaves can also be controlled by dragging the gray "leaves" on the left. The "Calibrate Leaflet Positions" feature can also be used to set a new leaf "zero" position. 100

Figure 5-7. SOC installed on SmART system, attached to the 4 x 4 square primary collimator. 101

Figure 5-8 SOC leaf position calibration procedure using the fluoroscopy mode of the SmART system calibration software. (Upper) SOC axes are determined from the inner leaf edges.

(Lower) open leaf positions are set to the desired distance from each axis and the new calibration is saved with the SOC GUI.....102

Figure 5-9 (Left) Mouse phantom modeled from mouse CT data and 3D printed with a flexible, tissue-equivalent material and a mid-coronal split for film measurement. Phantom is shown on the previously mentioned rotating couch mount. (Right) 3D printed block phantom for axial dose measurements. 105

Figure 5-10 (Left) The measured offsets between the SOC field center and treatment isocenter at each projection angle in the x (blue) and y (red) directions are shown with solid lines. The difference between the offsets with the SOC (mounted on the primary collimator) and the primary collimator alone (S40) are shown with dotted lines. (Right) Spoke shot pattern from 1 mm slit SOC fields delivered at 8 equally spaced angles, measured perpendicular to the rotational axis and shown with a 2 Gy minimum dose cutoff.....108

Figure 5-11 Abutting field film patterns for the upper (left) and lower (center) leaves, normalized to the average field dose. (Right) One of the alignment verification grid patterns delivered with the SOC, normalized to the maximum dose.....109

Figure 5-12 (Left) Calculated dose distribution of the C-shaped target plan perpendicular to the gantry rotation axis. (Center) Measured film dose distribution from the center of the solid water phantom for the C target plan delivered with the SOC. Both plans are shown with the same color scale, in units of Gy. (Right) A comparison of the calculated (yellow) and measured (blue) 50% isodose lines, with overlapping regions shown in red.....113

Figure 5-13 (A) Mid-coronal view of the calculated dose for the mouse phantom whole liver plan (units of Gy). (B) The 5 optimal coplanar beam angles selected with the 4π algorithm. (C) Measured film dose from the mouse phantom, treated with the whole liver plan, at the plane shown in (A) (units of Gy). (D) A comparison of the calculated (yellow) and measured (blue) 60% isodose lines, with overlapping regions shown in red. Target structure was rotated to account for slight phantom misalignment, which also resulted in the truncated lower left portion of the target. 114

Figure 5-14 (Left) Calculated Audrey test plan with 4 dose levels and an average aperture size of 2.35 mm. (Right) Measured dose distribution of the Audrey plan delivered with the SOC. Both plans are shown with the same color scale, in units of Gy.....115

LIST OF EQUATIONS

Equation 2-1 13

Equation 2-2 14

Equation 2-3 15

Equation 2-4 30

Equation 2-5 31

Equation 4-1 70

ACKNOWLEDGEMENTS

I would first like to express my deepest thanks to my advisor, Dr. Ke Sheng, for all his guidance over the last five years. I am so grateful to have had such a supportive and understanding mentor. His knowledge, curiosity, and passion for medical physics has inspired and motivated me throughout my graduate career.

I am also sincerely grateful to the rest of my dissertation committee, Dr. Dan Ruan, Dr. Kei Iwamoto, and Dr. Erik Tryggestad. Their fresh perspectives and insightful feedback have been extremely valuable to this work.

I would also like to thank Dr. Michael McNitt-Gray and Reth Im for everything they do for the Physics and Biology in Medicine program. I cannot imagine a graduate program that cares more about the success and overall well-being of its students.

I could not have done this without the help and friendship of my labmates, Victoria, Dan, Angelia, Daniel, Ryan, Wenbo, Elizabeth, Qihui, and Daili. I cannot wait to see the great things that they all will accomplish. I was lucky to be part of a lab with so much opportunity for collaboration and growth.

I am eternally grateful to my parents for their constant support in everything I do. All of my accomplishments have been possible because of them and the opportunities they have provided for me. A big thanks to my brothers as well for cheering me on but always keeping me humble. Finally, I want to thank Kris for believing in me far more than I believe in myself. His love and encouragement got me through the final stretch.

VITA

EDUCATION

M.S.	University of California, Los Angeles, Biomedical Physics	2017
B.S.	University of California, Los Angeles, Bioengineering	2012

AWARDS

Moses A. Greenfield Award	2018
Norm Baily Award (AAPM Southern California Chapter)	2018

PEER-REVIEWED PUBLICATIONS

1. **K. Woods**, D. Nguyen, R. Neph, D. Ruan, D. O'Connor, K. Sheng. "A Sparse Orthogonal Collimator for Small Animal Intensity Modulated Radiation Therapy, Part I: Planning System Development and Commissioning," *In submission.*
2. **K. Woods**, R. Neph, D. Nguyen, K. Sheng. "A Sparse Orthogonal Collimator for Small Animal Intensity Modulated Radiation Therapy, Part II: Hardware Development and Commissioning," *In submission.*
3. V.L. Murzin, **K. Woods**, V. Moiseenko, R. Karunamuni, K. Tringale, T. Seibert, M. Connor, D. Simpson, K. Sheng, J. Hattangadi-Gluth, **"**4π plan optimization for cortical-sparing brain radiotherapy," *Radiotherapy and Oncology*, 127(1): 128-135 (2018).
4. **K. Woods**, P. Lee, T. Kaprealian, I. Yang, K. Sheng, "Cochlea-sparing acoustic neuroma treatment with 4π radiation therapy," *Advances in Radiation Oncology*, 3(2): 100-107 (2018).
5. V. Yu, A. Landers, **K. Woods**, D. Nguyen, M. Cao, R.K. Chin, D. Du, K. Sheng, T.B. Kaprealian, "A prospective 4π radiotherapy clinical study in recurrent high grade glioma patients," *Int J Radiat Oncol Biol Phys*, 101: 144-151 (2018).
6. A. Tran, **K. Woods**, D. Nguyen, V. Yu, T. Niu, M. Cao, P. Lee, K. Sheng, "Predicting liver SBRT eligibility and plan quality for VMAT and 4π plans," *Radiation Oncology*, 12(1): 70 (2017).
7. A. Tran, J. Zhang**, K. Woods**, V. Yu, D. Nguyen, G. Gustafson, L. Rosen, K. Sheng, "Treatment planning comparison of IMPT, VMAT and 4π radiotherapy for prostate cases," *Radiation Oncology*, 12(1): 10 (2017).
8. D. Nguyen, D. Ruan, D. O'Connor, **K. Woods**, D. Low, S. Boucher, K. Sheng, "A novel software and conceptual design of the hardware platform for intensity modulated radiation therapy," *Medical Physics*, 43(2): 917-929 (2016).

9. **K. Woods**, D. Nguyen, A. Tran, V. Yu, M. Cao, T. Niu, P. Lee, K. Sheng, "Viability of noncoplanar VMAT for liver SBRT compared with coplanar VMAT and beam orientation optimized 4π IMRT," *Advances in Radiation Oncology*, 1(1): 67-75 (2016).
10. P. Dong, V. Yu, D. Nguyen, J. Demarco, **K. Woods**, S. Boucher, D. Low, K. Sheng, "Feasibility of using intermediate x-ray energies for highly conformal extracranial radiotherapy," *Medical Physics*, 41(4): 041709 (2014).

SELECTED CONFERENCE PRESENTATIONS

1. **K. Woods**, D. Nguyen, R. Neph, D. O'Connor, S. Boucher, K. Sheng (2018, July/October). "Sparse Orthogonal Collimator with Rectangular Aperture Optimization for Small Animal IMRT," AAPM Annual Meeting, Nashville, TN, and ASTRO Annual Meeting, San Antonio, TX.
2. **K. Woods** (2018, July). "Shaping Pre-Clinical Radiotherapy Research," MedPhys Slam National Competition – AAPM Annual Meeting, Nashville, TN.
3. **K. Woods**, D. Nguyen, D. Ruan, D. O'Connor, K. Sheng (2017, July). "Double-Focused Sparse Orthogonal Collimator Design for Small Animal X-Ray Irradiators," AAPM Annual Meeting, Denver, CO.
4. **K. Woods**, M. Harrison, S. Boucher, J. McNevin, S. Kutsaev, L. Faillace, K. Sheng (2016, August). "Novel Hardware and Software Platform for Intermediate Energy 4π Radiotherapy," AAPM Annual Meeting, Washington, D.C.
5. **K. Woods**, R. Karunamuni, A. Tran, V. Yu, D. Nguyen, J. Hattangadi-Gluth, K. Sheng (2016, August). "Dosimetric Comparison of 4π and Clinical IMRT for Cortex-Sparing High-Grade Glioma Treatment Plans," AAPM Annual Meeting, Washington, D.C. ***Best in Physics (Therapy)***
6. **K. Woods**, D. Nguyen, A. Tran, V. Yu, M. Cao, K. Sheng (2015, July). "Comparison of Coplanar VMAT, Non-Coplanar VMAT, and 4π Treatment Plans," AAPM Annual Meeting, Anaheim, CA.
7. **K. Woods**, S. Boucher, B.M. Hegelich, V. Bashkirov, R. Schulte (2013, October). "Diagnostic Proton Computed Tomography Using Laser-Driven Ion Acceleration," North American Particle Accelerator Conference, Pasadena, CA.

INVITED TALKS

A Double-Focused Sparse Orthogonal Collimator for Small Animal IMRT Using Rectangular Aperture Optimization. AAPM-SCC Norm Baily Award Meeting 1st place prize, May 2018.

1 INTRODUCTION

According to the International Agency for Research on Cancer (IARC), over 18 million new cancer cases were diagnosed worldwide in 2018[1]. Of these cancer patients, it is estimated that over 50% can benefit from some form of radiotherapy[2]. With almost 10 million cancer deaths worldwide in 2018[1], there is clearly a need for improved radiotherapy techniques to increase overall survival rates. However, the number of cancer survivors treated with radiation is increasing steadily and is projected to reach over 4 million in the United States alone by 2030[3], making the mitigation of long-term side effects of radiotherapy equally as important.

Technological advancements in radiation oncology have greatly improved the precision and conformity of radiotherapy techniques. Much of this is due to advancements in imaging, with new diagnostic imaging techniques enabling better tumor delineation and image-guidance allowing for smaller treatment margins and lower normal tissue toxicity[4]. Recent advances in magnetic-resonance (MR) guided radiotherapy offer significant improvements in soft tissue visualization, further expanding the realm of treatment

possibilities[5,6]. With this technology it is feasible to deliver highly conformal, potentially escalated doses and to implement more novel techniques such as adaptive therapy, advanced motion management, and spatial or temporal dose modulation. However, although we may have the technical capabilities, there are currently several factors limiting the full exploitation of innovative techniques necessary for achieving significant improvements in patient outcomes.

1.1 4π Radiotherapy

One such limitation is the manual selection of largely coplanar beam angles used in clinical treatment planning. Although the use of noncoplanar beams has been shown to increase dose conformity and improve organ-at-risk (OAR) sparing[7], the manual selection of highly noncoplanar angles is tedious and unintuitive. This is further complicated by the increased risk of collision between couch and gantry. The 4π radiotherapy framework was developed to address this problem, enabling the automated selection of highly noncoplanar beam angles that can be delivered on a conventional C-arm linear accelerator[8]. 4π radiotherapy has demonstrated significant potential for increased dose conformity and normal tissue sparing in the treatment of tumors in the liver[8], lung[9], head-and-neck[10], prostate[11,12], brain[13], and spine[14] when compared to conventional intensity modulated radiation therapy (IMRT) with manually selected beams or volumetric modulated arc therapy (VMAT). An individualized collision prediction model has also been developed to enable fully automated noncoplanar plan delivery[15].

1.2 Preclinical Radiotherapy

Another limitation to the use of these novel treatment techniques is a lack of understanding of the underlying biological mechanisms. Much of this advancement has been driven by physics and engineering developments, and preclinical validation is needed to determine which strategies will actually improve patient outcomes. Small animal models are the most practical and widely used preclinical research tool, and can help us gain a better understanding of cancer cell growth and radiation response[16,17]. These research findings, however, often cannot be replicated in human clinical trials due in large part to the discrepancy in irradiation techniques[18-21].

Although the incorporation of image-guidance technology into small animal radiotherapy has greatly increased preclinical research potential, these systems are still not able to deliver IMRT, the clinical gold standard. IMRT requires inverse fluence map optimization and dose modulating hardware, both of which must be adapted for the small animal scale. The dynamic multileaf collimator (MLC) is used for dose modulation in clinical treatment, but due to its complexity previous attempts to miniaturize this device for the small animal scale have been relatively unsuccessful, as well as several other attempted dose modulation strategies[22-25]. We have developed a simpler device, the sparse orthogonal collimator (SOC), better suited for small animal radiotherapy. Using a corresponding treatment planning system based on rectangular aperture optimization (RAO), we can create high quality small animal IMRT plans for delivery with the SOC.

1.3 Overview

Preliminary studies will first be presented on the validation of 4π radiotherapy for specific treatment sites and the development of tools and techniques for dosimetric evaluation in preclinical radiotherapy research. Development and commissioning of the SOC treatment planning and delivery systems are then detailed.

Chapter 2 describes three planning studies in which the feasibility and advantages of 4π radiotherapy are evaluated for different applications. First, a version of the paper "Viability of noncoplanar VMAT for liver SBRT compared with coplanar VMAT and beam orientation optimized 4π IMRT" published in *Advances in Radiation Oncology*[26] is presented. This study evaluates the plan quality, particularly dose conformity and normal liver sparing, for liver SBRT plans using standard coplanar VMAT, noncoplanar VMAT, and 4π plans with 20 optimized noncoplanar static beams. Next, a version of the paper "Cochlea-sparing acoustic neuroma treatment with 4π radiotherapy", also published in *Advances in Radiation Oncology*[27], is presented. In this study, 4π radiotherapy is evaluated for its potential to spare dose to the cochlea in acoustic neuroma treatment and potentially reduce the risk of subsequent hearing loss. The third study is part of the paper "4π plan optimization for cortical-sparing brain radiotherapy" published in *Radiotherapy and Oncology*[28]. This work was performed in collaboration with researchers at the University of California San Diego, and investigates the ability of 4π radiotherapy to reduce the dose to the cortex in brain radiotherapy, consequently reducing the risk of cognitive decline post-treatment.

In Chapter 3, two projects related to preclinical radiotherapy dosimetry are presented. In the first, two types of mouse phantoms were developed for the evaluation and

standardization of the dosimetric accuracy of small animal irradiation techniques. These phantoms were sent to institutions across the country for irradiation, and the resulting dosimetry was analyzed using thermoluminescent dosimeters (TLDs), optically stimulated luminescent dosimeters (OSLDs), and radiochromic film dosimetry. Next, an anatomically accurate monkey phantom was developed for preclinical dosimetry. A flexible, straightforward phantom fabrication process was established using 3D printing methods with materials closely mimicking the radiological properties of tissue, lung, and bone.

Chapter 4 describes the development and commissioning of the SOC treatment planning system. The RAO algorithm is presented, with several planning experiments demonstrating its ability to create highly concave, complex dose distributions deliverable with the SOC. Beam commissioning data acquired on the X-RAD SmART Small Animal Image-Guided Radiotherapy system at UCLA is presented, including output and off-axis factors, percent depth dose data, and field flatness. The incorporation of this data into the treatment system is described, as well as the implementation of post-optimization dose recalculation and aperture weighting reoptimization. This is a version of the paper "A Sparse Orthogonal Collimator for Small Animal Intensity Modulated Radiation Therapy, Part I: Planning System Development and Commissioning", currently in submission[29].

In Chapter 5, the complete design and fabrication process of the SOC hardware is detailed. SOC commissioning data is presented, including measurements of mechanical alignment, leaf transmission, penumbra, and leaf positioning accuracy and repeatability. The measured dose distributions from the plans described in Chapter 4 are presented, and the agreement between the measured and intended doses is evaluated. This is a version of the

paper “A Sparse Orthogonal Collimator for Small Animal Intensity Modulated Radiation Therapy, Part II: Hardware Development and Commissioning”, also currently in submission[30].

2 4π RADIOTHERAPY

2.1 Viability of Noncoplanar VMAT for Liver SBRT Compared with Coplanar VMAT and Beam Orientation Optimized 4π IMRT[26]

2.1.1 Introduction

Liver cancer is responsible for over 600,000 deaths each year, according to the American Cancer Society, making it a leading cause of cancer deaths worldwide. Although surgical resection is considered the primary treatment option for hepatocellular carcinoma and oligometastases, 80 to 90% of patients present with unresectable tumors[31], which are treated with modalities including radiation therapy. Conventionally fractionated radiotherapy has proven ineffective to achieve local control[32]. Stereotactic body radiation therapy (SBRT), with the delivery of fewer high-dose fractions, is a more effective treatment for patients with eligible conditions[33], which typically include inoperable liver tumors under the size of 6 cm and certain liver function criteria[34]. The success of SBRT is largely owed to the higher biological effective doses (BED) and normal tissue sparing afforded by improved dose conformity from recent advances in radiation physics[31,35,36].

Volumetric modulated arc therapy (VMAT) is a practical and effective delivery technique for liver SBRT, and has demonstrated normal tissue sparing and dose conformity superior to coplanar intensity modulated radiation therapy (IMRT)[37]. Although the incorporation of noncoplanar beams has improved normal tissue sparing in liver IMRT

studies[7,37,38], typical clinical VMAT liver plans are still coplanar, consisting of a pair of (clockwise and counterclockwise) arcs using collimators with 90˚ rotational offset. To gain dose conformity and liver sparing, manually selected noncoplanar VMAT has been clinically used but its benefit has not been quantified. Meanwhile, methods for the automatic selection of noncoplanar IMRT beams and optimized fluence maps have been developed for treatment sites including liver SBRT. Two separate groups have shown that by optimizing noncoplanar beam orientation selection, superior dosimetry to coplanar VMAT can be attained[7,39]. In this study, we refer to the beam orientation optimized noncoplanar IMRT plans as "4π static" because of the maximum of 4π steradian angles that can be used for noncoplanar beam orientation optimization. The useable angles are typically smaller than 4π due to collision concerns and couch pedestal occlusion[40]. Since the delivery efficiency of noncoplanar IMRT plans is considered lower than that of VMAT without the use of automation, a function unavailable to most clinics, one important question is whether manually selected noncoplanar VMAT, which is the only clinically available method to incorporate these arcs, can offer dosimetry superior to coplanar VMAT while maintaining the advantage of clinical availability and efficiency. The purpose of this study is therefore to quantify and compare the dosimetry of these planning methods for liver SBRT.

2.1.2 Methods

2.1.2.1 Coplanar VMAT Plans

Under institutional review board approval, treatment plans including CT, dose, and contours were obtained for 20 liver SBRT patients (Table 2-1). These patients were treated with VMAT plans (RapidArc, Eclipse Treatment Planning System Version 10, Varian),

typically consisting of two full coplanar arcs (cVMAT) with 90° collimator angle offset. The few original plans that included one partial noncoplanar arc were re-optimized in Eclipse with two full coplanar arcs to set a uniform baseline.

Table 2-1 Patient Data

	Diagnosis	Prescription Dose (Gy)	Fractions	PTV Volume (cm^3)	Normal Liver Volume (cm^3)	Liver Volume (cm^3)
1	Metastatic esophageal cancer	60	5	53.3	1491.0	1544.5
2	Metastatic squamous cell carcinoma	60	5	64.9	2169.9	2234.7
3	Metastatic adenocarcinoma of the lung	60	5	46.7	1194.2	1239.0
4	Metastatic colorectal cancer	60	5	35.6	1168.6	1187.5
5	Metastatic colon cancer	60	5	59.2	1404.7	1454.3
6	Metastatic colorectal cancer	50	5	123.0	1324.1	1447.1
7	Metastatic uterus carcinosarcoma	50	5	35.1	1768.8	1803.8
8	Metastatic transitional cell from the kidney	60	5	30.2	1241.2	1270.1
9	Metastatic colon cancer	50	5	179.0	1752.7	1909.4
10	Hepatocellular carcinoma	36	3	54.4	1133.4	1187.9
11	Metastatic colon cancer	60	5	88.4	1302.7	1391.1
12	Metastatic prostate adenocarcinoma	60	5	10.5	1442.7	1453.3
13	Metastatic cholangiocarcinoma	40	5	48.8	1837.0	1837.0
14	Metastatic high-grade cholangiocarcinoma	48	3	19.4	1027.0	1047.8

15	Cholangiocarcinoma	40	5	88.7	1787.0	1852.0
16	Cholangiocarcinoma	40	5	67.0	2517.6	2577.3
17	Cholangiocarcinoma	40	5	141.8	1809.6	1926.6
18	Metastatic primitive germ cell tumor	30	5	192.9	3342.8	3346.1
19	Metastatic gall bladder small-cell carcinoma	60	5	109.4	1533.5	1616.2
20	Metastatic bile duct adenocarcinoma	50	5	57.3	1107.8	1148.6

2.1.2.2 Noncoplanar VMAT Plans

These clinical plans were re-planned in Eclipse with 3 to 4 manually selected partial noncoplanar arcs (nVMAT), as shown in Figure 2-1 (middle), with collimator angle offsets between 45° and 135°. The average total arc length for the 20 nVMAT plans was 553°. These arcs were empirically chosen to maximize noncoplanar angles while avoiding collision. Each plan typically consisted of one arc with a 0° couch rotation, two arcs with an average couch rotation of ±21° (-40° to +35° range), and for a few patients with tumors located near the mid-sagittal plane, one arc with a nearly perpendicular couch kick (86° on average). The optimization objectives were set up to minimize dose to liver, kidneys, spinal cord, and stomach, with the highest priority placed on the normal liver dose. All plans were normalized to deliver 100% of the prescribed dose to 95% of the planning target volume (PTV), and PTV hot spots were limited to those of the respective coplanar plans. A source-to-axis distance (SAD) of 100 cm was maintained for all plans.

2.1.2.3 4π Static Plans

The first step in the 4π static optimization process, the details of which have been previously reported[39], is to eliminate any beams out of the 1162 beam 4π static solid angle space that would cause collisions between the gantry and couch or patient. From the remaining beams, an integrated beam orientation and fluence map optimization is performed using a greedy column generation method[41]. Briefly, the remaining candidate beams were subdivided into 5 x 5 mm^2 beamlets and the dose distribution matrices of each beamlet were calculated using collapsed-cone convolution/superposition codes and 6 MV x-ray polyenergetic kernels with heterogeneity corrections. The dose calculation model was tuned to match 6 MV machine commissioning data. The dose calculation resolution was 2.5 x 2.5 x 2.5 mm^3. The first-order derivative of the quadratic cost function with each additional beam from the candidate pool was evaluated and the beam that contributed most was kept.

This process was iteratively performed until the desired number of beams was selected. Full fluence map optimization was performed after each beam selection. Although the cost function value did not converge, the dosimetric gains with more than 20 beams were modest. Considering a balance between plan deliverability and plan quality, in this study, 20 beams were selected with the 4π static algorithm for each patient, such as those in Figure 2-1 (right). The gantry and couch angles for each beam were imported into Eclipse to develop a clinically deliverable treatment plan using an identical dose calculation engine to the VMAT plans. The organ at risk (OAR) constraints, plan normalization, SAD, and PTV hotspots matched those described earlier for the nVMAT plans.

2.1.2.4 Additional notes on the optimization implementation

For each plan optimization, dose constraints were placed on the liver, kidney, spinal cord, and stomach. When necessary, additional optimization constraints were placed on other OARs such as the bowel or heart, depending on the location of the tumor. Although the constraints and penalties were initially the same for each, these parameters were adjusted throughout the optimization process in order to further reduce OAR doses for all techniques. Since plan optimization with Eclipse depends on both the sequence of the planning parameters used along with the process and the timing of when they are used, maintaining a single set of constraints and penalties generally would result in poorer plan quality. Instead, the objectives for each plan were pushed as hard as possible to reduce OAR doses, particularly to the normal liver, while maintaining acceptable PTV doses. The normal tissue objective was also used, with a 0.1 cm distance from target border, 99% start dose, 50% end dose, and 0.2 fall-off. Each plan was re-optimized until no further OAR dose reduction could be achieved without compromising PTV coverage (typically between two and four runs).

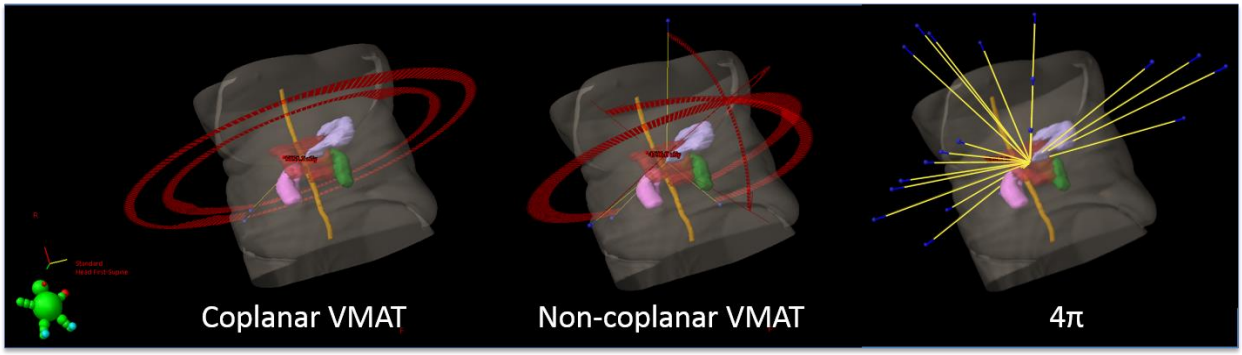

Figure 2-1 Beam geometry comparison for a typical liver SBRT case. Beam orientation is shown for the coplanar VMAT plan (left), 3 to 4 noncoplanar partial arcs (center) and 20 noncoplanar, optimized beams (right).

2.1.2.5 Plan Comparison

The cVMAT, nVMAT, and 4π static plans were evaluated by comparing various metrics of normal tissue sparing. The minimum dose to 98% of the PTV (D98%) was compared between the three plans to evaluate any under-dosage to the target. The conformity of each plan was evaluated by the conformation number (CN), defined by van't Riet et al as

$$CN = \frac{TV_{RI}}{TV} \times \frac{TV_{RI}}{V_{RI}},$$

Equation 2-1

where TV_{RI} is the target volume covered by the prescription isodose, TV is the target volume, and V_{RI} is the volume of the prescription isodose[42]. R_{50}, defined as the ratio of the 50% isodose volume to the PTV, was used to evaluate the dose gradient outside the PTV. The homogeneity index (HI) was also calculated as 1+(D2% - D98%)/(Prescription Dose). The normal liver volume receiving >15 Gy ($VL_{>15}$) was quantified to assess normal tissue dose, as were the mean and maximum doses to OARs.

A radiobiological modeling study was performed to compare the probabilities of tumor control, normal tissue complication, and patient survival. The tumor control probability (TCP) was first calculated for each plan. Because TCP calculation parameters vary widely between studies and for different tumor types[43,44], and because a variety of tumor origins were included in this study, high tumor radioresistance was assumed for the parameter selection ($\alpha = 0.2\ Gy^{-1}$, $\alpha/\beta = 10$ Gy) for a conservative TCP estimate. The Kutcher-Burman dose-volume histogram (DVH) reduction scheme[45] was used to calculate the normal liver effective volume (V_{eff}), the percentage of the normal liver volume that, if irradiated

uniformly to the prescription dose, would give the same normal tissue complication probability (NTCP) as the non-uniform dose distribution. The effective volume was then used to calculate the normal liver NTCP using the Lyman model[46]. The Lyman-Kutcher-Burman (LKB) NTCP model parameters from Dawson et al were used (TD_{50} = 45.8 Gy [metastases], TD_{50} = 39.8 Gy [primary tumors], n = 0.97, m = 0.12)[47]. Since these parameters were obtained from fractionated treatment plans, the SBRT plans in this study were normalized to 1.5 Gy per fraction using α/β = 2.5 Gy[48].

2.1.2.6 Dose Escalation

The prescription dose for each plan was escalated (or reduced) to the maximum tolerable dose (MTD) yielding a normal liver NTCP below the desired limit. The number of fractions for the clinical plans were maintained, with an escalated dose per fraction. In this study, MTDs for NTCP limits of 1%, 5%, and 10% were calculated. The biological effective dose (BED) for each MTD was determined by

$$BED = Nd + \frac{N}{\alpha/\beta}d^2 - \frac{ln2}{\alpha T_d}T\ ,$$

Equation 2-2

with number of fractions N, dose per fraction d, total treatment time T, α = 0.01, α/β = 15, and tumor doubling time T_d = 120 days from Tai et al[49]. The survival model developed by Tai et al was used to predict the survival rates (SR) for each plan based on the BED:

$$SR(D,d,\tau) = 1 - \frac{1}{\sqrt{2\pi}}\int_{-\infty}^{t} e^{-\frac{x^2}{2}}dx\,,$$

$$t = \frac{e^{-\left[\alpha\left(1+\frac{d}{\alpha/\beta}\right)D-\gamma T-\left(\gamma(\tau-T)\right)^{\delta}\right]} - K_{50}/K_0}{\sigma_k/K_0}$$

Equation 2-3

where D is the prescription dose, τ is the elapsed time since treatment, δ describes the tumor growth rate, K_0 is the initial number of tumor clonogens, K_{50} is the critical number of tumor clonogens corresponding to death in 50% of patients, σ_k is the Gaussian width for the critical clonogen number distribution, and $\gamma = \ln 2/T_d$. The fitting parameters from Tai et al are K_{50}/K_0 = 2.03, σ_k/K_0 = 0.65, and δ = 0.2[49]. Survival fractions at 1, 2, 3, and 4 years were calculated for each plan before and after dose escalation.

2.1.3 Results

2.1.3.1 Plan Comparison

The average dose statistics for each plan type, using paired, 2-tailed t-tests, are given in Table 2-2. On average, the nVMAT plans delivered higher kidney doses than the cVMAT plans and lower doses to the other OARs, but the only statistically significant difference was an increased V50%. However, there were large improvements with 4π static compared to both VMAT techniques. The mean dose to the normal liver was significantly lower with the 4π static plan, and the liver volume receiving >15 Gy was reduced from the cVMAT and nVMAT plans by 79.8 cm^3 and 74.8 cm^3, respectively (>32%). Although nVMAT enabled reductions in maximum stomach and spinal cord doses (compared to cVMAT) of approximately 2% and 14%, respectively, 4π static reduced these doses by 32% and 40%.

The HI and CN values were similar for all plans. The individual dosimetric parameter comparison is shown in Figure 2-2. Consistent reduction in the R_{50} from cVMAT to 4π static was observed for all patients and the reduction is correlated to that of liver V15 and mean liver dose. In comparison, R_{50} of nVMAT slightly increased from cVMAT, indicating no improvement in the dose compactness.

Table 2-2 Average dose statistics for coplanar VMAT, noncoplanar VMAT, and 4π plans for all 20 patients (HI: homogeneity index, CN: conformation number)

Plan Type	Organ-At-Risk Doses (Gy)					
	L Kidney Mean	**R Kidney Mean**	**Normal Liver Mean**	**Stomach Max**	**Cord Max**	**Body Mean**
cVMAT	1.42* (2.4)	2.04 (2.4)	7.07* (2.6)	11.15 (6.7)	6.69* (3.2)	1.51* (0.6)
nVMAT	1.46* (2.1)	2.09 (2.5)	6.97* (2.8)	10.95* (10.0)	5.74* (4.0)	1.51* (0.6)
4π	0.82 (1.2)	1.70 (1.4)	6.01 (2.3)	7.58 (6.3)	4.00 (3.7)	1.46 (0.6)
	PTV D98% (Gy)	**VL>15 (cm3)**	**V50% (cm3)**	**R50**	**HI**	**CN**
cVMAT	49.62* (9.6)	233.7* (120.8)	271.5** (185.6)	3.66* (0.4)	0.11 (0.03)	0.94 (0.03)
nVMAT	49.59 (9.7)	228.7* (122.3)	287.5** (213.4)	3.77* (0.5)	0.10 (0.02)	0.93 (0.04)
4π	49.42 (9.7)	153.9 (84.5)	210.8 (146.4)	2.82 (0.3)	0.11 (0.03)	0.93 (0.03)

*Significantly different from 4π with $p<0.05$ (paired, 2-tailed t-test).

**Significantly different from 4π and other VMAT plan type with $p<0.05$ (paired, 2-tailed t-test).

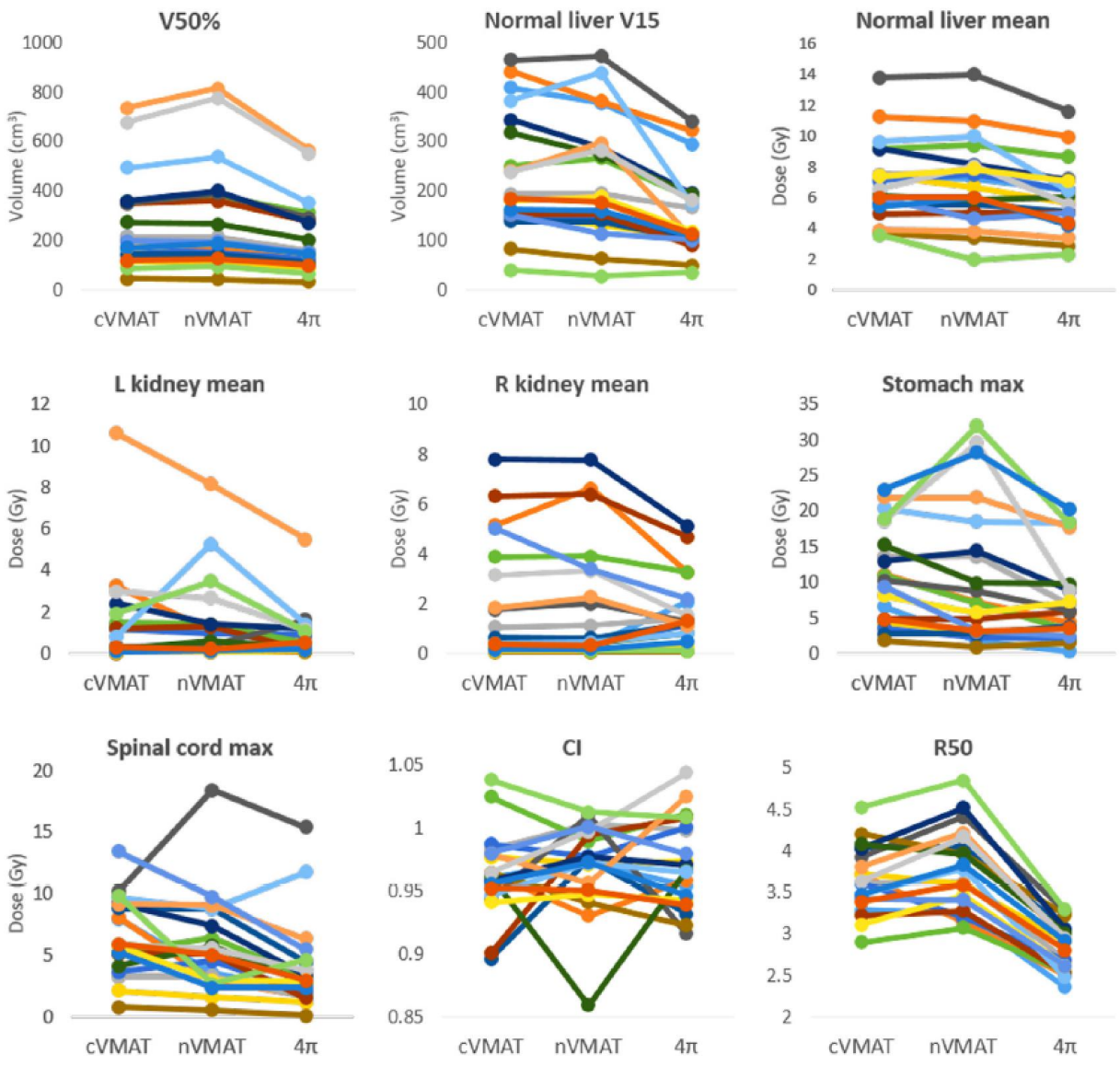

Figure 2-2 Individual patient dosimetric results comparison between cVMAT, nVMAT, and 4π static.

These reductions in OAR dose are evident in the DVHs in Figure 2-3 (top). Additionally, the 4π static technique reduced the 50% dose spillage volume by >22% compared to both VMAT plans. The major reduction in 50% isodose volume with the 4π static technique is evident in the dose washes in Figure 2-3 (bottom). Although the dose washes show less low dose spillage for the nVMAT plan than the cVMAT plan, the isodose

volume above 15 Gy is very similar. There was a statistically significant difference between the mean cVMAT and 4π static PTV D98% doses, but only by 0.2 Gy.

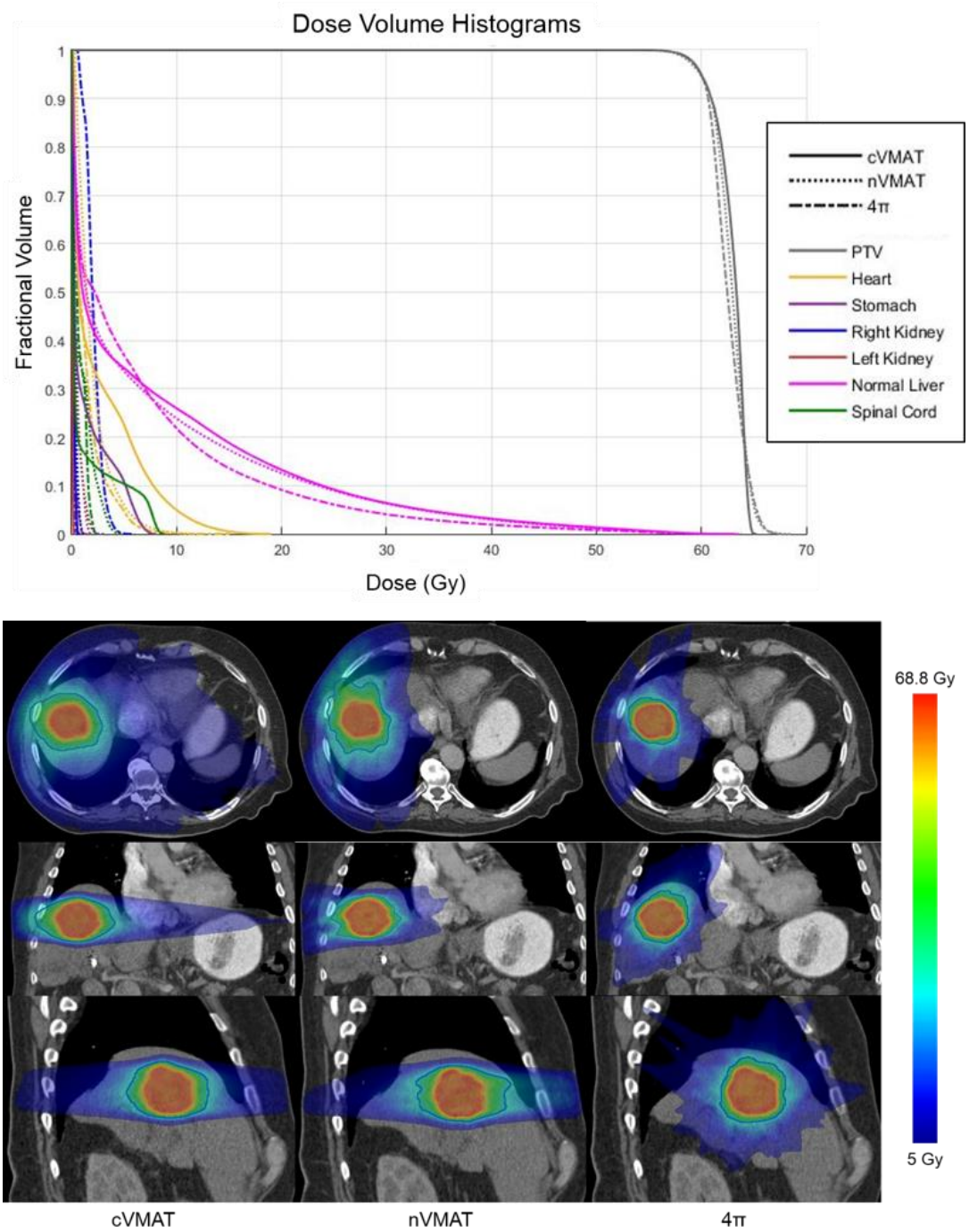

Figure 2-3 (Top) Dose-volume histograms for a typical liver SBRT case. (Bottom) Dose color washes for each plan type. The orange contours represent the PTV volume and the blue represent the 50% isodose lines.

The average TCP values (calculated with the LKB model), given in Table 2-3, were very similar for nVMAT and cVMAT plans and slightly (~1.1%) lower for 4π static. Although the optimization constraints on the maximum PTV dose were relaxed, 4π static plans still tend to result in more homogenous PTV doses, as seen in the DVH in Figure 2-2 (top), and slightly lower TCP.

Table 2-3 Biological modeling parameter results for cVMAT, nVMAT, and 4π plans for all 20 patients (standard deviation in parentheses)

	TCP (%)	**V_{eff} (%)**	**NTCP[a] (%)**
cVMAT	7.37 (11.5)	13.79* (5.2)	5.29 (18.8)
nVMAT	7.40* (11.1)	14.00* (5.9)	6.22 (22.2)
4π	6.25 (9.7)	11.63 (4.4)	1.65 (6.3)

[a]The mean NTCP is drastically increased by two outlying patients, without which the mean NTCP values are 0.06%, 0.53%, and 0.02% for cVMAT, nVMAT, and 4π, respectively.
*Significantly different from 4π plans with $p<0.05$ (paired, 2-tailed t-test).

The average normal liver effective volume was very similar for the VMAT plans, but was significantly reduced with 4π static by >15%. The resultant NTCP was therefore also much lower, with reductions of 69% from cVMAT and 73% from nVMAT.

2.1.3.2 Dose Escalation

The results of the dose escalation are given in Table 2-4. For every NTCP limit, 4π static enabled significantly higher average MTDs than both cVMAT and nVMAT. The escalated doses for 4π static were approximately 20% and 14% higher than those for cVMAT and nVMAT, respectively. The corresponding BEDs for 4π static were higher than cVMAT and nVMAT for every NTCP limit by about 39% and 19%, respectively, with a statistically significant difference between 4π static and cVMAT at the 5% level (paired, 2-tailed t-test).

The average MTD and BED for nVMAT were higher than cVMAT for every NTCP limit, but not statistically significant at the 5% level.

Table 2-4 Dose escalation based on the normal liver effective volume and desired normal liver LKB NTCP for all 20 patients (standard deviation in parentheses)

	1% NTCP		5% NTCP		10% NTCP	
	MTD (Gy)	**BED (Gy)**	**MTD (Gy)**	**BED (Gy)**	**MTD (Gy)**	**BED (Gy)**
cVMAT	76.80* (27.6)	170.40* (97.8)	85.51* (30.7)	202.70* (117.6)	90.14* (32.4)	220.94* (129.0)
nVMAT	80.63* (37.7)	198.32 (177.7)	89.76* (41.6)	236.78 (215.5)	94.65* (43.8)	258.67 (237.4)
4π	91.98 (36.2)	235.80 (164.8)	102.43 (40.3)	281.91 (199.8)	107.99 (42.5)	308.08 (219.8)

*Significantly different from 4π plans with $p<0.05$ (paired, 2-tailed t-test).

The average survival fractions at 1, 2, 3, and 4 years for each NTCP limit (1%, 5%, and 10%) showed a statistically significant increase for the 4π static plans compared to both VMAT plans, as shown in Figure 2-4. These improvements were most significant for the 4π static four year survival fraction, which was over 7% higher than both VMAT plans at the 10% and 5% NTCP limits and over 9% higher at the 1% NTCP limit. Even for conservative treatments allowing for only a 1% probability of liver complications, the 4π static technique enabled an average four year survival fraction of 86%. This increased to 93% when a 10% NTCP was tolerated.

2.1.3.3 Delivery Time

The delivery time for two arc cVMAT for SBRT treatment was estimated as five to seven minutes. The time increased by an additional one to three minutes for nVMAT, depending on whether remote couch rotation was used. Delivery of the 4π treatment with

20 beams can take 45 minutes with manual couch rotation and translation. However, a significant portion of this time is used by the therapist to enter and exit the shielded vault. Consequently, the time can be reduced to approximately 12 minutes with automated delivery[40], in line with the nVMAT delivery time.

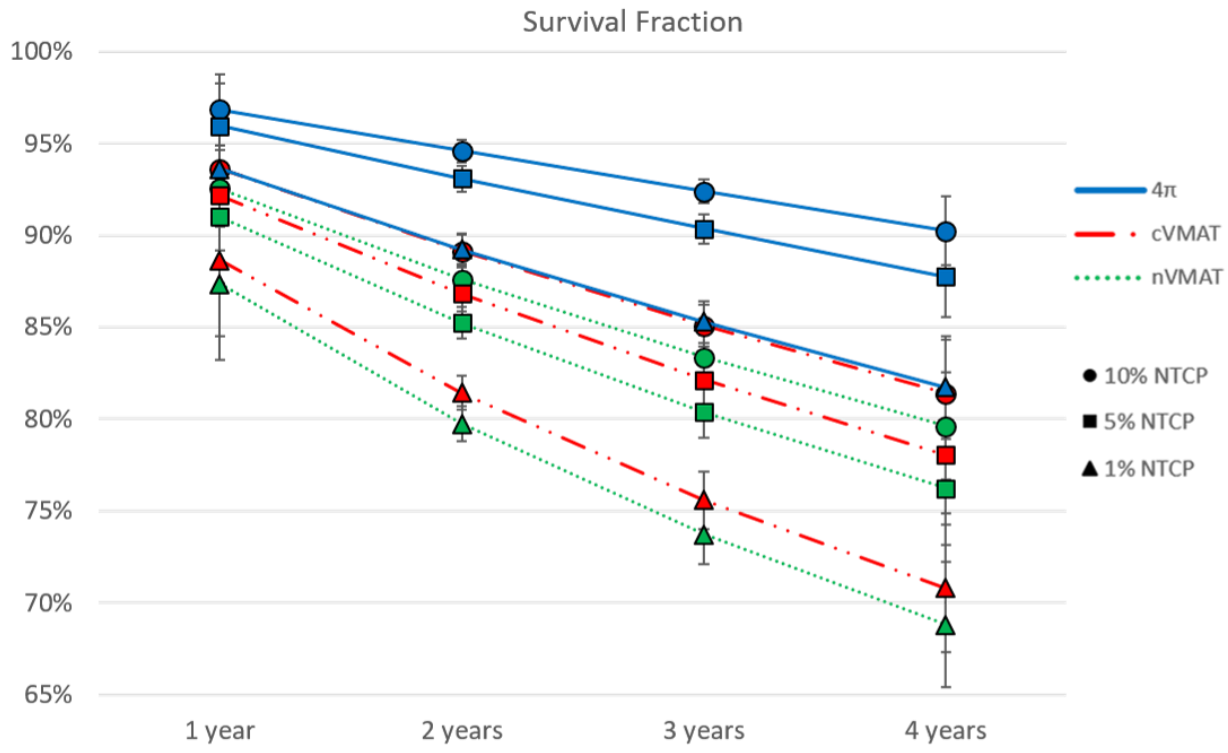

Figure 2-4 Average survival predicted with the model from Tai et al[49] for the maximum tolerable doses yielding 1%, 5%, and 10% normal liver NTCPs. All fractions for nVMAT and cVMAT were significantly different than 4π static at the 5% significance level (paired, 2-tailed t-test).

2.1.4 Discussion

The success of SBRT is largely attributed to the improved physical dose conformity enabled by recent advances in radiation therapy techniques, including intensity modulated radiation therapy, image-guided radiation therapy, and volumetric modulated arc therapy. A previous study showed that tumor local control can benefit from further dose escalation[35], but is limited by normal tissue toxicity.

Experience from intracranial radiosurgery suggests that an effective way to achieve a steeper dose gradient outside the tumor is by adding noncoplanar beams and arcs[50]. The usefulness of noncoplanar beams in SBRT has been far less clear. R_{50} has been commonly used to evaluate the dose compactness in SBRT treatment[51], the minimization of which leads to more effective SBRT[52]. Lung Radiation Therapy Oncology Group protocols[53] recommend using either noncoplanar static or coplanar arc beams to achieve the R_{50} dosimetric goal. Lim et al[54] showed that compared with coplanar plans, lower R_{50} could be achieved in 81% of patients when noncoplanar beam arrangement was employed. However, in a different lung study, no dosimetric improvements were found comparing coplanar and noncoplanar IMRT plans[55]. In the case of liver radiotherapy, it was found that the advantage of using noncoplanar beams can be matched by coplanar plans with a large number of beams[56]. Noncoplanar VMAT has been used on an ad hoc basis in liver SBRT[37] with the expectation that these arcs should improve normal organ sparing without quantification of the dosimetric improvement.

In this study, we compared three clinically deliverable planning methods for liver SBRT. Our study shows that the incorporation of this type of arrangement of noncoplanar VMAT arcs offered modest dosimetric gains over coplanar VMAT. However, by fully utilizing the freedom of the noncoplanar beam geometry solution space and automated beam orientation selection, the 4π static technique achieved major reductions in the dose to OARs, particularly the normal liver, stomach, and spinal cord, as well as a much more compact dose distribution.

There are several reasons for the minimal plan quality improvement from nVMAT over cVMAT. First, in practice, the number of VMAT arcs is limited. Due to the continuity of the arcs, large noncoplanar angles are prohibited to avoid collision. This is different from intracranial stereotactic radiation surgery, where a large noncoplanar beam solution space can be nearly uniformly sampled and included. It has been shown that the inclusion of small noncoplanar arc angles in a rotational IMRT system does not significantly improve the plan quality[57]. Second, selection of noncoplanar arcs is unintuitive to the planner. It is difficult, if not impossible, for a human operator to optimally select segments of noncoplanar arcs, considering the freedoms of arc lengths and locations. One way to overcome this limitation is by optimizing the noncoplanar arc selection. However, a method to globally search the noncoplanar arc trajectories, or "4π arc", is currently unavailable. Papp et al[58] reported a noncoplanar arc optimization method based on static beam orientation optimization and then using these beams to anchor noncoplanar segments. However this method does not promise that arcs between the anchoring beams are optimal. Furthermore, this method would result in arcs that require simultaneous couch and gantry rotation and are undeliverable in the clinical mode. Both limitations are effectively overcome using 4π static planning, where the collision-free beam geometry solution space is individually mapped and the beam orientations are optimized. Therefore, even though nVMAT is currently available and more efficient to deliver, it is not a reasonable substitution for 4π static.

A major difference between the current study and the previously published report of using 4π static for liver SBRT[39] is that the liver SBRT plans are generated in Eclipse using identical dose calculation engine to ensure an unbiased comparison. Compared to the previous study, the liver $VL_{>15}$ was further reduced by an additional ~30 cm^3 to 80 cm^3. This

increased normal tissue sparing is crucial for liver SBRT because it enables escalation of the prescription dose to the PTV without further complications from high doses to normal tissue. Our dose escalation study showed that for the same normal liver complication probability, prescription doses delivered with the 4π static technique could be escalated 20% higher than cVMAT plans and 14% higher than nVMAT plans, leading to significant increases in predicted survival fractions.

Improved liver tumor motion management can be combined with 4π static radiotherapy for additional dosimetric gains, but the gains may be less significant. For example, Velec et al[59] showed that by reducing the PTV volume using the mean respiratory position, the isotoxicity PTV dose can be escalated by 4 Gy, which is moderate compared to the dose escalation using 4π static.

2.1.5 Conclusions

4π static radiotherapy using optimized noncoplanar beams significantly reduces normal liver doses, enabling safe tumor dose escalation. Despite its clinical availability, VMAT using noncoplanar arcs is not a viable replacement for 4π static radiotherapy for compact dose liver SBRT.

2.2 Cochlea-Sparing Acoustic Neuroma Treatment with 4π Radiation Therapy[27]

2.2.1 Introduction

Acoustic neuroma, also known as vestibular schwannoma, is a benign brain tumor arising from the eighth cervical nerve. There are 2000 to 3000 new cases of benign acoustic neuroma in the United States each year, approximately 25% of which are treated with radiation therapy[60]. Due to its benign nature, the prognosis for acoustic neuroma patients is typically very good, and with proper surveillance and treatment, no decrease in lifespan is expected. Therefore, the long term post-treatment toxicity must be heavily weighted for these patients. Although the complication rates are much lower than with surgery[61-63], some patients do experience radiation-induced side effects following treatment. Up to 40% of patients may experience middle ear side effects such as otitis media during treatment[64], which can cause tinnitus, dizziness, and pain. Almost half of patients may also experience some degree of sensorineural hearing loss (SNHL), which continues to worsen for years after treatment[65-71].

There is evidence suggesting a correlation between the dose to the cochlea and the degree of hearing loss observed after radiation therapy for tumors in the head and neck region[72-76]. For acoustic neuroma patients treated with fractionated stereotactic radiotherapy, a study by Thomas et al showed that the minimum and maximum cochlear doses, as well as the percentage of the cochlea receiving 50%, 80%, and 90% of the prescription dose were all strongly predictive of subsequent hearing deterioration[77]. For stereotactic radiosurgery (SRS), significantly better hearing preservation was observed by

Kano et al when the dose to the central cochlea was kept below 4.2 Gy[78]. Timmer et al also demonstrated a correlation between the maximum cochlear dose and the extent of hearing loss in acoustic neuroma patients treated with Gamma Knife radiosurgery[79].

In addition to hearing loss, many acoustic neuroma patients experience cranial neuropathy following radiation therapy. In a study of 149 cases of acoustic neuroma radiosurgery, Foote et al found that the maximum dose to the brainstem was the most significant predictor of the incidence of facial, trigeminal, or any other type of neuropathy after treatment[80]. Therefore, the sparing of dose to the brainstem must also be a high priority for these patients.

However, adequate radiation doses must still be delivered in order to achieve long-term tumor control. A large Gamma Knife patient cohort established that a median single fractional dose of 13 Gy to the tumor margin (50% isodose) is necessary for local control[67]. This dose prescription typically results in maximum doses of 26 Gy for Gamma Knife plans, which may not always be safely deliverable[81], particularly for larger tumors. Although 12 to 13 Gy is also the standard prescription dose for linac-based single fraction acoustic neuroma treatment, these plans follow different prescription conventions (typically 100% of the prescription dose to 95-100% of the target volume) and result in more homogeneous dose distributions with lower maximum doses.

Therefore, to reduce the risk of hearing loss and other normal tissue complications following treatment while also delivering an adequate dose for maximal tumor control, highly conformal dose distributions are needed that can better spare the surrounding normal tissue. The dosimetry of Gamma Knife has been compared to conformal and dynamic

arcs using linacs for acoustic neuroma treatment[82]. Although the Gamma Knife dose was slightly more conformal (by 2%), the maximal dose was also much higher. This may help local control but can increase the risk of hearing loss and other neurological side effects since the intracanalicular component of the cochlear nerve, the cochlear ramus of the internal auditory artery, and the facial nerve all traverse the target volume[83]. Another advantage of linac-based treatment is that the treatment can be fractionated for larger tumors. A clinically relevant question is whether recent advances in treatment planning techniques can be used to further improve linac plans. 4π radiotherapy, with optimized noncoplanar beam orientations, has been shown to significantly reduce normal tissue doses in the liver, prostate, brain, lung, and head and neck[9,11,39,84]. The aim of this study was to determine whether 4π can also produce superior dosimetry for acoustic neuroma treatment, potentially providing better sparing of the cochleae and reducing the risk of radiation-induced complications such as hearing loss.

2.2.2 Methods

2.2.2.1 Clinical plans

Thirty patients previously treated with radiation therapy for benign acoustic neuroma were included in this study, and their computed tomography images, plan, dose, and contours were obtained (Table 2-5). Fourteen of these patients were treated with single-fraction SRS with prescription doses of 12 to 13 Gy. Six patients received stereotactic radiation therapy (SRT) with 5 fractions of 5 Gy each. Ten patients received intensity modulated radiation therapy (IMRT) with 28 to 30 fractions of 1.8 Gy each. Static IMRT beams (7-11 beams) were used for 13 patients (IMRT), dynamic conformal arcs (4-5 partial

noncoplanar arcs) were used for 11 patients (DCAT), and volumetric-modulated arcs (2 full coplanar arcs or 2-4 noncoplanar partial arcs) were used for 6 patients (VMAT).

Table 2-5 Patient data

	Rx dose (Gy)	Fractions	Plan type	PTV volume (cm^3)		Rx dose (Gy)	Fractions	Plan type	PTV volume (cm^3)
1	12	1	DCAT	0.5	**16**	25	5	IMRT	1.07
2	12	1	IMRT	5.48	**17**	25	5	IMRT	2.45
3	12	1	IMRT	2.7	**18**	25	5	VMAT	8.12
4	12	1	DCAT	1.66	**19**	25	5	IMRT	0.24
5	12	1	DCAT	3.33	**20**	25	5	IMRT	0.17
6	12	1	DCAT	2.75	**21**	50.4	28	VMAT	6.3
7	12	1	IMRT	0.74	**22**	50.4	28	VMAT	35.81
8	12	1	DCAT	2.79	**23**	50.4	28	IMRT	17.29
9	12	1	IMRT	2.54	**24**	50.4	28	DCAT	0.35
10	12	1	DCAT	2.24	**25**	50.4	28	DCAT	2.42
11	12	1	IMRT	3.1	**26**	50.4	28	DCAT	0.92
12	12	1	IMRT	5.23	**27**	50.4	28	VMAT	10.87
13	12	1	DCAT	2.65	**28**	50.4	28	IMRT	2.78
14	13	1	DCAT	1.31	**29**	50.4	28	VMAT	13.58
15	25	5	IMRT	2.54	**30**	54	30	VMAT	23.22

(DCAT: dynamical conformal arc therapy; IMRT: static intensity modulated radiation therapy; VMAT: volumetric-modulated arc therapy)

The plans were created using the machine parameter file for a Novalis Tx machine equipped with a 0.25 cm high-definition multileaf collimator. The dose calculation resolution was 2 mm using the Analytical Anisotropic Algorithm, Version 10.0.28. The treatment

regimen was determined on the basis of tumor size and achievable organ-at-risk (OAR) sparing. Examples of the beam orientations for these plans are shown in Figure 2-5. The brainstem, chiasm, cochlea (one or both, depending on the tumor location), eyes, lenses, and optical nerves were included as critical organs for all plans.

2.2.2.2 4π plans

4π plans were made for each patient using the optimization process previously published[39,41]. The optimization process started with a pool of 1162 candidate beams making up the 4π solid angle space, each with a separation of 6°. A computer-assisted design model of the Varian TrueBeam system, along with a 3-dimensional patient model, was used to detect any potential collisions between the gantry and the couch or patient.

After these beams were eliminated, the dose was calculated for 5 x 5 mm^2 beamlets using convolution/superposition with a 6 MV polyenergetic kernel. A greedy column generation method was then used to perform an integrated beam orientation and fluence map optimization[41]. The objective function includes manually-tuned parameters for the priority and weighting of each OAR, which were set to penalize dose to the cochlea and other critical organs while maintaining a homogeneous dose to the planning target volume (PTV). A final beam count of 20 was chosen to fully exploit the noncoplanar space while maintaining reasonable deliverability, as shown by a prospective patient study[85].

Next, using the optimized beams, fluence map optimization and dose calculation were performed again in Eclipse with parameters that were identical to those of the clinical plans for an unbiased comparison. The planning goal was to match the PTV coverage of the

clinical plans while reducing the dose to the cochleae and reducing or maintaining the doses to all other OARs.

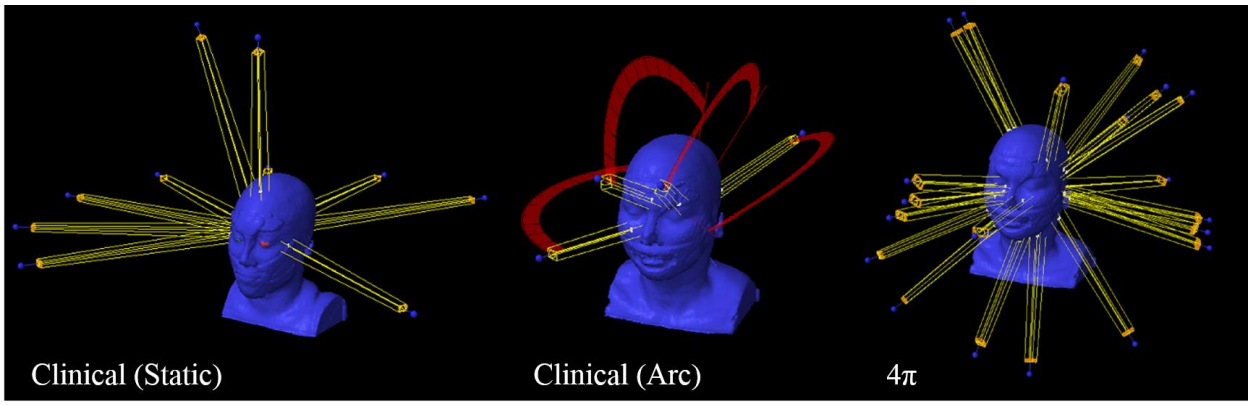

Figure 2-5 Examples of typical beam orientations for the clinical plans with 7 to 11 static beams (left), clinical plans with 2 to 5 arcs (middle), and 4π plans with 20 static beams (right). From Table 2-5, these are patients 16, 4, and 1, respectively.

2.2.2.3 Plan comparison

The 4π and clinical plans were compared on the basis of their PTV coverage and normal tissue sparing, specifically of the cochleae. The mean and maximum doses to the cochleae and all other OARs were compared for all plans. The volume receiving 50% of the prescription dose (V50%) was calculated to evaluate the dose spillage for each plan. To evaluate dose conformity, R_{100} (the ratio of the 100% isodose volume to the PTV) was compared, along with the van't Riet conformation number (CN)[42], defined as

$$CN = \frac{V_{T,Rx}}{V_T} \times \frac{V_{T,Rx}}{V_{Rx}},$$

Equation 2-4

where V_T is the target volume, $V_{T,Rx}$ is the volume of the target receiving a dose equal to or greater than the prescription dose, and V_{Rx} is the total volume receiving the prescription dose. The homogeneity index (HI) was also calculated as

$$HI = 1 + \frac{(D2\% - D98\%)}{D_{Rx}}$$

Equation 2-5

where D_{Rx} is the prescription dose and $D2\%$ and $D98\%$ are the minimum doses to 2% and 98% of the PTV volume.

Radiobiological modeling was also used to predict the tumor control probability (TCP) and the normal tissue complication probability (NTCP) for SNHL. The definition of SNHL differs between studies but is typically considered a loss of at least 10 to 20 dB in one or more frequencies. Because hearing function has been shown to continue deteriorating over long follow-up times[68], the SNHL NTCP at both 3 years and 5 years post-treatment was calculated for each plan.

The TCP was calculated using the Poisson-based model with the parameters shown in Table 2-6. The cochlea effective volume (V_{eff}) was calculated with the Kutcher-Burman dose volume histogram reduction scheme, which estimates the volume of the cochlea which, if homogenously irradiated to the prescription dose, would result in the same NTCP as the actual inhomogeneous dose distribution[86]. This effective volume was then used to predict the NTCP values for the cochlea with the Lyman model[46], using the parameters in Table 2-6.

Table 2-6 TCP and NTCP model parameters

Model Parameter[a]	TCP	SNHL NTCP (3 years)	SNHL NTCP (5 years)
α/β	2.4 Gy	2 Gy	2 Gy
TCD_{50}	27 Gy	-	-
TD_{50}	-	31.5 Gy	19.25 Gy
γ_{50}	1.5	0.71	0.46
n	-	0.83	0.83

[a]α/β: ratio of the linear and quadratic terms of the organ-specific dose response curve; TCD_{50}: tumor dose to achieve 50% TCP; TD50: whole organ dose resulting in 50% NTCP; γ50: slope of sigmoidal dose response curve at 50% TCP/NTCP; n: volume-effect parameter. (TCP: tumor control probability; SNHL: sensorineural hearing loss; NTCP: normal tissue complication probability)

All model parameters were selected on the basis of published clinical data on the relationship between treatment outcomes (tumor control and complication rates) and dose delivered to the tumor and cochleae[68-71]. Since the fractionation schemes varied widely among patients in this study, all plan doses were normalized to a reference dose of 2 Gy per fraction for radiobiological modeling.

2.2.2.4 Dose escalation

Although excellent local control rates have been reported for acoustic neuroma treated with SRS and SRT, the control rates decrease in long-term follow up, particularly for larger tumors[87,88]. Therefore, there may be benefits to dose escalation if normal tissue complication rates remain low. A dose escalation study was performed to evaluate whether 4π radiotherapy could achieve higher tumor control rates without increasing the risk of hearing loss for acoustic neuroma patients. The prescription doses for each plan were escalated until the plans achieved TCP values of 99.5%. The NTCP values for SNHL at 3 and

5 years post-treatment were then calculated for the escalated dose distributions and compared for the clinical and 4π plans.

2.2.3 Results

2.2.3.1 Plan comparison

The OAR doses and conformity measures for both plan types are given in Table 2-7 and Figure 2-6. The mean cochlear dose was significantly reduced with 4π from 6.29 Gy to 4.25 Gy for SRS plans, from 11.20 Gy to 8.00 Gy for SRT plans, and from 30.88 Gy to 20.93 Gy for IMRT plans. The maximum cochlear dose was also significantly reduced by 1.58 Gy (20%), 2.2 Gy (15%), and 7.1 Gy (18%) for SRS, SRT, and IMRT, respectively.

In addition, there was significant sparing of the brainstem with 4π, which reduced the mean and maximum doses by 18% and 7%, respectively. These reductions were achieved with a steeper dose gradient around the target, as illustrated by the dose wash in Figure 2-7. The mean and maximum doses to the chiasm were also 39% and 38% lower, respectively, for the 4π plans than for the clinical plans. The mean doses to the eyes, lenses, and optical nerves were reduced by 19% to 56% on average with 4π.

Table 2-7 OAR doses and conformity measures for both plan types

Plan Type		Average OAR Doses (Gy)					V50% (cm^3)	PTV HI	van't Riet CN
		Brainstem	Chiasm	Cochleae					
				SRS	SRT	IMRT			
Clinical	Mean	6.61	2.12	6.29	11.20	30.88	25.23	0.92	0.69
	Max	20.03	3.27	8.05	14.92	38.79			
4π	Mean	5.41*	1.30*	4.25*	8.00*	20.93*	24.85	0.93	0.73
	Max	18.59*	2.04	6.47*	12.72*	31.74*			

*Statistically significant difference from the clinical plans (2-tailed t-test, $p<0.05$)

(CN: conformation number; HI: homogeneity index; max: maximum; V50%: volume receiving 50% of the prescription dose)

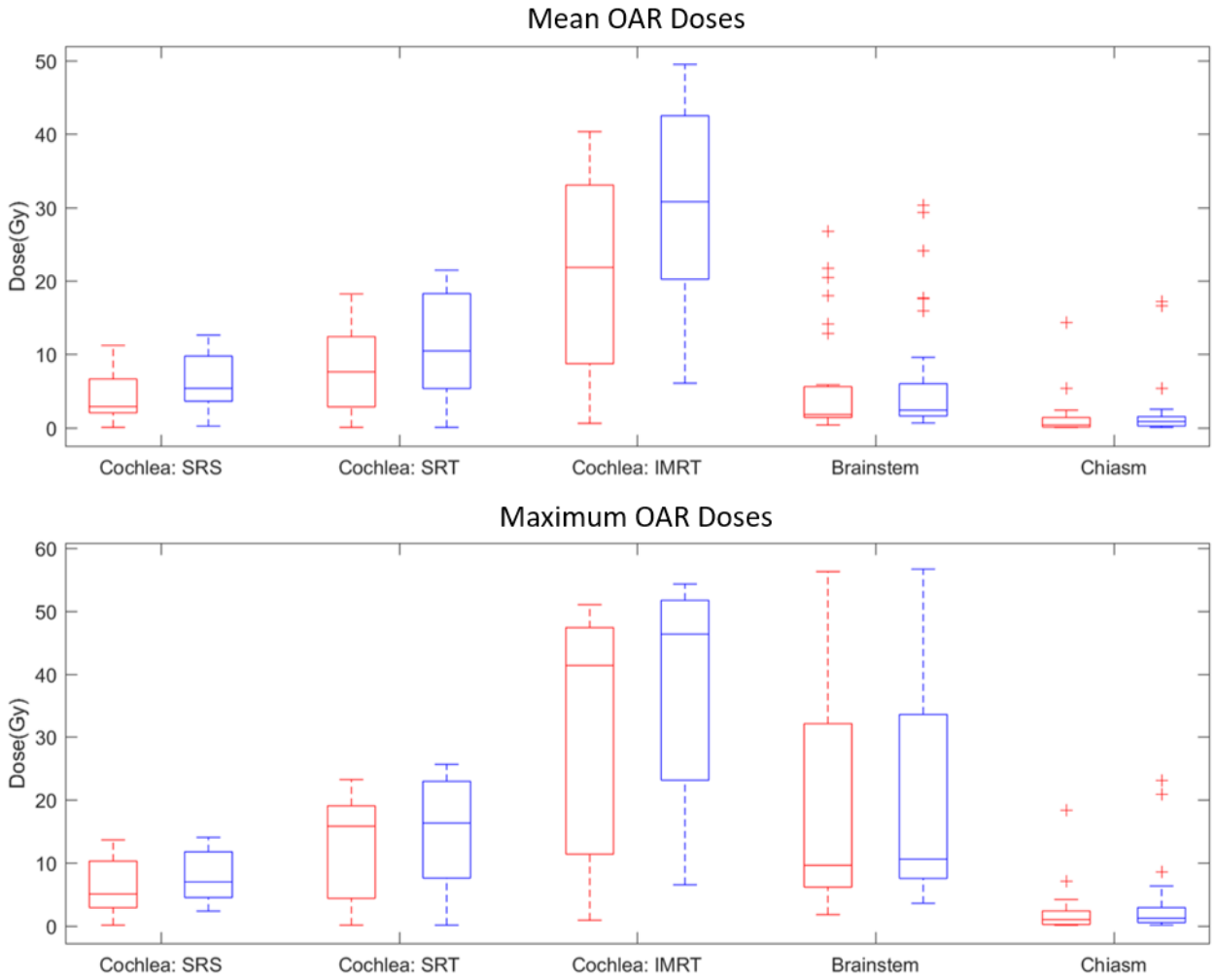

Figure 2-6 Mean (top) and maximum (bottom) doses to the cochlea (SRS, SRT, and IMRT groups), brainstem, and chiasm with the 4π plans (red) and clinical plans (blue). All differences between the 4π and clinical plans were statistically significant (2-tailed t-test, 5% significance level), except the maximum dose to the chiasm.

The conformity measures were essentially the same between the clinical and 4π plans. The average V50% was 0.38 cm^3 lower for the 4π plans than for the clinical plans. The 4π plans were also able to maintain similar PTV coverage despite the major reductions in OAR doses, as illustrated in the dose volume histogram shown in Figure 2-8. The average R_{100} ratio was better for the 4π plans (1.32 vs 1.41) as well as the van't Riet conformation number (0.73 vs 0.69). There was also a statistically significant increase in the PTV homogeneity index with 4π (0.93 vs 0.92). The total monitor units for each plan were, on average, 2248 for the 4π plans and 1561 for the clinical plans.

4π consistently improved the cochlea sparing compared with IMRT, DCAT, and VMAT patient subcohorts. The mean cochlea dose was reduced by 32.2%, 26.8%, and 35.1%, respectively. The maximum cochlea dose was reduced by 19.4%, 11.3%, and 21.3%, respectively.

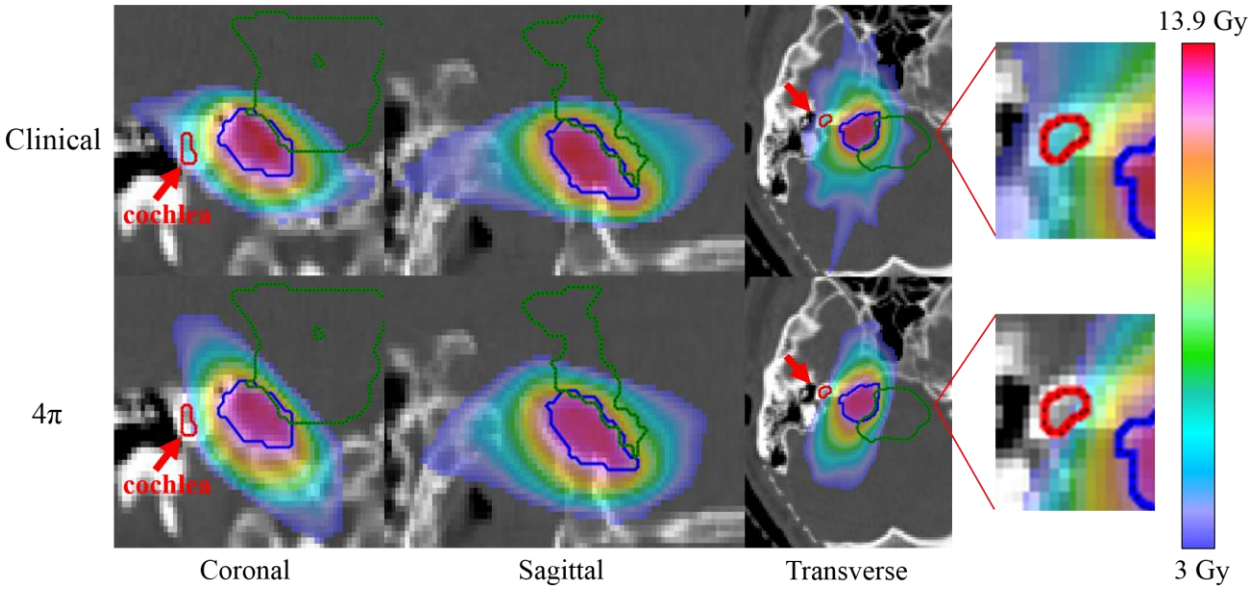

Figure 2-7 Dose color wash for a patient (patient 3 in Table 2-5) who was treated to a prescription dose of 12 Gy in a single fraction. Structures: PTV (blue), brainstem (green), and cochlea (red).

The results of the radiobiological modeling study are given in Table 2-8. Although the difference was statistically significant, the TCP was only 0.3% higher for the clinical plans than for the 4π plans. This difference can be explained by the significantly greater hotspots within the PTV for the clinical plans because all plans were normalized for the same target coverage. The estimated TCP is consistent with clinical reports, in which prescription doses of at least 12 Gy for SRS and 50 Gy for IMRT yielded TCP values of >90%[68-71]. All NTCP predictions for SNHL were significantly higher for the clinical plans than for the 4π plans. The average NTCP was 10.0% higher for the clinical plans at 3 years and 18.4% higher at 5 years post-treatment.

Table 2-8 Results of the radiobiological modeling and dose escalation study

Plan Type	**Average TCP**	**Average SNHL NTCP**		**Average Escalation Factor**	**Escalated SNHL NTCP**	
		3 years	5 years		3 years	5 years
Clinical	95.7 ± 0.9%	40.8 ± 5.9%	61.7 ± 10.8%	1.162 ± 0.02	43.4 ± 6.3%	64.7 ± 11.1%
4π	95.4 ± 0.9%*	30.8 ± 5.3%*	43.3 ± 11.2%*	1.166 ± 0.02*	32.6 ± 5.5%*	46.4 ± 11.3%*

*Statistically significant difference from the clinical plans (2-tailed t-test, $p<0.05$)

(TCP: tumor control probability; SNHL: sensorineural hearing loss; NTCP: normal tissue complication probability)

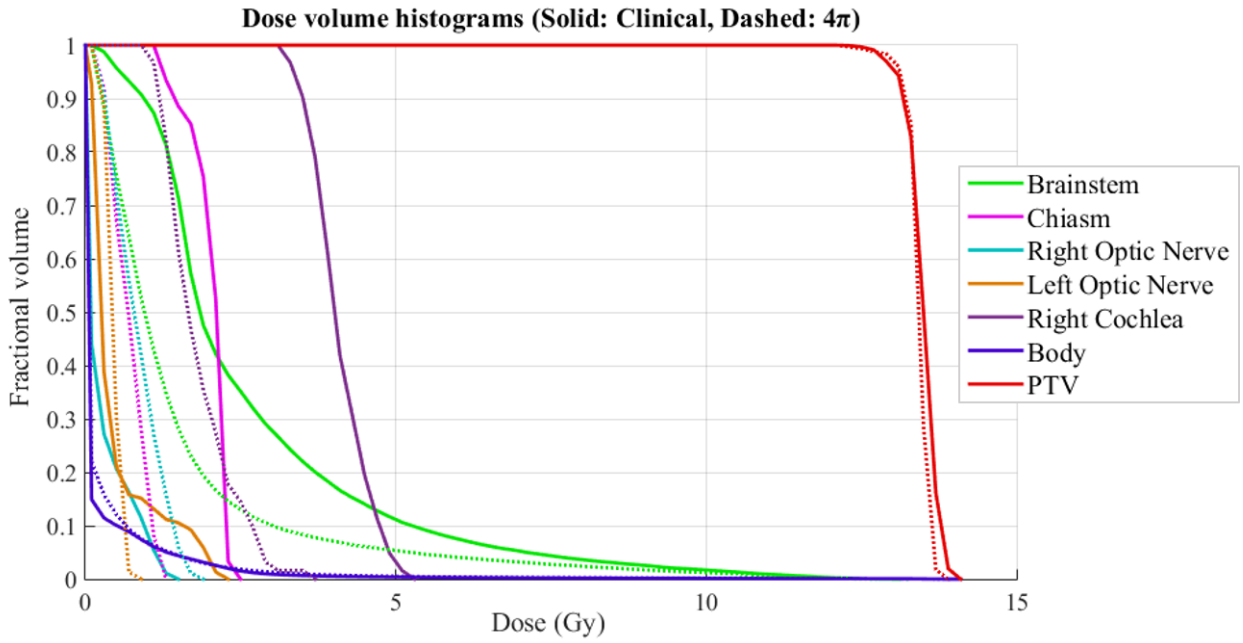

Figure 2-8 Dose volume histograms (solid line: clinical plan; dashed line: 4π plan) for one of the patients who received SRS in this study (patient 2 in Table 2-5) with a prescription dose of 12 Gy.

2.2.3.2 Dose escalation

To achieve a TCP of 99.5%, the prescription doses had to be escalated by a factor of approximately 1.16 on average for both plan types. After dose escalation, the probabilities of post-treatment SNHL at 3 and 5 years were once again significantly lower for the 4π plans, by 10.8% and 18.3%, respectively. The average NTCP for the escalated 4π plans was 8.2% lower than the normal (non-escalated) clinical plans at 3 years post-treatment, and 15.4% lower at 5 years.

2.2.4 Discussion

Although normal tissue complications are a concern for every patient receiving radiation therapy, these risks must be weighted even more heavily for the treatment of benign tumors such as acoustic neuroma. The majority of these patients will have an unaffected life expectancy, and any radiation-induced side effects could have a lasting impact

on quality of life that competes with the benefits of treatment. In addition, acoustic neuroma is a highly treatable disease. Therefore, despite high treatment success rates, technological improvement should not stop until 100% local control is achieved because uncontrolled tumor growth may ultimately compromise patient hearing and other neurological functions. While excellent local control (>98%) can be achieved with surgical resection, this treatment option carries significant risks in addition to hearing loss. Over 20% of surgical patients experience complications such as facial paralysis, neurologic damage, CSF fistula, hematoma, hydrocephalus, and even death[61-63].

Radiosurgery is increasingly chosen over surgery as a noninvasive treatment option, but there are still a significant number of cases in which the treatment either fails to control the tumor growth or the tumor eventually recurs. Surgical resection is typically the next course of action in these cases because further radiation therapy would exceed normal tissue dose tolerances. In a study by Yomo et al on repeat radiosurgery for acoustic neuroma patients, two patients required as many as three Gamma Knife treatments (with prescription doses of 12, 12, and 14 Gy) before achieving tumor control[89]. None of the patients in this study maintained useful hearing after receiving repeat radiosurgery. Although an initial target dose of 12 Gy was clearly insufficient for achieving or maintaining tumor regression in these patients, the delivery of larger single-fraction doses is typically limited by normal tissue tolerances.

Using noncoplanar conformal and dynamic arcs on a modern linac, dose conformity nearly as good as that with Gamma Knife can be achieved, without the toxic high maximal doses[82,83]. As demonstrated in this study, 4π radiotherapy can enable statistically significant

reductions in both mean and maximum normal tissue doses, particularly to the cochlea and brainstem. As previously mentioned, clinical studies have found that patients who receive <4.2 Gy single fractional doses to the cochlea experience significantly better hearing preservation than patients who receive >4.2 Gy.

Our study shows that for patients treated with a single fractional SRS dose, the mean cochlear dose can be reduced from 6.29 Gy to 4.25 Gy, allowing potentially significant reductions in hearing loss. On the other hand, we showed that prescription doses for the 4π plans can be escalated to achieve 99.5% tumor control while maintaining hearing loss probabilities below the non-escalated clinical plans. The ability to safely escalate prescription doses would likely reduce the incidence of tumor recurrence and the need for subsequent tumor resection or secondary radiation, both of which carry major risks of hearing loss or other complications.

In this study, heterogeneous planning techniques including conformal arc, IMRT, and VMAT were used clinically, mainly depending on the size of the tumor. Conformal arcs are typically used on smaller tumors, while larger tumors benefit from the better dose homogeneity and conformity that can be achieved with intensity modulation in static IMRT and VMAT. Nevertheless, 4π radiation therapy resulted in consistently improved cochlea sparing in individual planning technique comparisons.

The noncoplanar beams were not actually delivered in this study. However, in a separate prospective clinical study[85], a similar number of beams were delivered to patients with brain tumors. In this study, the beams were ordered on the basis of their couch rotation angles. That way, the treatment could be delivered in a single couch sweep while the gantry

rotated back and forth under the guidance of pretreatment modeling[40]. With remote manual machine operation, the treatment delivery time was less than 35 minutes. In the phantom test using fully automated machine control that has not been approved for patients, the same treatment could be delivered in <15 minutes. We expect similar treatment times for patients with acoustic neuroma.

2.2.5 Conclusions

4π radiotherapy achieves significantly greater normal tissue sparing compared with radiotherapy techniques that are typically used in acoustic neuroma treatment. These major reductions in cochlear dose may reduce the risk of normal tissue complications such as hearing loss and enable the safe escalation of prescription doses to potentially improve tumor control rates.

2.3 4π Plan Optimization for Cortical-Sparing Brain Radiotherapy[28]

2.3.1 Introduction

Thinning of the cerebral cortex has been observed in patients treated with fractionated partial brain radiation therapy and may contribute to cognitive decline following treatment. The extent of this thinning is dose-dependent, as illustrated in Figure 2-9, and has been shown comparable to that of neurodegenerative diseases such as Alzheimer's disease at one year post-therapy[90].

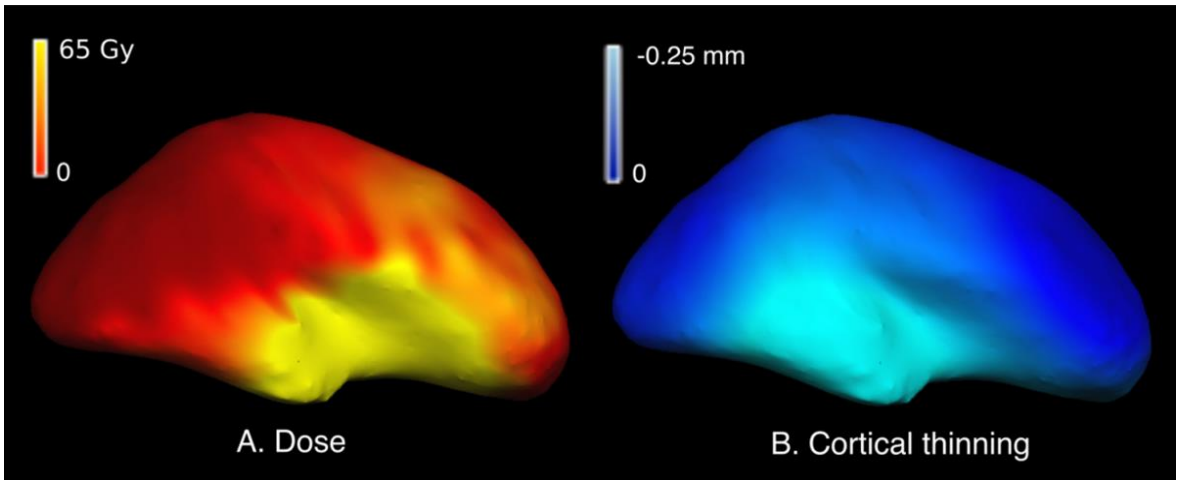

Figure 2-9 A representation of the cortical surface from Karunamuni et al[90] showing the dose delivered (A) and the extent of cortical thinning one year post-irradiation (B) for an example patient.

The objective of this study was to investigate whether 4π radiotherapy can enable better sparing of the cerebral cortex and other critical structures when compared to conventional clinical IMRT plans. This could potentially reduce the degree of cortical thinning, and subsequent neurocognitive decline, observed in high-grade glioma patients following radiation therapy.

2.3.2 Methods

2.3.2.1 Patient population and treatment

This retrospective study was approved by the institutional review board. The patient cohort consisted of nine male and four female subjects (median age 60 years, range 40-77) with high grade glioma. Patients were treated on a 6 MV TrueBeam (Varian Medical Systems, Palo Alto, CA) linear accelerator with a 120-leaf Millennium MLC to a prescription dose of 59.4 Gy (N=1) and 60 Gy (N=12) in 33 or 30 fractions, respectively. All patients' original clinical plans were six to eight noncoplanar field, fixed-gantry, sliding-window IMRT. The original IMRT plans were obtained and re-planned with 4π radiation therapy optimization.

2.3.2.2 Radiation planning objectives

The original fixed gantry IMRT plans were optimized to meet clinical objectives for PTV coverage and standard OARs (including brainstem, optic structures, and spinal cord) at the time of treatment. Dose constraints matched guidelines set by RTOG 0825[91], including maximum doses of <60 Gy to the brainstem, <55 Gy to the optic nerves, and <56 Gy to the optic chiasm. Beam arrangements for these plans were selected by the treating physician and dosimetry team to most effectively achieve the planning goals for each case. These original clinical plans were not optimized for cortical sparing. For each case, two new plans were created to spare the cortex: IMRT-optimized and 4π-optimized. Cortical sparing for the IMRT-optimized plans was performed to minimized cortical volume outside the PTV receiving doses higher than 30 Gy[92], with the highest priority given to the cortex. In 4π planning the highest constraint for each case was also placed on the normal cortex, with the

other OARs prioritized based on proximity to the tumor. The overarching goal was to minimize OAR doses while matching the primary objective for PTV coverage in the original plan. The same objectives and priorities were used for the cortical-sparing IMRT plans and cortical-sparing 4π plans. Doses in all plans were normalized to deliver 100% of the prescription to 95% of the PTV volume.

2.3.2.3 4π optimization

The 4π treatment planning process is a highly noncoplanar and non-isocentric system developed on C-arm gantry linear accelerators, and has been described in detail previously[8-10,26,93]. Briefly, the 4π planning process began with 1162 candidate beams evenly distributed throughout the solid sphere angle space, with 6° separation between beams. A CAD model of the Varian TrueBeam linear accelerator with a 3D-scanned human surface model positioned on the couch was utilized to exclude any beams causing a collision between the gantry and couch or patient[40]. Dose contribution matrices with 2.5 x 2.5 x 2.5 mm^3 resolution were computed for each of the candidate beams using convolution/superposition of a 6 MV polyenergetic x-ray kernel. A greedy column generation algorithm with defined upper dose constraints and structure priority weighting, was used to iteratively select 20 beam orientations, such as those shown in Figure 2-10, and perform fluence map optimization. To compare with the clinical plans without any bias from different dose calculation methods, the optimal beam orientations were then imported into Eclipse for dose recalculation using an identical dose calculation engine and resolution.

2.3.2.4 Dosimetric comparison

The mean and maximum dose to the cerebral cortex and other OARs were compared for the two cortical-sparing plan types, as well as the conformity index (CI), homogeneity index (HI), and 50% dose spillage volume (R_{50}) to assess the target coverage and dose spillage. CI was defined as the ratio of the volume receiving the prescribed dose to the volume of the PTV, and HI as the ratio of the 95% and 5% isodose volumes. R_{50} was defined as the ratio of the 50% isodose volume to the PTV volume.

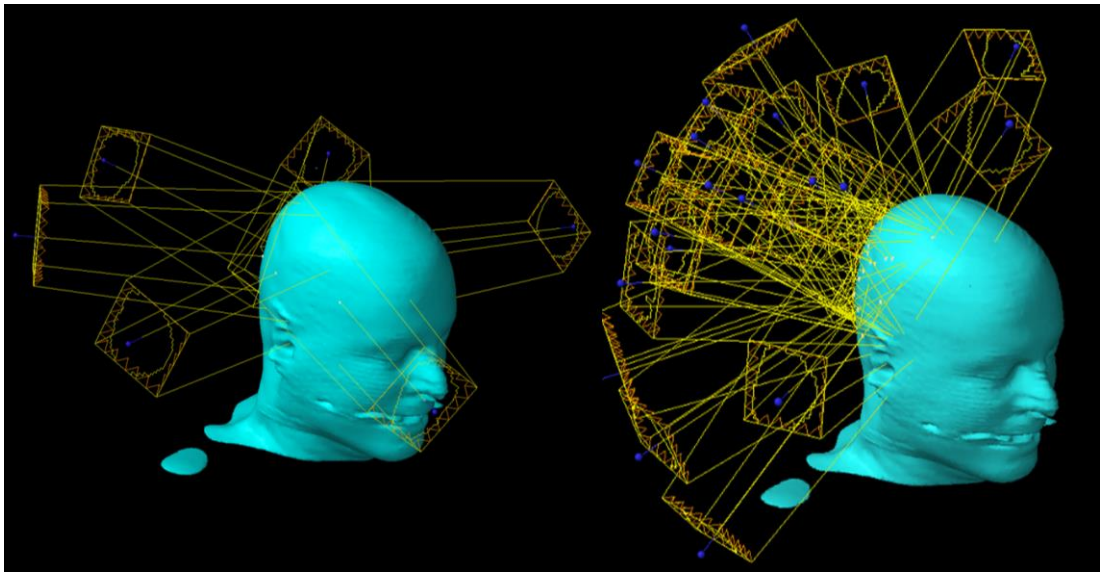

Figure 2-10 Orientation of the beams used in the clinical IMRT plan (left) and the 20 optimal beams selected by the 4π algorithm (right) for one patient in the study.

2.3.3 Results

As shown in Table 2-9, the 4π plans significantly reduced the mean cortical dose by an average of 15% (ranging from 6% to 27%) compared to the clinical plans. The mean dose to every other OAR compared was also reduced by 15% to 42%, with statistically significant reductions to the brainstem, chiasm, right eye, optic nerves, subcortical white matter, and hippocampus. The average maximum doses were also reduced for 10 out of the 12 OARs

compared, with statistically significant reductions in the maximum dose to the brainstem, chiasm, hippocampus, and subcortical white matter. These significant reductions in OAR doses are evident in the dose volume histograms for one representative patient (Figure 2-11) and averaged over all patients in the study (Figure 2-13). The R_{50} was significantly reduced with the 4π plans by over 14%. This significant reduction in high dose spillage is also evident in the dose washes shown in Figure 2-12, particularly in the axial view.

Table 2-9 Dose statistics for clinical and 4π plans for the 15 high-grade glioma patients in this study

Plan Type		**Average OAR Doses (Gy)**						**Body Mean (Gy)**	**PTV Min (Gy)**	**R_{50}**	**Homogeneity Index**	**Conformity Index**
		Brain	Brainstem	Chiasm	Hippocampus	Subcortical White Matter	Cortex					
Clinical	*Mean*	19.7	18.6	20.1	23.1	16.3	15.5	8.5	51.6	4.4	0.84	1.73
	Max	45.5	28.4	29.1	49.6	54.0	53.0					
4π	*Mean*	12.9	12.8*	12.2*	14.6*	13.8*	13.1*	8.0*	52.5	3.8*	0.86*	1.72
	Max	49.3	37.2*	20.5*	45.0*	52.7*	53.1					

*Significantly lower dose (or higher homogeneity) than the clinical plans (2-tailed t-test, $p<0.05$)

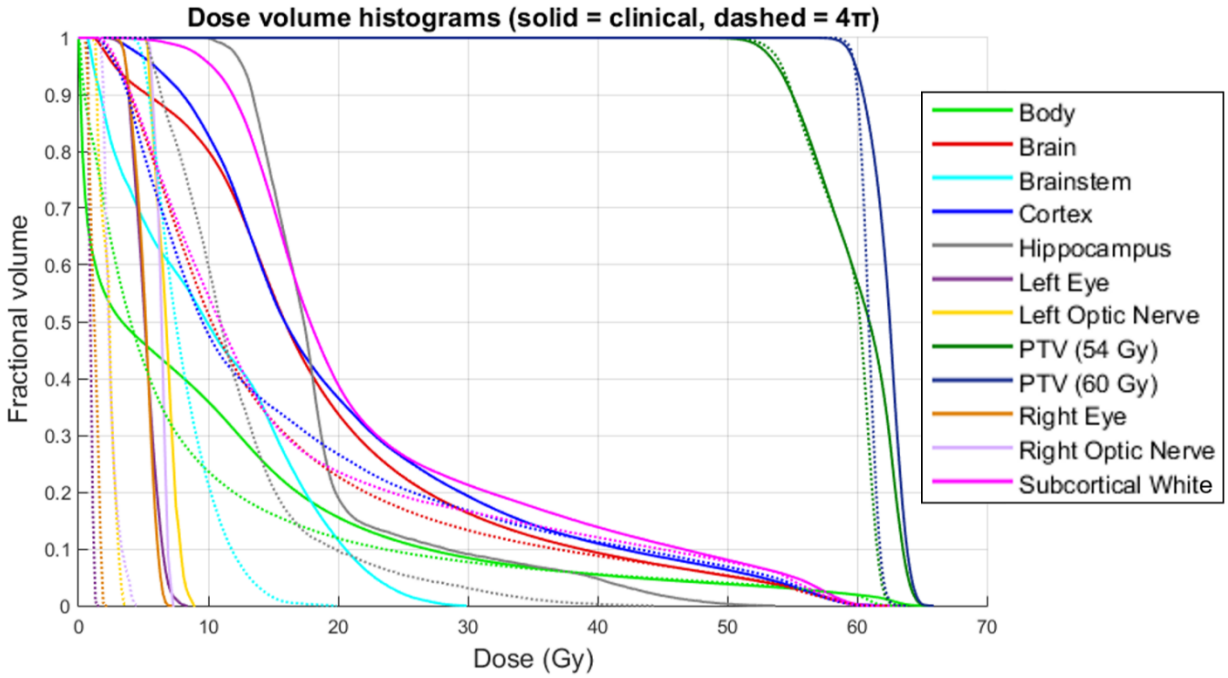

Figure 2-11 Dose volume histograms of the 4π (dashed) and clinical (solid) plans for the patient in Figure 2-10.

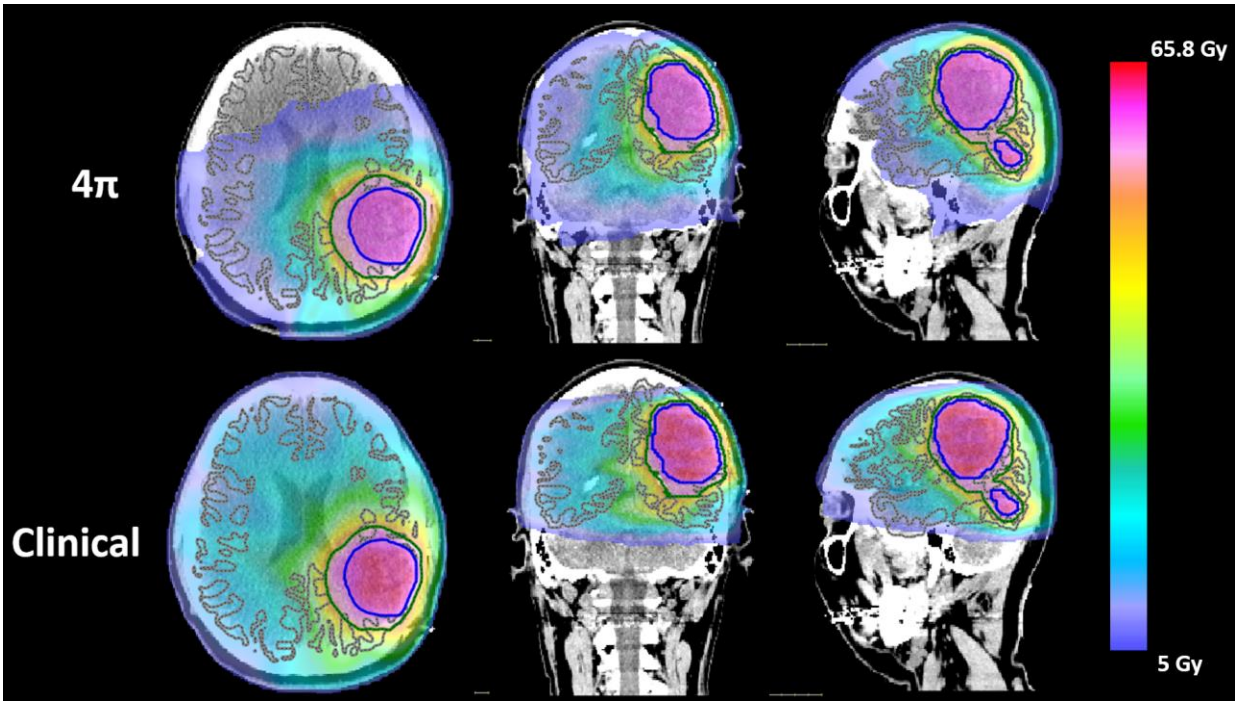

Figure 2-12 Dose washes of the 4π and clinical plans for the patient in Figure 2-10. Structures: 54 Gy PTV (green), 60 Gy PTV (blue), and cerebral cortex (gray).

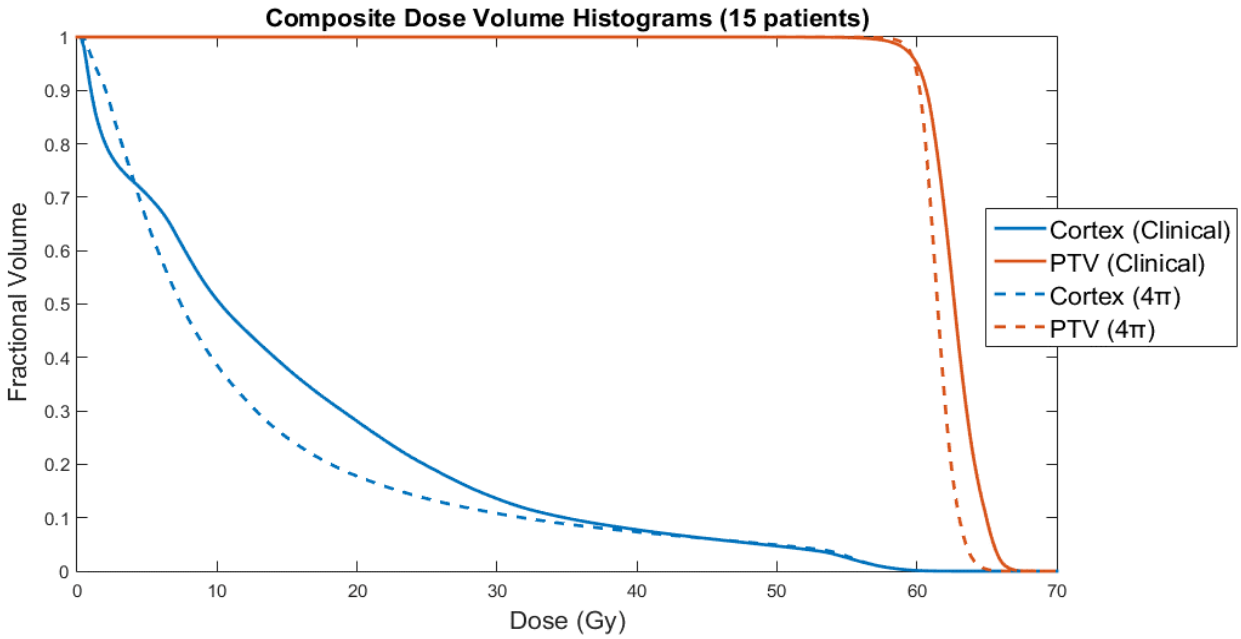

Figure 2-13 Dose volume histograms of the cortex and PTV (60 Gy prescription level) for the 4π (dashed) and clinical (solid) plans averaged over all 15 patients.

2.3.4 Discussion

Reducing the volume of incidentally irradiated normal brain structures in brain radiotherapy may help to lower the probability of cortical, white matter, and hippocampal damage that could lead to neurocognitive deficits. A previous study showed that cortical sparing was feasible by heavily prioritizing cortical dose in standard IMRT planning[92]. This study investigated whether the cortical dose could be further reduced using new planning methods without compromising other planning metrics such as PTV dose homogeneity. Cortex-sparing IMRT plans were compared to 4π-optimized IMRT plans, and 4π improved sparing of all standard OARs, including the brainstem and optic structures. 4π also significantly reduced the volume of the cortex receiving over 30 Gy, and since doses over 30 Gy increase (by 20% or greater) the probability of severe cortical thinning[92], 4π-optimized IMRT has the potential to lower cortical injury.

In whole brain radiotherapy patients, dose to the hippocampus is hypothesized to cause post-treatment decline in verbal memory[94], and a recent quantitative MRI study reported dose-dependent hippocampal atrophy after brain radiotherapy[95]. Notably, even though none of the plans were optimized with respect to the hippocampus, 4π significantly reduced the mean dose to the hippocampus by 37% compared to the cortical-sparing IMRT, suggesting that this technique would also be helpful for hippocampal sparing. Also, while cortical sparing in optimized IMRT was achieved at the price of increased inhomogeneity of PTV coverage, 4π optimization allowed for better cortical sparing without significant reductions in homogeneity. The reduced dose to the hippocampus and white matter with 4π appears to be an additional benefit of limiting dose spillage outside the PTV.

2.3.5 Conclusions

4π radiation therapy, which utilizes optimized highly noncoplanar beam orientations, has been shown to enable significant sparing of the cerebral cortex, as well as other critical structures, when treating high-grade gliomas. Previous research suggests that this could reduce the risk of harmful dose-dependent cortical thinning, which may be the cause of neurocognitive decline observed in such patients following radiation therapy.

3 Dosimetric Evaluation Tools for Preclinical Radiotherapy

3.1 Small Animal Irradiation Standardization Project

3.1.1 Introduction

Despite significant advances in the field of radiation biology, many of the biological effects of radiation exposure have yet to be explained. The most widely used research tools for studying these mechanisms are small animal models, particularly the mouse model[16,17]. Over recent years, more advanced small animal irradiation systems have been developed that enable image guidance and feature dedicated treatment planning systems for more precise dose calculations[96,97]. These new capabilities could greatly expand the potential for preclinical studies, enabling much higher dosimetric and geometric precision[98]. However, because this technology is relatively new, there is a significant lack of standardization across different small animal radiotherapy platforms and different research institutions[99]. One of the goals of the Radiation Physics Core of the UCLA Center for Countermeasures against Radiation (CMCR)[100] is to evaluate and mitigate these inconsistencies in small animal dosimetry.

3.1.2 Methods

3.1.2.1 Phantom development

First, cylindrical phantoms were developed that are simple to manufacture but also incorporate some tissue heterogeneity for mimicking the mouse anatomy. These phantoms are similar in size to a typical mouse (3 cm diameter and 10 cm long) and are made of polystyrene that can be split at the center for the insertion of dosimeters and radiochromic film. Polystyrene has a density of 1.02 g/cm^3, which is close to that of soft tissue. These phantoms also have higher density "bone" inserts (Teflon rod, 2.2g/cm^3) for the spine and legs and low density inserts (0.3 g/cm^3 Polyurethane rod, McMaster-Carr) for the lungs (see Figure 3-1). The phantom has triplet TLD slots in five different locations in the head, chest, abdomen, and pelvis, and room for six additional TLDs in the lungs. Radiochromic film is cut with a digital film cutter (Silver Bullet) to fit between the two phantom halves.

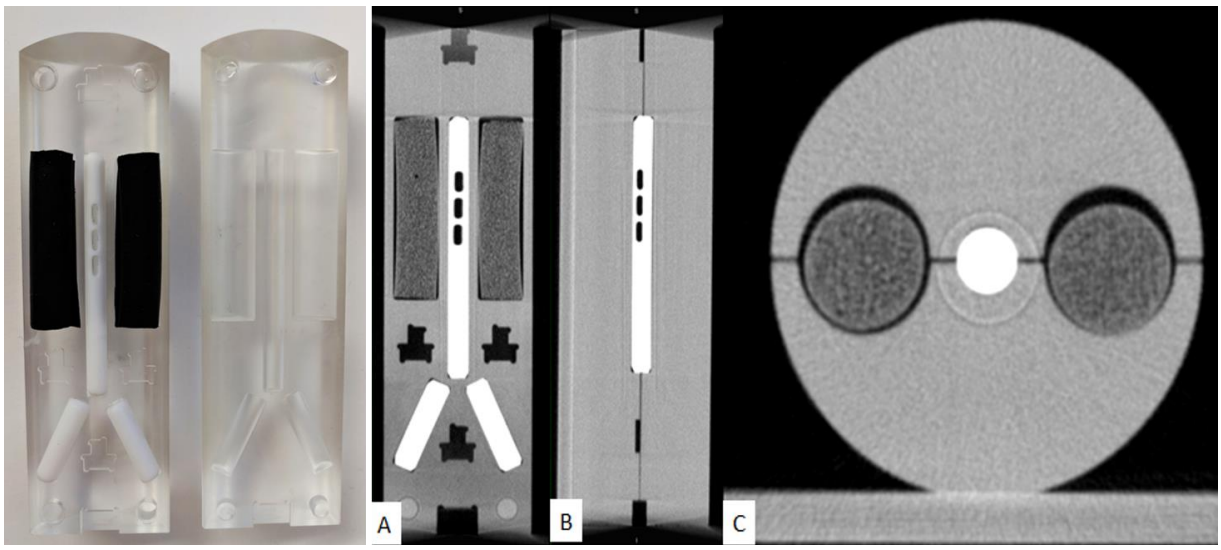

Figure 3-1 Photograph (left) and CT scan (right: coronal view of the lower (A) and upper (B) phantom halves; axial view through the lungs (C)) of the cylindrical polystyrene mouse phantoms, with higher density inserts in the spine and legs and lower density foam inserts in the lungs. It has groups of three TLD slots in the head, spine, left and right abdomen, and pelvis. Custom die-cut film is inserted between the two halves.

A mouse phantom with a more anatomically accurate shape was also developed, which we refer to as “mousemorphic”. A CAD model was created based on micro CT of a C57B1/6 mouse and split along the midcoronal plane for dosimeter insertion. Three different versions of the phantom were created with slots for thermoluminescent dosimeters (TLDs), optically stimulated luminescent dosimeters (OSLDs) or Alanine dosimeters. The CAD models for all three phantom types are shown in Figure 3-2. These mousemorphic phantoms, shown in Figure 3-3, were first printed using fused deposition modelling (FDM) 3D printing with acrylonitrile butadiene styrene (ABS) filament on the MakerGear M2 printer. ABS is close to tissue-equivalent, with a density of 1.04 g/cm^3. Initial dosimetric calibration was performed using a 225 kVp x-ray machine with Monte Carlo dose calculation. Using the SmART Advanced Treatment Planning (ATP) System (SmART Scientific Solutions, Maastricht, Netherlands) and assuming tissue equivalency of ABS in the Monte Carlo simulation (SmART Plan version 1.3, pegs 4 material Tissue), the measured dose was 1.2% off from the calculated dose, as shown in Figure 3-4, suggesting that ABS mousemorphic phantoms are good surrogates for dosimetric testing. Inter-phantom variation, assessed by weight, was less than 0.5%, suggesting consistent print density and dimensions. These ABS phantoms were used for all institutional dosimetry measurements in this study.

A second version of the mousemorphic phantom was printed on the Formlabs Form 2 stereolithography (SLA) 3D printer with Flexible Resin, which enabled higher print resolution and success rates (Formlabs, Somerville, MA). This material is also very radiographically similar to tissue, with average Hounsfield Unit (HU) measurements differing by <2% compared to tissue measurements from real animal CT data. These

measurements are shown and further discussed in section 3.2, and the printed phantom is shown later in Figure 5-9.

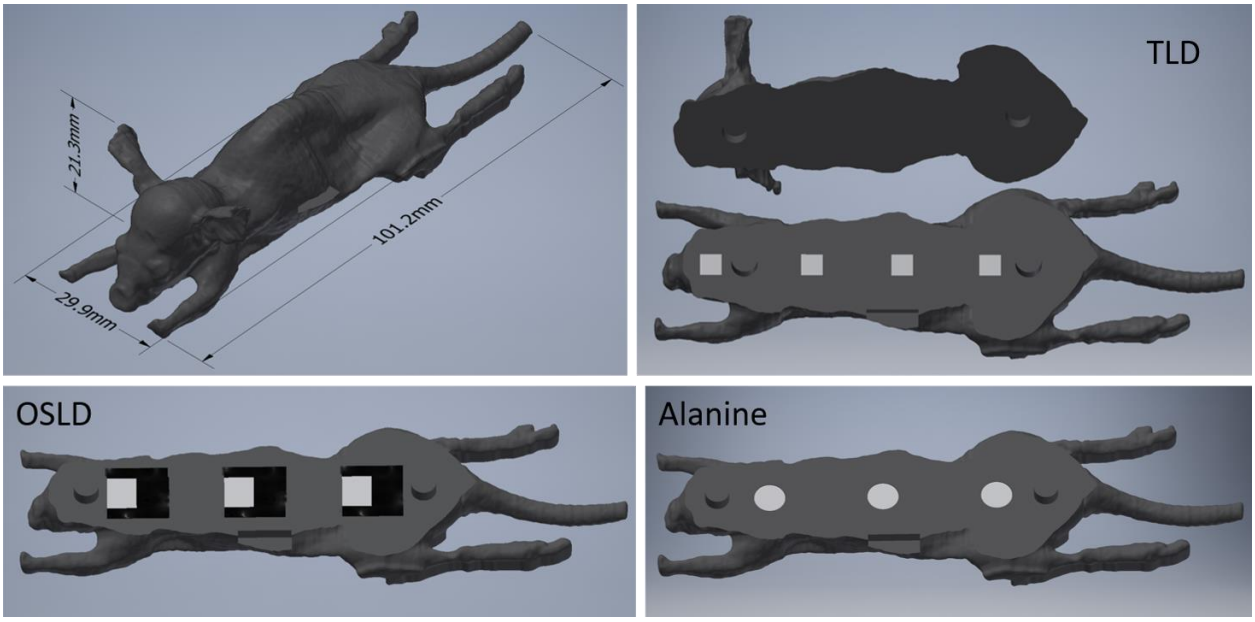

Figure 3-2 CAD models of the full mousemorphic phantom with dimensions (upper left) and the design variations for TLD, OSLD, and Alanine dosimetry.

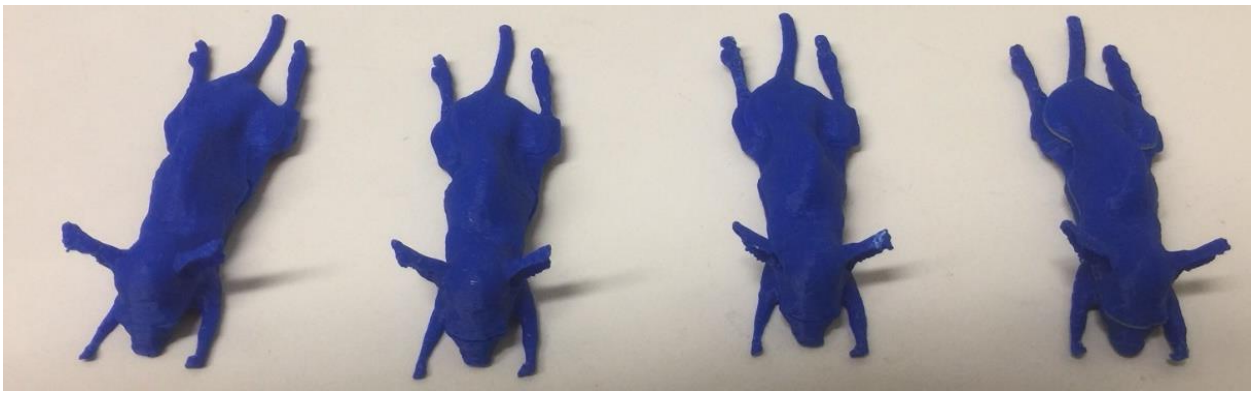

Figure 3-3 Phantoms 3D printed out of ABS from the CAD model shown in Figure 3-2. The weight of the phantom is 24.5 ± 0.1 g.

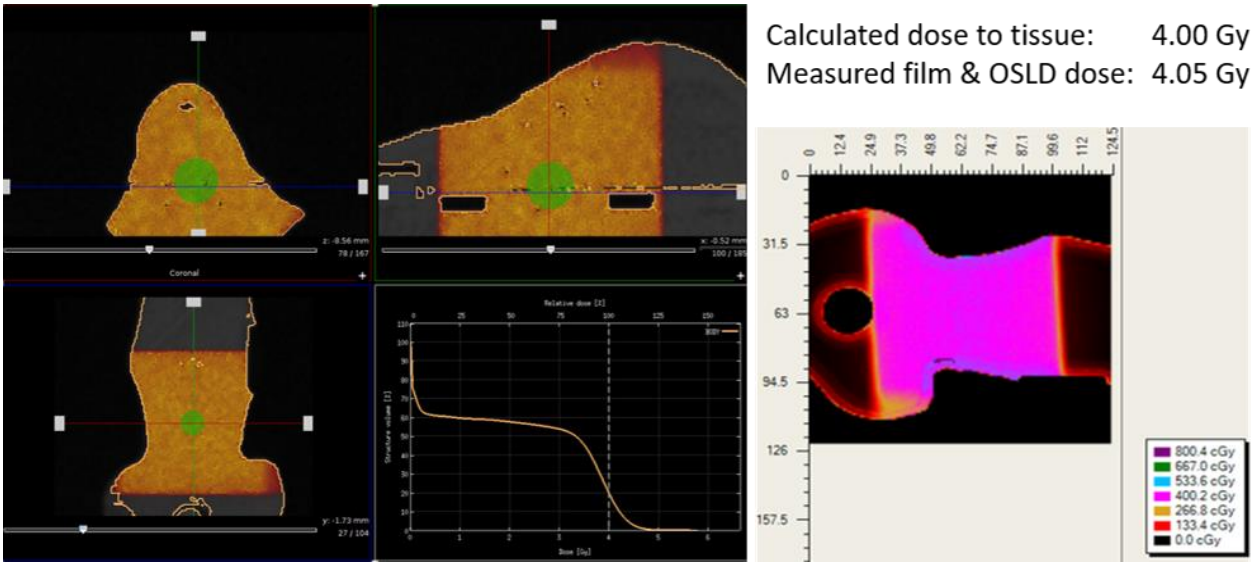

Figure 3-4 Monte Carlo dose calculation in the SmART-ATP system assuming tissue equivalence (left) and measured phantom film dose (right).

3.1.2.2 Dosimeter calibrations

Calibration curves were then developed for TLD, OSLD, and EBT3 film dosimetry for the standardization surveys described in the following section. A wide range of photon energies are used for small animal irradiation, which is one of the challenges with standardization. This variation was reflected in these surveys, which included systems using 225 to 320 kV x-ray tubes, 6 MV linear accelerators, and Cs-137 sources. In order to accurately compare the measurements between these systems, energy correction factors were also derived for each type of dosimeter.

TLDs

TLDs were first annealed using the procedure recommended by Yu et al[101] (400°C for 1 hour, followed by 105°C for 2 hours). These annealed TLDs were irradiated at calibration doses of 0, 1, 4, 8, and 16 Gy, and a pre-readout anneal was performed (105°C for 15 minutes, then cooled for 5 minutes). The TLDs were then read out and a quadratic

calibration curve was created with the measurements. Energy correction factors were calculated using literature data[102] and a decay factor of $3x10^{-4}$ Gy/day was used to correct for time between irradiation and readout.

OSLDs

The Landauer microSTARii Medical Dosimetry System was used for the calibration of the nanoDot OSLDs. Screened nanoDots, which had been individually tested to ensure high accuracy in sensitivity determination (±5.5%) were used for all calibration and measurements. A high dose nonlinear calibration was created for a 225 kVp x-ray beam using the SmART. Three screened nanoDots were irradiated at 225 kV to each dose level: 0.5, 1, 3, 5, 8, 10, and 13 Gy. The irradiation was performed using 305.4 mm SSD, 4 x 4 cm collimator, large focal spot, and 0.32 mm Cu filtration. Each nanoDot was then measured four times using the microSTARii system, and a standard deviation of <0.05 across all sensitivity-corrected counts for each dose level was verified before accepting the calibration. This calibration was used for reading out OSLDs irradiated with 225 to 320 kV photons. Correction factors for energies >225 kV, given in Table 3-1, were determined from data provided by Landauer.

Landauer also supplied calibration sets for 80 kVp and Cs-137, with nanoDots irradiated to 0.5, 3, 50, and 100 rad (with three nanoDots at each dose level). Low dose linear calibrations were created for each energy using the process above. This higher energy calibration was used for OSLDs irradiated with Cs-137 or 6 MV photons.

Film

Gafchromic EBT3 film (Ashland Inc., Covington, KY) was irradiated on the SmART system at 225 kV to doses of 0, 1, 2, 4, 6, 8, 10, 12, 14, 16, 18, and 20 Gy (although fewer calibration points could have been used). The film was scanned on an Epson 10000XL scanner with a resolution of 96 dpi in 48-bit RGB (red, green, and blue), and Ashland's FilmQA Pro software was used to create the calibration curve and to perform all subsequent film measurements. EBT3 film energy response data from the literature[103] was used to calculate the correction factors given in Table 3-1. Film measurements were also corrected for the time between irradiation and measurement (which was significant in some cases due to shipping times) assuming an optical density increase of $5x10^{-4}$/day (if kept in the dark, as instructed).

Table 3-1 Energy correction factors for TLD, OSLD, and EBT3 film measurements

Irradiation Energy	TLD	OSLD		EBT3 Film
		225 kV readout	*Cs-137 readout*	
225 kV	1	1	-	1
250 kV	1.067	1.070	-	0.991
320 kV	1.098	1.204	-	0.970
Cs-137	1.086	-	1	0.909
6 MV	1.114	-	1	0.909

3.1.2.3 Measurement procedure

Each cylindrical and mousemorphic phantom was loaded with custom die-cut pieces of EBT3 film and TLDs or OSLDs. Each phantom pair was then sent out for remote dosimetry to institutions across the country with specific instructions for phantom irradiation to 4 Gy.

After irradiation, the phantoms were shipped back to UCLA along with relevant experimental details such as irradiation energy, system, exposure time, and filtration. The TLDs, OSLDs, and film were measured and corrected for irradiation energy based on the factors given in Table 3-1, as well as the time since irradiation. The survey was then repeated to assess the reproducibility of the dosimetric measurement based on the dose to the cylindrical phantom shown in Figure 3-1. This comparison was based on the average film dose measurements from four tissue-like regions of the phantom, as indicated by the red regions-of-interest (ROIs) on the sample film in Figure 3-5. For the third survey, the necessary change in exposure time was calculated based on the deviation between measured and expected dose and communicated to the participating institutions.

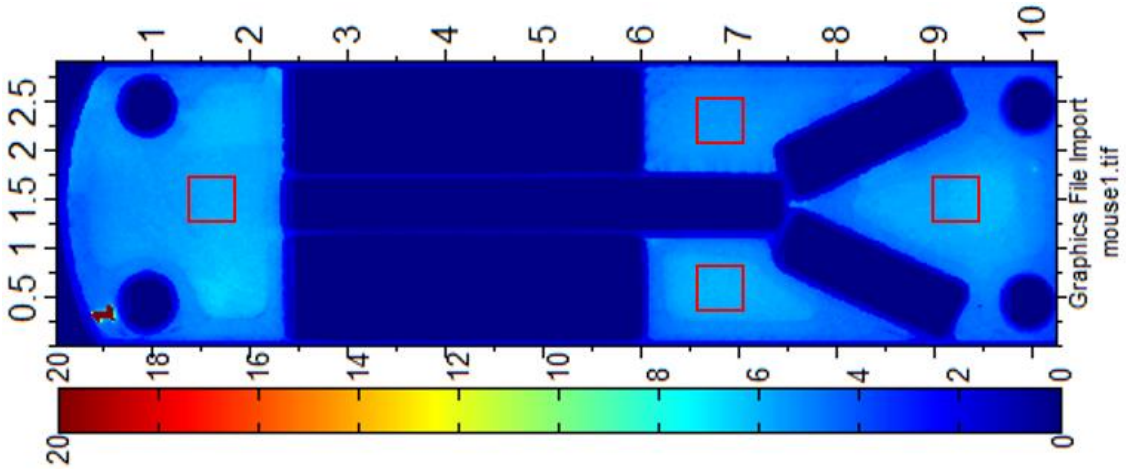

Figure 3-5 Film measurement from one of the cylindrical mouse phantoms. Average dose was measured within the four regions indicated by red squares.

3.1.3 Results and Discussion

Dose deviations of up to 30% were measured in the first two surveys. After modifying exposure times accordingly, all but one center was able to improve the dosimetric deviation from the expected value to within 7%, as shown in Figure 3-6. However, this center later realized that the exposure time was not adjusted according to the revised instructions. They

are now aware of this consistent deviation and will adjust future exposure times accordingly. For irradiator #6, the large dose heterogeneity in the second survey resulted from improper animal setup, which was consistently used at the institution prior to this survey. When this setup error was corrected in the harmonization survey, the heterogeneity was reduced to 2% and the absolute dose error reduced to 1%.

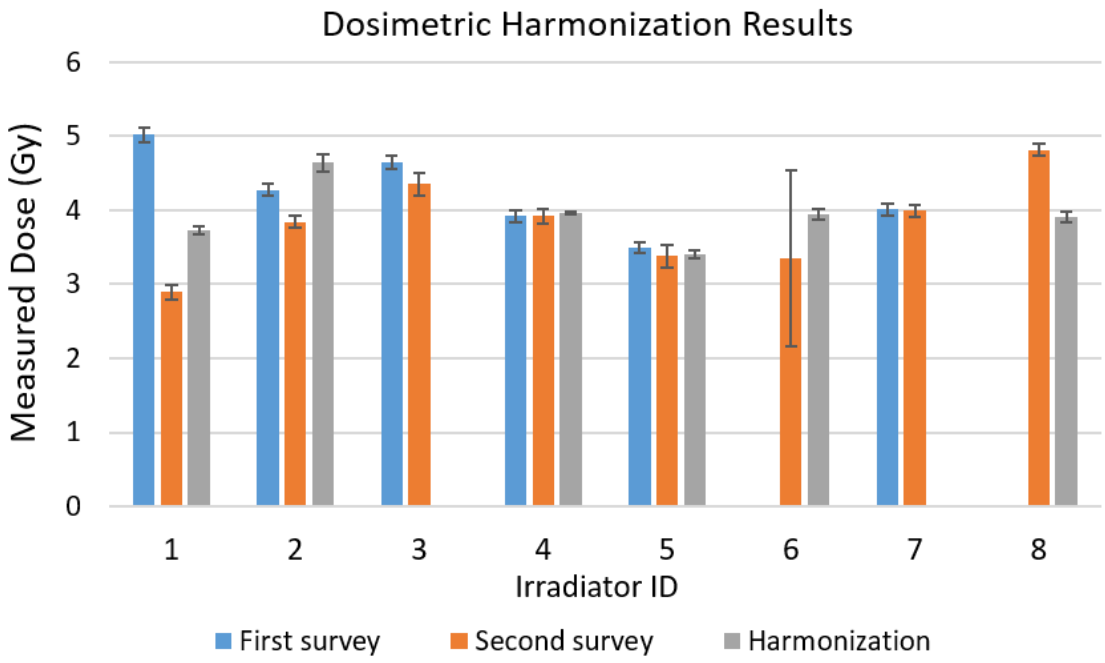

Figure 3-6 Dosimetric harmonization test results. Measured dose is given as the average dose from the four regions-of-interest of the cylindrical phantom film (as shown in Figure 3-5) with error bars indicating the standard deviation. Irradiators #6 and #8 did not participate in the first survey, and the harmonization result of #3 was not valid. The exposure parameter for #5 was not adjusted.

Although these results are fairly consistent, it should be noted that deviations between the film and TLD measurements of up to 20% were observed for a few of the phantoms. This is likely due to uncertainties in energy correction, since these deviations were significantly smaller for exposures at 225 kV (when no corrections were needed). Even

with accurate energy response relationships, there may still be significant uncertainties in this correction due to the unknown energy spectrum of each irradiation system.

To address this uncertainty, a phantom was developed for beam characterization (Figure 3-7). This phantom features five separate regions for TLD and film measurement, with different thicknesses of copper above each region: 0, 1, 2, 3, or 4 mm. The phantom is 3D printed with water-equivalent plastic resin, and there is an equal thickness of plastic above each region. This simple, compact measurement tool (approximately 5 x 5 x 2.5 cm) is designed to be shipped with the mouse phantoms and irradiated under identical conditions. By measuring the dose below each filtration level, we can calculate the relative copper half-value layer (HVL) of the beam and perform a more accurate energy correction (Figure 3-8).

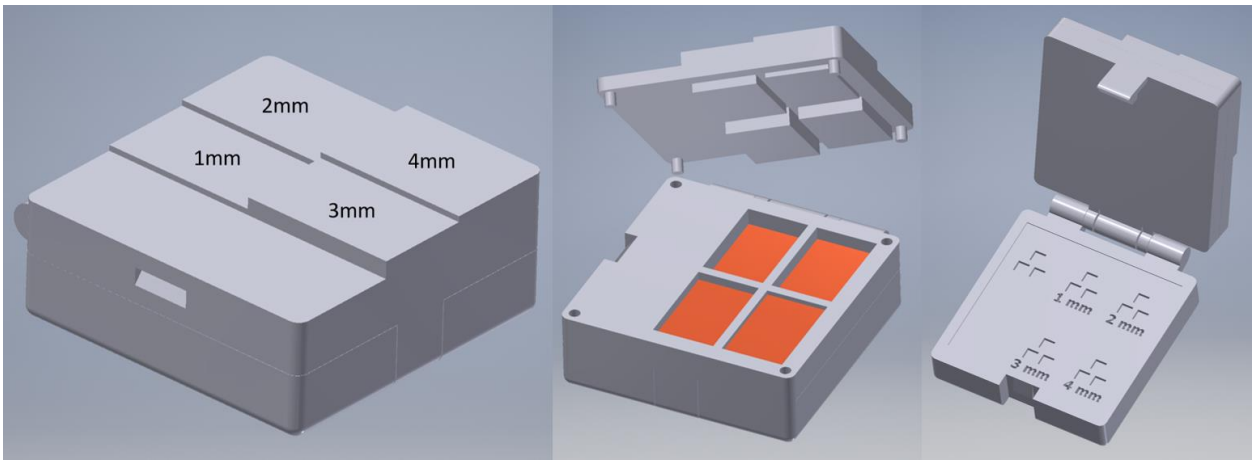

Figure 3-7 CAD model of the portable phantom developed for beam energy spectrum characterization. Each region of the phantom has the same thickness of plastic (left), above four different thickness of copper (center). Below the copper there are inserts for three TLDs in each region, including the 0 mm region (right). Film is inserted above the TLDs, with a shim in between to prevent scatter.

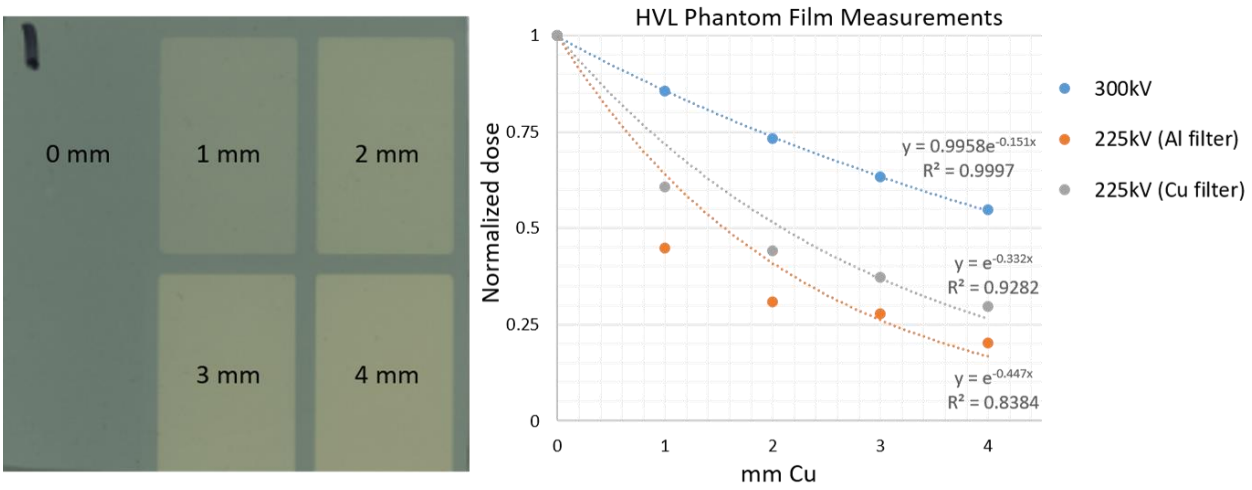

Figure 3-8 (Left) The measured film distribution for one of the half-value layer (HVL) experiments, with labels for the copper thickness above each region. (Right) Measured film doses (normalized to 1) and best-fit exponential curves for the HVL phantom irradiated with 300 kV x-rays, 225 kV x-rays with an aluminum filter, and 225 kV x-rays with a copper filter. A simple exponential relationship cannot accurately model the attenuation of polyenergetic beams, which is most evident for the 225 kV beam with aluminum filtration.

3.1.4 Conclusions

Several useful tools were developed for small animal dosimetry, including an anatomically accurate mouse phantom and a portable beam energy characterization phantom. These can be used to assess the significant inconsistencies in preclinical irradiation techniques between different institutions. The results of the dosimetric harmonization survey strongly suggest the need for increased collaboration between physicists and biologists on the design and execution of preclinical studies. Low cost, straightforward standard quality assurance protocols are needed for these systems to minimize dosimetric inaccuracies and help achieve more consistent small animal irradiation research results.

3.2 A 3D Printed, CT-Generated Monkey Phantom with Tissue and Bone Equivalent Materials

3.2.1 Introduction

Anthropomorphic phantoms mimicking realistic tissue radiographical properties are important in therapy and imaging practices. However, conventional anthropomorphic phantoms are expensive, limited in option, and lack flexibility. 3D printing is a viable technology for fabricating custom phantoms, but a process to print and assemble anatomically and radiographically realistic phantoms has not yet been demonstrated. In this study for non-human-primates, we developed and characterized a phantom from CT images using 3D printed materials that closely mimic the x-ray attenuation properties of soft tissues and bone. This straightforward and inexpensive technique could greatly increase the feasibility and value of phantom studies for a wide range of applications, such as material decomposition or proton stopping power measurements.

3.2.2 Methods

CT images were acquired for a 3 kg male rhesus monkey and segmented by Hounsfield Units (HU) into bone, lung, and soft tissues using MATLAB (The Mathworks Inc., Natick, MA). The model was then imported into Autodesk Inventor 3D CAD software for further manipulation (Autodesk, San Rafael, CA). A honeycomb structure was added within the lung volume to create the structure density necessary to mimic realistic lung CT values. This structure consisted of two overlapping hexagonal honeycombs, with side length of 4 mm and wall thickness of 0.42 mm, offset laterally by one side length. Removable

thermoluminescent dosimeter (TLD) holders were created in the chest and abdomen of the model, and a midsagittal split was made for film dosimetry. The phantom was then further segmented for printing and assembly.

All phantom segments were then printed using the Formlabs Form 2 3D printer. The Formlabs Flexible Resin was used to print all soft tissue and lung segments, and the Ceramic Resin was used to print the bone segments. Although the Ceramic Resin is intended to be fired after printing, we found that the unfired state was better suited for this application. Although the parts are quite brittle after printing, this was not a major concern because the "bones" are fully encased within the flexible "soft tissue". Also, the unfinished state actually improved the phantom assembly process by allowing the parts be sanded down where necessary for better mating. The phantom was designed to split into three segments – head/arms/chest, abdomen, and pelvis/legs – and all other permanent connections were made using superglue.

After assembly, the material properties of the phantom were assessed. CT scans were acquired of the phantom pelvis, spine, and lungs using the cone-beam CT imaging capabilities of the X-RAD SmART system. HU measurements were compared between the original monkey CT and the phantom CT for regions of interest in soft tissue, lung, and bone. A treatment plan was also created on the SmART-ATP system to deliver a dose of 8 Gy to a 10 mm target in the phantom chest in one full arc, using real tissue, lung, and bone material properties for Monte Carlo dose calculation (SmART Plan version 1.3, pegs 4 materials Tissue, Lung, Bone).

3.2.3 Results

The phantom segments were printed and assembled, with examples of both material types shown in Figure 3-9. The phantom CT scan showed good agreement with the original monkey CT in terms of average HU, as illustrated in the example ROIs in Figure 3-10. The HU values were compared for bone, tissue, and lung using the average measurements from six ROIs for each material throughout the whole phantom (1 cm diameter ROIs for tissue and lung, 5 mm diameter for bone). The average CT measurements for soft tissue differed by 53.5 HU between the real monkey and the phantom (52.5 HU and -1.0 HU, respectively), which corresponds to a difference of only 2.7% on the HU scale. The average lung measurements differed by only 1.8%, with -745.7 HU for the real monkey CT and -780.9 HU for the phantom CT. The bone had the closest average measurements, with a difference of only 1.3% (1082.3 HU for monkey, 1055.4 HU for phantom).

Figure 3-9 3D printed monkey phantom parts. The bone segments were printed out of Ceramic Resin (left) and soft tissue out of Flexible Resin (center). Inserts in the phantom abdomen and chest were designed for TLD dosimetry (right).

The calculated and measured dose distributions for this plan are shown in Figure 3-11. The measured film dose from the test treatment plan also showed good agreement with

the calculated dose distribution, with <1 Gy difference between the delivered and calculated mean target dose. This suggests that the phantom materials may serve as good surrogates for real soft tissue, lung, and bone for dosimetric testing.

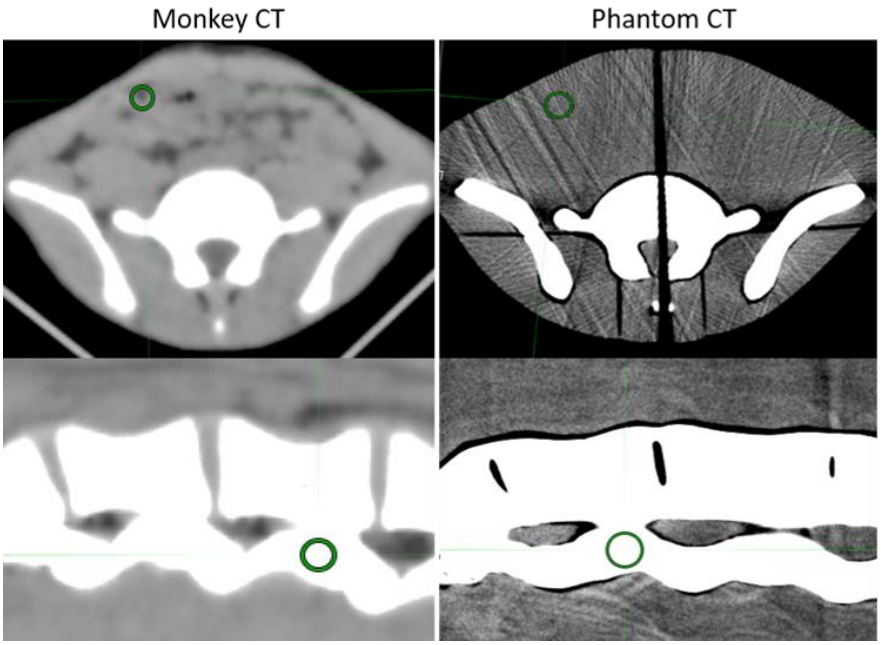

ROI values (HU)

Tissue	Monkey	Phantom
Max	83	179
Mean	**35**	**8.1**
Min	-35	-114

Bone	Monkey	Phantom
Max	1189	1107
Mean	**902**	**906**
Min	241	-444

Figure 3-10 CT images for the real monkey (left) and phantom (right) in the pelvis (upper) and spine (lower). The center slit in the phantom pelvis was designed for film insertion. Measured HU values for ROIs in the soft tissue and bone (shown in green) are given on the right. (HU: Hounsfield Units)

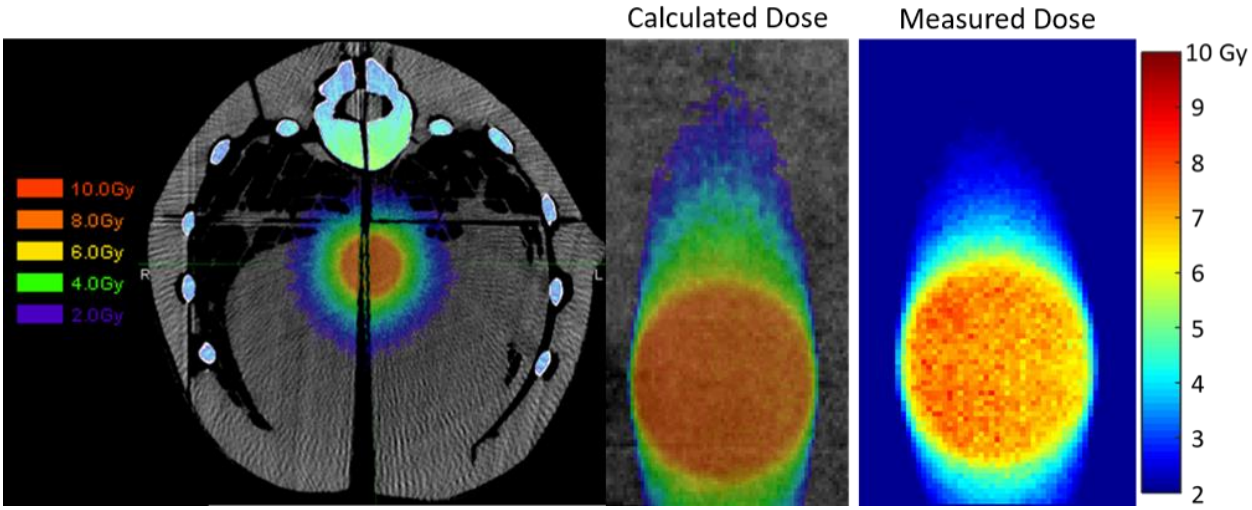

Figure 3-11 (Left) Calculated dose for the phantom test plan, with a prescription dose of 8 Gy to a 10 mm target in the phantom chest delivered in one full arc. Real tissue, lung, and bone material properties were used for dose calculation. (Right) Measured dose from film inserted into the midsagittal slit in the phantom chest, at the same plane as the calculated dose shown in the center.

3.2.4 Discussion

There were some challenges in the development of this phantom that will be improved upon in the next version. The brittleness of the unfired ceramic material was an issue for very small phantom parts, such as the ribs and vertebrae. Several of these bones broke during assembly, which was evident from the phantom CT images. This could be alleviated by slightly simplifying the bone structure, as long as this does not significantly affect the phantom dosimetry. This was also a very small monkey – only 3 kg – and would likely not be an issue with a larger primate or human phantom. The recent development of a larger version of the 3D printer used in this study would also enable the use of this technique (with the same resins) for larger phantoms.

Although further testing is necessary, preliminary measurements of the phantom show good agreement with the radiographical properties of real tissue and bone. More rigorous measurements of absolute dose will be performed using the abdominal and chest inserts shown for TLD dosimetry in order to more accurately assess the electron density of the phantom materials. A full-body scan will also be acquired with the phantom fully assembled. This will help to assess the overall fit of the bone structure within the soft tissue and identify any areas for improvement.

3.2.5 Conclusions

A CT-specific 3D printed monkey phantom was developed that closely mimics the CT values for soft tissue, lung, and bone, providing a useful preclinical research tool and establishing a method for creating more anatomically accurate custom phantoms. This straightforward and inexpensive technique could greatly increase the feasibility and value

of phantom studies for a wide range of applications, such as material decomposition or proton stopping power measurements.

4 SOC Planning System Development and Commissioning

4.1 Introduction

Since over 50% of cancer patients can benefit from radiation therapy[2,18,104], it is not surprising that this is a field of extensive research and constant technological advancement. As a result, improvements in radiotherapy techniques have greatly increased dose conformity and normal tissue sparing. Intensity modulated radiation therapy (IMRT), the current clinical gold standard, allows for the delivery of extremely precise, complex dose distributions, enabling the use of escalated doses and more novel techniques such as dose painting. However, the clinical benefits from improved dose distributions alone will likely plateau due to normal tissue tolerances and may not improve outcomes for radioresistant tumors[105]. This highly conformal treatment is possible due to advancements in image guidance and treatment planning technology, both in terms of hardware and software, but this has been driven by physics and engineering developments rather than emergent knowledge of the underlying radiobiology of tumors and normal tissue. In order to better understand which novel treatment techniques will actually translate to improved clinical outcomes, preclinical validation is required.

Small animal models, particularly mouse models, are the most widely used tool for preclinical research, providing a low-cost, versatile way to gain valuable insight into cancer growth and radiation effects[16,17]. They also provide a practical avenue for testing the safety of new drugs and combination therapies prior to human exposure. However, the translation of these results to clinical outcomes is extremely poor[18-21]. A systematic review by Hackman et al[106] showed that out of 76 highly-cited animal studies only 28 were replicated in human trials, and 14 of these had outcomes contradicting the animal trials. There was even a NCI Radiation Research Program workshop held to discuss the "Lessons Learned from Radiation Oncology Clinical Trials" in which ten well-designed, randomized clinical trials from the Radiation Therapy Oncology Group were examined, with nine of these resulting in null or negative results[107].

For these preclinical radiotherapy studies, translation is limited in large part by the irradiation techniques used[99]. Differences in fractionation and treatment setup can drastically change the response of cancer cells to radiation[108,109]. The use of much lower energy x-rays for small animals (kilovoltage vs. megavoltage) results in different dose distributions within the tissue, as well as potential differences in relative biological effectiveness[110-112]. The use of very small field sizes can also be an issue, since both the dose rate and the dose prediction accuracy decrease significantly[96]. Previously, preclinical studies used only crude irradiation techniques and protocols that did not account for these factors. These studies typically used radiation systems intended for human use, which are not nearly precise enough for the small animal scale. Very limited imaging was used, partially due to the inability of these human systems to achieve the resolution required for small animals. This lack of geometrical targeting necessitated the use of large radiation fields, therefore

delivering high doses to normal tissue as well. Most preclinical research thus far has been done with these single large fields and very crude dose calculations, in stark contrast to the highly conformal, precisely calculated (and verified) doses delivered clinically[99].

The recent development of image-guided small animal irradiators has therefore greatly expanded the potential for preclinical radiotherapy studies[98]. The two main systems are the Small Animal Radiation Research Platform (SARRP) (Xstrahl Inc., Suwanee, GA) and the X-RAD SmART (Precision X-Ray, Inc., North Branford, CT). These systems both feature cone beam CT imaging and their own dedicated treatment planning systems (Muriplan and SmART-Plan, respectively). For both irradiators, beam collimation is typically achieved using interchangeable circular or rectangular inserts ranging from 1 mm diameter to 10 x 10 cm square[97,113].

In order for preclinical studies to accurately predict patient outcomes, the techniques employed must be analogous to those used in the clinic. IMRT relies on inverse fluence map optimization combined with dose modulating hardware, both of which must be adapted for the small animal scale in order to successfully employ this technique in preclinical studies. While the two systems mentioned above offer major improvements in preclinical radiotherapy techniques, they still lack the necessary foundations for IMRT. Clinical dose modulation is achieved with a dynamic multileaf collimator (MLC), but due to its complexity, the miniaturization of the dynamic MLC for small animals is extremely difficult and has yet to be achieved. While small animal IMRT has been attempted without an MLC by raster scanning with a 1 mm cone, this technique is prohibitively slow and is subject to significant uncertainties due to improper beam modeling for small field sizes[25]. While there have been

several other attempts to develop a miniature dose modulation device, none have proven feasible for small animal IMRT. These previous efforts are described in Chapter 5, which focuses on the hardware development and commissioning.

In this study, we introduce a new method to deliver small animal IMRT using the previously described sparse orthogonal collimator (SOC)[114], with four orthogonal leaf pairs, that can be more easily miniaturized for the small animal scale, and a planning system that supports the use of this simple dose modulation device. We demonstrate the performance of this new method on hallmark IMRT cases, including highly concave dose distributions and simultaneous integrated boost plans. We also detail the measurement and incorporation of beam commissioning data into our treatment planning system and the design for the SOC hardware.

4.2 Methods

This novel small animal IMRT method is based on the idea that direct aperture optimization (DAO) can be performed using only rectangular apertures for IMRT planning. We will first introduce the optimization algorithm, then describe the beam commissioning procedure and SOC design.

4.2.1 Rectangular Aperture Optimization

For SOC-based IMRT we have formulated the Rectangular Aperture Optimization (RAO), which has been described in more detail previously[114], as

$$\underset{\boldsymbol{\alpha}}{\boldsymbol{argmin}} \quad \frac{\mathbf{1}}{\mathbf{2}}\|\boldsymbol{W}(\boldsymbol{AR\alpha} - \boldsymbol{d_0})\|_2^2 + \boldsymbol{\lambda}\|\boldsymbol{\alpha}\|_1$$

$$\boldsymbol{subject\ to} \quad \boldsymbol{\alpha} \geq \mathbf{0}.$$

Equation 4-1

The optimization variable, α, is a vector of coefficients. The matrix R is a scaling function which converts the coefficients from alpha to rectangular apertures in the fluence domain. Each column of R represents one rectangular aperture in the fluence domain, which configures a direct correspondence between each coefficient in alpha and a rectangular fluence of varied size and position. The matrix A converts the fluence to the dose domain. The desired dose, d_0, is set to the prescription dose at the PTV and zero elsewhere. The diagonal weighting matrix W controls the relative importance of the structures of interest. The definition of the norm with parameter p, for some vector x of dimension n, is $\|x\|_p = \sqrt[p]{\sum_{i=1}^{n}|x_i|^p}$. The L2-norm fidelity term is used to penalize deviations from d_0, and the L1-norm encourages the vector α to be sparse. The regularization weighting term, λ, is utilized to regulate the number of non-zero coefficients, and can be adjusted to meet the needs of a particular plan (i.e. to prioritize dosimetric quality or delivery efficiency). This problem formulation can be solved with a first-order primal-dual algorithm known as the Chambolle-Pock algorithm[115-118].

The mapping, R, represents discrete rectangles in the fluence domain, and the enumeration of every rectangle quickly becomes numerically intractable for fluence maps with a large number of beamlets. Instead, we start with an over-represented set of rectangles that have side lengths of $2^n \times 2^m$, where $n, m \in \{0,1,2, \dots, k\}$. The size of the fluence map is constrained to $2^k \times 2^k$. Since R has a limited number of rectangles it represents, a step is

added to update R with potentially important rectangles for selection. This step is performed in an alternating fashion with the optimization in Equation 4-1. The update method first takes pairwise combinations of all the apertures that have an associated non-zero coefficient from α. A new aperture is generated from the union of the aperture shapes from each pair, and is added to R if the new aperture is rectangular and is unique to the current apertures available in R. The optimization in Equation 4-1 and this update method are alternated until no more new apertures are added to R. A detailed explanation of the initial over-represented set and the update method was previously described[114].

4.2.2 RAO Evaluation

Three planning experiments were executed to validate RAO for SOC-based small animal IMRT. The aim of the first experiment was to evaluate the ability to create highly concave distributions and compare the quality of plans delivered with the SOC versus a hypothetical miniature MLC. A U-shaped target was first created on microCT images of a mouse brain (Mouse U). Two plans were created, one with a hypothetical conventional MLC having 0.5 mm resolution and the other with the SOC. The MLC plan was created by first performing a beamlet-based fluence map optimization, regularized by anisotropic total variation, as described in a previous publication[119]. The resulting fluence maps were then segmented such that the number of deliverable apertures matched that of the SOC plan. The U-shaped target was treated to 10 Gy. A SOC plan was then created for a more complex target volume with two overlapping U and C-shaped targets (Mouse UC). For the Mouse UC case, the non-overlapping volume was treated to 10 Gy, and the overlapping volume was treated to 12.5 Gy, a 25% dose boost.

In the second experiment, a 3D printed mouse phantom modeled from mouse CT data was used to demonstrate a realistic application for the SOC. One preclinical research area in which the SOC could be beneficial is investigating the role of radiation-induced damage-associated molecular patterns (DAMPs) in cancer[120] and ways to manipulate these immune responses in specific organs such as the liver[121]. In order to properly characterize these responses, it is necessary to deliver a conformal radiation dose to the liver while sparing the surrounding normal tissue and other organs. To simulate such an experiment, a mouse CT scan was acquired using contrast for better delineation of the liver and kidneys. Contours were drawn for these two structures and transferred to analogous positions on the body contour of the mouse phantom CT. The planning objective was to deliver a dose of 10 Gy to the whole liver while sparing the dose to the kidneys and surrounding normal tissue.

The third experiment was designed to evaluate the level of 2D dose complexity achievable with the SOC and create a plan well-suited for evaluating the commissioning steps described in the following section. For this plan, an image of Audrey Hepburn was downsampled and simplified to three dose prescription levels of 2, 4, and 6 Gy. This target dose pattern lends itself to a wide range of aperture sizes, making it ideal for evaluating field size-specific effects on the dose distribution.

For each of the mouse plans, the dose was calculated for 180 coplanar beams with 2° separation using a convolution/superposition algorithm with a 225 kV polyenergetic kernel tuned to match the PDD of the SmART system for a 2.5 cm (Mouse U and UC) or 1 mm (Mouse Liver and Audrey) field size. The justification and measurement of this 1 mm field size energy spectrum is detailed in a later section. The voxel resolution was 0.5 mm^3 for the Mouse U and

UC plans and 0.1 mm^3 for the Mouse Liver and Audrey plans. The 4π beam orientation optimization method, which has been previously published extensively[9,10,12-15,26-28,85,122], was then used to find optimal beam angles for each plan. This optimization is based on a greedy column generation approach which iteratively selects beams from a candidate pool. Since the Mouse U and UC plans aimed to evaluate the highest achievable SOC plan quality, 20 optimal beams were selected and a beamlet size (and minimum aperture size) of 0.5 mm^2 was used. The Mouse Liver case was planned more conservatively, with a more realistically deliverable beam count of 5 and a minimum aperture size of 1 mm^2. The Audrey plan was also optimized for a 1 mm^2 beamlet size. RAO was then applied for each plan, with a shell structure added around the PTV for the mouse plans to minimize dose spillage. The mouse plan doses were scaled to deliver the prescription dose to 95% of the target volume.

As dosimetric endpoints for evaluation, R_{50} and PTV homogeneity $\left(\frac{D95}{D5}\right)$ were assessed. R_{50} is a measure of high dose spillage, defined as the ratio between the 50% isodose volume and the PTV volume. The van't Riet conformation number (CN) was also assessed[123]. CN is defined as $CN = \frac{TV_{RI}}{TV} \times \frac{TV_{RI}}{V_{RI}}$, where TV_{RI} is the target volume covered by the prescription dose, TV is the target volume, and V_{RI} is the prescription dose volume.

4.2.3 Beam Commissioning Measurements

The optimization method described above assumes the same output, energy spectrum, and penumbra for all aperture sizes and locations, and does not account for any system-specific characteristics or imperfections. Therefore, a series of beam commissioning measurements, detailed in Table 4-1, were performed on our X-RAD SmART system in order

to improve the dosimetric accuracy of RAO IMRT plans delivered on this system. All measurements were done at an energy of 225 kV and source surface distance (SSD) of 30.5 cm with 0.32 mm added copper filtration. Film measurements were performed with Gafchromic EBT3 film (lot #10161801) (Ashland Inc., Covington, KY) and scanned on an Epson 10000XL scanner with a resolution of 96 dpi in 48-bit RGB (red, green, and blue). Film doses were analyzed with Ashland's FilmQA Pro software using a red channel calibration curve created from the same film lot according to the manufacturer-recommended protocol[124]. The 40 x 40 mm square stationary collimator for the SmART system was used for the larger field measurements. All field sizes <40 mm were created using a prototype SOC system. Briefly, the SOC design consists of four pairs of orthogonal, double-focused tungsten leaves driven by Arduino-controlled stepper motors with rotary encoders for leaf position verification. The SOC system is mounted onto the 40 x 40 mm collimator of the SmART. The complete design, fabrication, installation, and commissioning of the SOC is detailed in Chapter 5.

Table 4-1 SmART system beam commissioning measurement parameters

Measurement	Equipment	Square field sizes (mm)	Depth	Calculation details
Absolute output	Ionization chamber, electrometer	40	In air	AAPM Task Group 61 protocol[125] (average of 3 measurements)
Output factor	EBT3 film, solid water sheets	26, 20, 15, 10, 5, 2.5, 1	2 mm	$\frac{mean\ dose(field\ size\ x)}{mean\ dose\ (26\ mm\ field)}$ (average of 4 measurements)
Off-axis factors		5, 2.5, 1 (1.5 mm apart over entire SOC field)	2 mm	$\frac{mean\ dose(\ location\ x)}{mean\ dose\ (center)}$
Percent depth dose		40, 20, 10, 5, 1	20 depths, 0-10 cm	$\frac{mean\ dose(\ depth\ x)}{max(all\ mean\ depth\ doses)}$
Flatness		40	2mm 2cm 4cm	Percent variation from mean dose across central 80% of FWHM (average of 5 line profiles)

The measured off-axis factors were used to create off-axis "maps" for field sizes of 5, 2.5, and 1 mm. These maps were then interpolated to estimate the output at any point within the full SOC field. Simplified maps were also created to compare the off-axis factors for different field sizes by averaging the measurements within nine equal regions of the SOC field. Preliminary measurements showed no significant difference in off-axis output for fields >5 mm.

The measured PDD data was used to generate an estimated energy spectrum for each field size, with mean and maximum allowed PDD deviations of <2% and <5%, respectively. These spectra were obtained by first using the dose calculation method previously described with a virtual water phantom to generate 40 different PDD curves (spanning the range of the

measured curves) for beams with slightly different attenuation properties. The convex optimization software CVX (CVX Research, Inc., Austin, TX) was then used to find the optimal weighting of each curve to best match the measured PDD.

Any average field flatness variations of ≤5% from the mean dose were not incorporated into the treatment planning system at this stage of commissioning. However, these measurements are necessary for assessing the overall system error.

4.2.4 Plan Post-Processing

This data was then integrated into the treatment planning process. Originally, the dose was calculated using a single general energy spectrum, previously tuned for a 20 x 20 mm field on the SmART, and the plan was optimized using this dose matrix. However, this optimized plan may include a wide range of aperture sizes, and the calculated dose will theoretically only be accurate for 20 x 20 mm apertures.

Therefore, instead of performing the initial dose calculation with a single energy spectrum, this step was updated to calculate five different dose matrices using the estimated energy spectra for 1, 3, 5, 10, and 20 mm square field sizes. After optimization, the final apertures can then be separated by closest equivalent square field size, multiplied by the appropriate dose matrix and optimized weighting value (α), and summed together to get a potentially more accurate, aperture size specific dose distribution. Since the plan quality is typically degraded to some extent after dose recalculation, the aperture weightings are then re-optimized to match the original optimized dose as closely as possible.

Since five different initial dose matrices are calculated now, the remaining question is which should be used for the initial optimization. This was explored by performing the rectangular aperture optimization for the same plan using the dose matrices for each of the five energy spectra. The difference between each optimized dose and the recalculated field size specific dose was then analyzed. The Audrey plan was ideal for this analysis because of its wide range of aperture sizes (a preliminary optimization selected apertures ranging from 1 to 20 mm equivalent squares).

The weighting for each aperture is then converted to a dwell time based on the measured absolute output and scaled by output factor using the equivalent square field size. In addition to output factor scaling, apertures ≤5 mm are matched by equivalent square size to the closest off-axis factor map and scaled according to their location within the SOC field.

Once the final apertures and dwell times have been calculated, the plan is prepared for delivery with the SOC hardware, described in the following section. The basic SOC design enables apertures in diagonal quadrants to be delivered simultaneously, greatly improving the plan delivery efficiency. Therefore the apertures are then categorized by quadrant, and apertures in diagonal quadrants are combined to be delivered in parallel. The apertures are also sorted by dwell time prior to combination so that the longest times are paired together, further increasing delivery efficiency.

4.3 Results

4.3.1 RAO Plan Analysis

In the first experiment, the average number of deliverable apertures per beam was 11.5 and 10.5 for the Mouse U and UC cases, respectively. Figure 4-1 shows the resulting dose distributions for highly concave RAO IMRT plans inside the mouse brain. Both hypothetical MLC and SOC plans achieved conformal dose distributions, but the SOC plans had higher homogeneity within the target volume. The poorer performance of the MLC is due in part to the extra segmentation step from the fluence map to deliverable apertures, which is avoided with the DAO method used for the SOC plans. The SOC was also able to create the more complex UC target while sparing the normal brain. The PTV homogeneity, R_{50}, and CN for the Mouse U and UC cases are given in Table 4-2. For the Mouse U case, the SOC plans were superior to the MLC plans in all categories. The Mouse UC SOC plan achieved acceptable conformity and homogeneity while minimizing the high dose spillage.

In the second experiment, RAO achieved a highly conformal dose to the mouse liver while sparing the dose to the kidneys, as shown in the DVH and dose wash in Figure 4-2, demonstrating a realistic application for the SOC. The plan achieved relatively high target homogeneity and conformity with low dose spillage, as demonstrated by the evaluation metrics given in Table 4-2. Most importantly, this high quality dose distribution was achieved using realistic delivery parameters of five beams and 1 x 1 mm minimum aperture size.

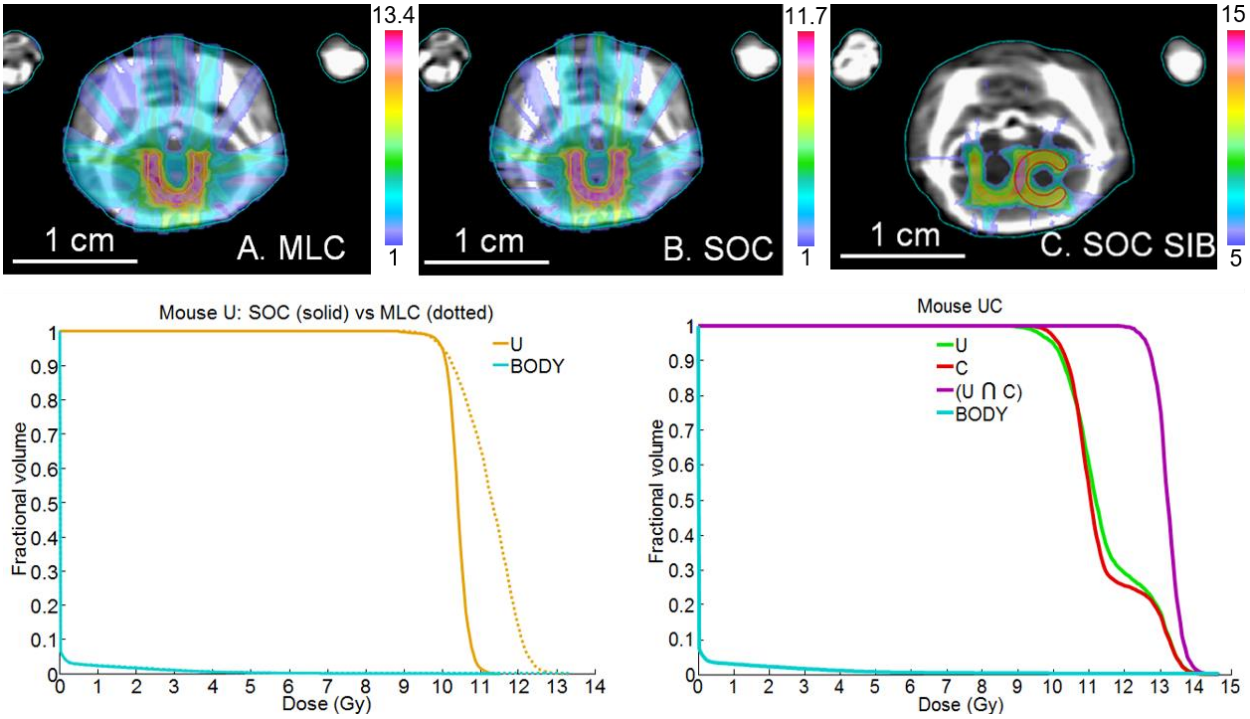

Figure 4-1 (Upper) Calculated concave dose distribution (with colorbar units in Gy) in the mouse brain delivered with a hypothetical MLC (A) and the SOC (B). Simultaneous integrated boost SOC plan (C) with a 125% dose boost to the overlapping target region. (Lower) Dose volume histogram comparisons for plans in (A-C). The SOC plans show a more homogeneous dose with less high dose spillage using the same number of segments.

Table 4-2 Dose evaluation metrics for the mouse test cases (R50: 50% dose spillage; CN: Conformation Number)

Plan	Target	Homogeneity	R_{50}	CN
Mouse U (SOC)	U	0.922	4.459	0.753
Mouse U (MLC)	U	0.815	4.818	0.626
Mouse UC (SOC)	U - C	0.888	3.862	0.713
	C - U	0.896		
	U ∩ C	0.914	N/A[a]	0.711
Mouse Liver (SOC)	Liver	0.895	2.204	0.856

[a]No R_{50} calculation for the U ∩ C volume was made since the dose to the non-overlapping volume would be included in the calculation.

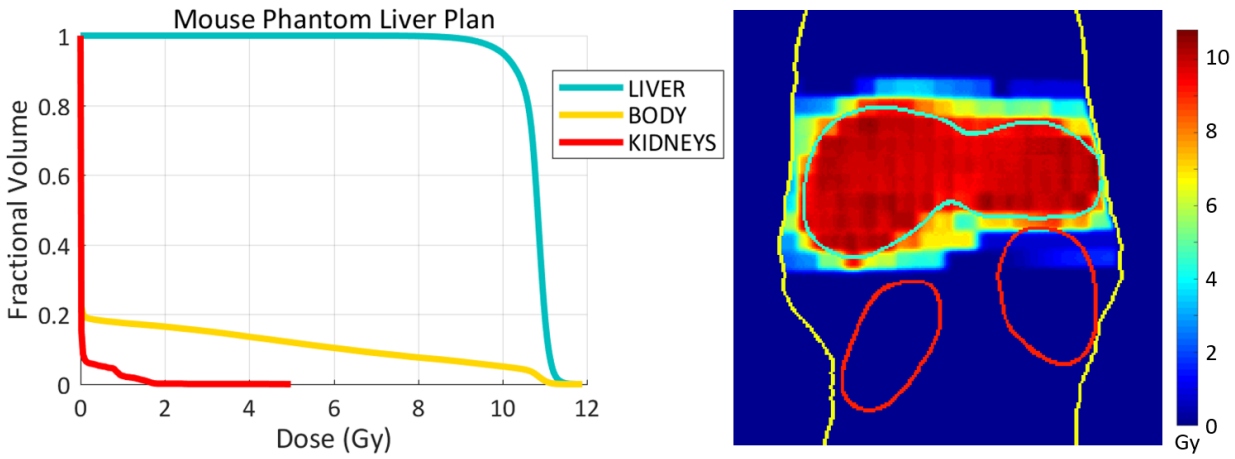

Figure 4-2 Dose volume histograms (left) and dose wash (right) for the mouse phantom whole liver irradiation plan, optimized with RAO. In both images, the liver (target) is shown in teal, body in yellow, and kidneys in red.

The resulting dose distribution for the Audrey RAO IMRT plan is shown in Figure 4-3. This complex target image, with four dose levels (including 0 Gy) and 1 mm resolution, was closely replicated with RAO using a total of 551 apertures with a mean size of 2.4 x 2.4 mm. Due to the high number of small fields, this corresponds to an estimated delivery time of approximately 18 minutes (after applying the output and off-axis factors presented in the following section). While this would be impractically high for a single beam of a mouse SOC plan, it is certainly feasible for delivery as a proof-of-concept.

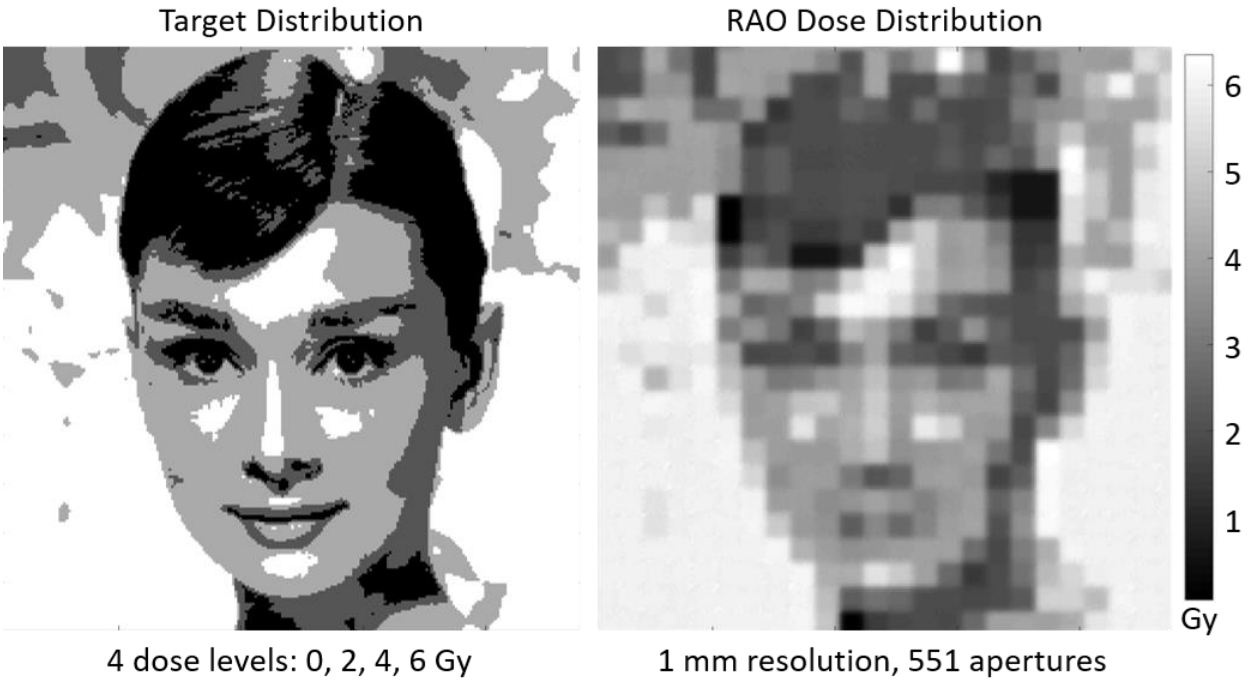

Figure 4-3 (Left) Target image for the Audrey Hepburn plan, with 4 dose levels of 0, 2, 4, and 6 Gy. (Right) Optimized dose distribution from RAO with 1 mm beamlet and minimum aperture size. The optimized plan used 551 apertures with an average size of 2.4 mm.

4.3.2 Beam Commissioning

The absolute output of the SmART was 0.461 cGy/mAs, and the measured output factors are shown in Figure 4-4. A logarithmic curve was fit to the average measurements for field sizes 2.5 to 25 mm with an R^2 value of 0.9916. Since the output dropped significantly for 1 mm fields and a simple curve could not closely fit all data points, a separate logarithmic equation was used for fields 1 to 2.5 mm. These relationships are used to scale each aperture by output factor based on its equivalent square field size. The smallest field size for which the output could be reliably measured with film was 1 mm, for which the output factor was 0.747 ± 0.025. Therefore, although the orthogonal SOC design is theoretically capable of achieving smaller aperture sizes, for now the minimum beamlet size for SOC-based IMRT is limited to 1 mm. This inconsistency in submillimeter field dosimetry is likely the result of

slight leaf positioning errors, which have a large effect on small field sizes due to occlusion of the ~3 mm diameter focal spot. There may also be error resulting from an inhomogeneous focal spot distribution, which has been observed in previous studies[126] and will be discussed in a later section.

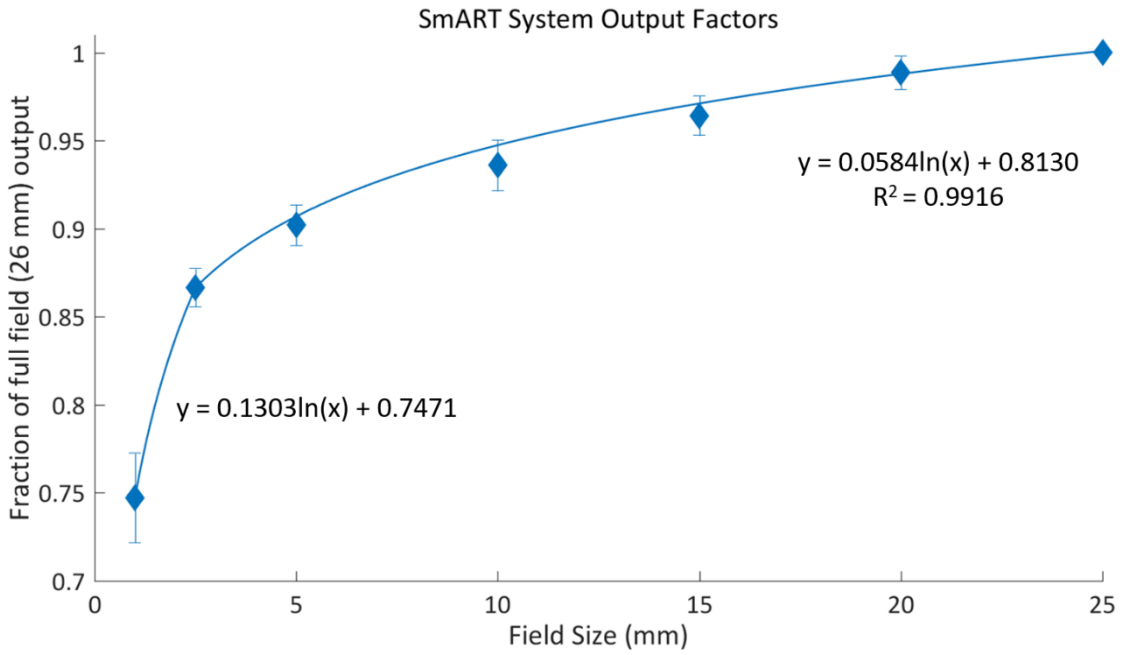

Figure 4-4 Measured output factors (average and standard deviation shown for 4 measurements) for the SmART system, calculated as a fraction of the full 26 mm SOC field.

Simplified off-axis factor measurements for field sizes 5, 2.5, and 1 mm are given in Table 4-3, averaged over nine SOC field regions for comparison, and the calculation process is illustrated in Figure 4-5 for 2.5 mm fields. The highest output was measured in the center of the SOC field for all three field sizes and was therefore the reference point for all other region measurements. The minimum and maximum (excluding the center) output factors were measured in the same SOC field regions for the 2.5 and 1 mm fields, but differed for the 5 mm field, although the effect is minimal for this larger field size. The full interpolated maps, such as the one shown in Figure 4-5, right, are used for the final off-axis aperture scaling.

Table 4-3 Simplified off-axis factor measurements for 1, 2.5, and 5 mm square SOC fields on the SmART system, averaged over nine equal regions for comparison

Off-Axis Factors (shown according to SOC field location)								
1 mm			2.5 mm			5 mm		
.70	.70	.65[b]	.94	.96	.91[b]	.97	.99	.99
.75	1.00	.70	.96	1.00	.93	.98	1.00	1.00[a]
.70	.80[a]	.65[b]	.93	.97[a]	.91[b]	.96[b]	.97	.97

[a]Maximum off-axis factor (excluding the center region)

[b]Minimum off-axis factor

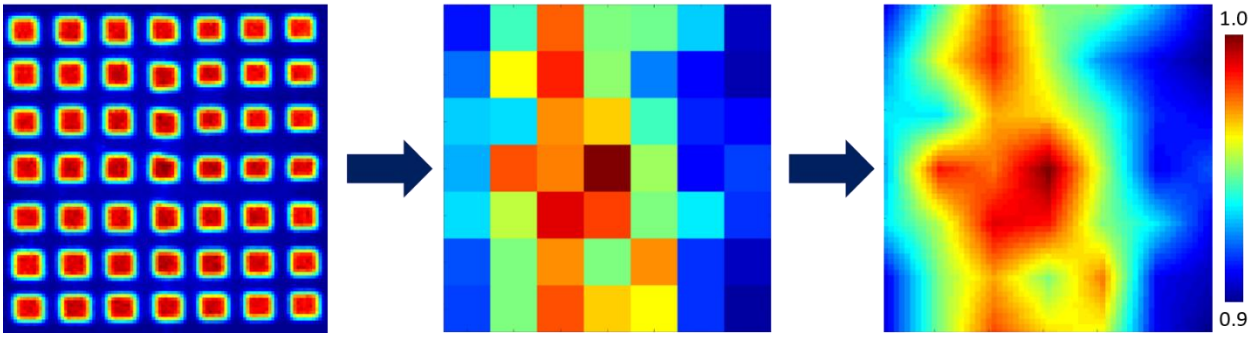

Figure 4-5 The 2.5 mm field off-axis dose film map (left), mean dose measurement map (center), and final interpolated off-axis factor map (right).

The measured PDD curves for square field sizes 1 to 40 mm are plotted in Figure 4-6, along with the matched energy spectra curves. Each spectrum is a weighted combination of two to three of the 40 candidate beams. The average maximum and mean differences between the measured and matched PDD curves were 4.47 ± 0.30% and 1.71 ± 0.18%, respectively.

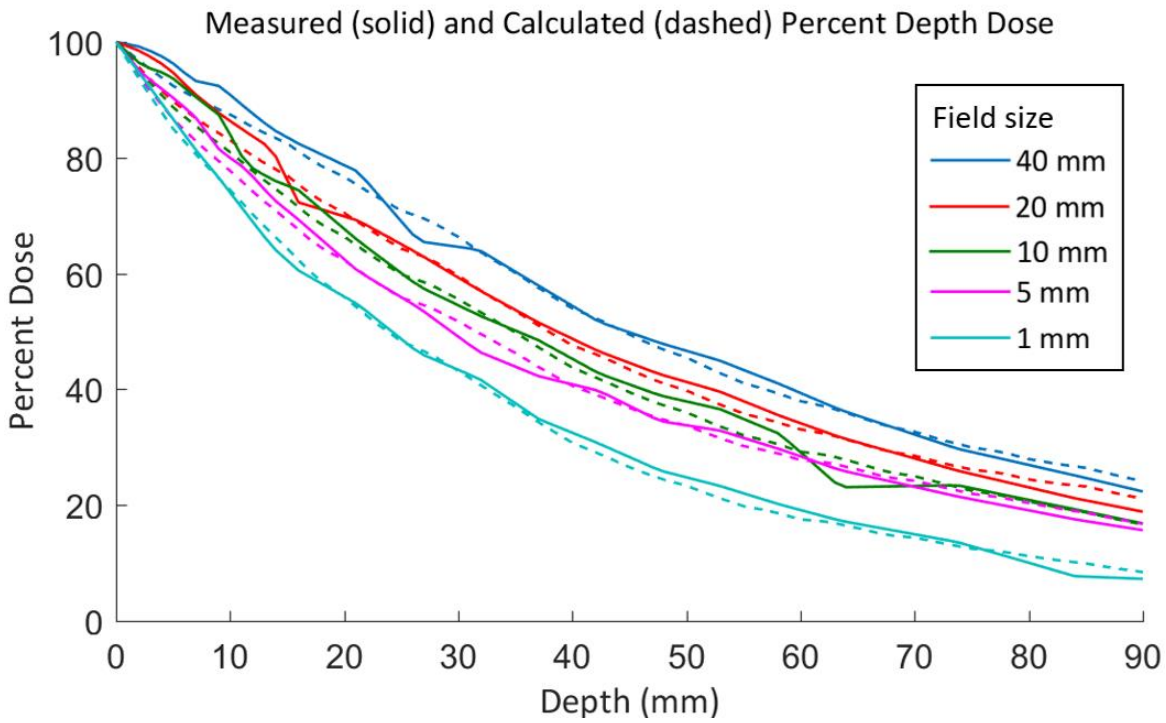

Figure 4-6 Measured percent depth dose curves for different field sizes on the SmART (solid lines) and for the energy spectra optimized to match each measured curve (dashed lines).

The flatness measurements for a 40 mm square field at depths of 2 mm, 2 cm, and 4 cm are given in Table 4-4. Since all mean dose variations were below 5%, as well as the maximum variations at 2 mm depth, field flatness was not factored into our treatment planning process at this point. However, there were some maximum variations of over 5% at 2 cm and 4 cm depths. Since this may lead to non-negligible errors in our dose prediction, the field flatness will be further characterized and incorporated at the next level of planning system commissioning.

Table 4-4 Field flatness for a 40 mm square field on the SmART system

Field Flatness (% variation, 40 mm field)						
	2 mm depth		**2 cm depth**		**4 cm depth**	
Direction	*Max*	*Mean*	*Max*	*Mean*	*Max*	*Mean*
X	4.96	1.62	5.45	1.72	8.20	2.57
Y	4.52	1.46	4.99	1.75	6.98	1.92

4.3.3 Dose Recalculation

For the Audrey plan dose recalculation assessment, the five plans optimized with each dose matrix (calculated for energy spectra tuned to 1, 3, 5, 10, and 20 mm field sizes) all selected at least two apertures of each closest equivalent square field size. The most common aperture size selected for each plan was 1 mm (66.8 ± 1.0%). This decreased with increasing field size, with a least common aperture size of 20 mm (0.6 ± 0.1%). The difference between the optimized and recalculated dose for each plan is shown in Figure 4-7 (upper), and the mean and maximum dose deviations, as well as the complete aperture size breakdown, are given in Table 4-5.

Table 4-5 Error comparison for plans optimized with different dose calculation spectra

Optimization Dose Matrix (energy spectrum field size, mm)	**Optimized Dose – Recalculated Dose (absolute voxelwise comparison, % of maximum dose)**	
	Mean	*Maximum*
1	1.2	11.0
3	3.0	16.0
5	3.4	14.7
10	3.1	9.7
20	3.2	9.7

The spatial distribution of the dose deviations is intuitive, with most of the error arising from the largest apertures in the 1 mm optimization and from the smallest apertures in the 20 mm optimization, while the 5 mm optimization shows a mix of both. The 1 mm optimized plan had a mean dose deviation of only 1.2% of the maximum dose, compared to ≥3% for the other plans, likely because the majority of apertures were closest to this field size. The 10 and 20 mm optimized plans had the lowest maximum dose deviation of 9.7%, despite these field sizes making up only ~2.2% and ~0.6% of the total apertures, respectively. The 5 mm optimized plan had the highest mean deviation (3.4%) and the 3 mm plan had the highest maximum deviation (16.0%), which suggests that "compromising" with one of the middle aperture sizes may not be a good strategy. Given the computational power available, it is feasible to instead perform this initial optimization in parallel for all field sizes, perform the aperture-specific dose recalculation for each, and select (either manually or automatically) the dose distribution that best meets the planning objectives.

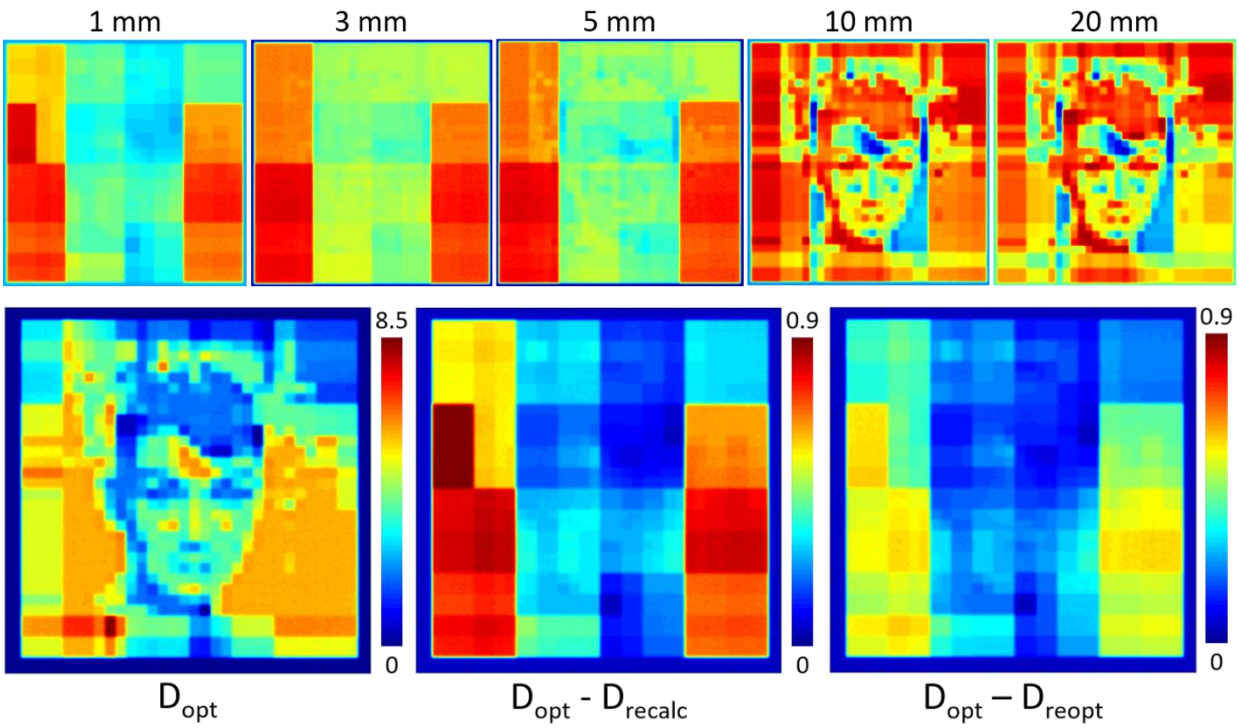

Figure 4-7 (Upper) Difference from the recalculated (field size-specific) dose for each optimization spectrum. (Lower) Dose optimized with the 1 mm field calculation spectrum (left), difference between the optimized dose and the recalculated dose, with a mean of 1.2% and maximum of 11.0% of the maximum plan dose (middle), difference between the optimized dose and the dose after reoptimization of the aperture weightings, with a mean of 1.2% and a maximum of 7.3% of the maximum plan dose (right). All dose distributions are shown at the target depth of 2 mm. (D_{opt}: original optimized dose; D_{recalc}: optimized dose recalculated based on aperture size; D_{reopt}: dose after reoptimization of aperture weightings)

For the same test plan, the maximum difference between the original optimized dose (for 1 mm field size) and the recalculated dose was reduced from 11.0% to 7.3% of the maximum dose after reoptimization of the aperture weightings. The mean difference was maintained at 1.2%. These differences in dose distribution are shown in Figure 4-7 (lower).

4.4 Discussion

The gap between human radiotherapy and preclinical animal studies has widened with the utilization of IMRT and other more sophisticated radiotherapy techniques including

4π radiotherapy. The increasing discrepancy in dose conformality can adversely impact the ability to translate animal studies to effective human trials. Due to a difference in size of one to two orders of magnitude, direct translation of the MLC used in human radiation therapy has met insurmountable engineering difficulties. In this study, we describe an alternative approach using a sparse orthogonal collimator for small animal IMRT. With the RAO SOC test cases, we demonstrated the ability to create highly conformal plans with concave and complex targets.

It is evident from our beam commissioning measurements that the accurate characterization of small, off-axis fields is currently the limiting factor in terms of the minimum SOC aperture size. However, some of the main sources of error with these measurements are due to fundamental limitations of the SmART system itself and the temporary gantry mounting of the prototype SOC (described in Chapter 5), rather than the SOC design. Despite our best effort, there are some challenges mounting the SOC onto the SmART system gantry, causing slight misalignment with each installation. Even with leaf position re-calibration, the misalignment can introduce detectable residual error for fields smaller than the 3 mm diameter focal spot. While the SmART system does have a smaller focal spot option, the low output would lead to prohibitively long treatment times.

Even with perfect SOC alignment, the dosimetry of submillimeter field sizes would likely still be a challenge. Tryggestad et al performed a pinhole experiment with a similar source (225 kVp, 3 mm large focal spot) on the SARRP and found that the focal spot had a highly inhomogeneous intensity, significantly affecting the dose distribution from a 0.5 mm aperture[126]. These effects were much less significant for 1 mm fields, resulting in only slight

asymmetry. In order to reduce the minimum SOC aperture size below 1 mm, we would need to fully characterize the large focal spot fluence distribution and incorporate this into our dose calculation engine for more accurate small field dose predictions.

Despite these uncertainties, the SOC is better suited for small animal radiotherapy than the MLC. In addition to the simplified hardware design, the SOC has advantages in terms of the optimization algorithm. While the MLC can conform to more arbitrary shapes, the SOC is seemingly limited in the complexity of apertures. However, this limitation is advantageous in solving the direct aperture optimization problem using the rectangular basis, since the dose degradation during the fluence map to MLC aperture conversion is avoided. This results in high quality plans and in some cases, such as the U target plan, more homogeneous and conformal PTV doses. Our analytical rectangular direct aperture optimization method is distinctly different from previous "jaws-only" optimization approaches[127,128] using a stochastic simulated annealing method, which is slow and cannot search all available apertures.

Also, unlike with human treatments, trained dosimetrists and medical physicists are unaffordable in preclinical studies. Therefore, any small animal treatment planning system must be highly automated in order to be a realistic and desirable alternative to current methods. Although the target and avoidance structures, if any, would still need to be contoured, the rest of the proposed planning system requires very limited user input. With the use of automated beam selection, followed by rectangular aperture optimization and system-specific plan post-processing, high quality treatment plans can be created for SOC delivery without any special training or lengthy planning process.

4.5 Conclusions

By using advanced optimization techniques, complex IMRT plans were achieved using a simple dose modulation device. Beam commissioning data was incorporated into the treatment planning process to more accurately predict the resulting dose distribution. This platform substantially reduces the gap in treatment plan quality between clinical and preclinical radiotherapy, potentially increasing the value and flexibility of small animal studies.

5 SOC HARDWARE DEVELOPMENT AND COMMISSIONING

5.1 Introduction

As described in Chapter 4, one of the main limitations in the clinical translation of small animal radiotherapy studies is the major discrepancy in irradiation techniques[99]. To deliver analogous treatment to small animals, the development of a small animal IMRT platform is necessary. Such a platform requires two developments, the first being a planning approach based on inverse fluence map optimization, such as the Rectangular Aperture Optimization (RAO) based treatment planning system detailed in Chapter 4. The second is a dose modulation device suitable for the small animal scale.

The majority of small animal radiotherapy systems have been limited to stationary collimators, with a few exceptions. At Stanford University, a variable hexagonal aperture collimator was developed to achieve beam diameters up to 102 mm[22]. The University of Western Ontario developed motorized orthogonal jaws for their micro-CT/RT system, with characterization focused on 2 to 30 mm field sizes[23]. A binary micro-MLC (bmMLC) has also been developed by the University of Wisconsin-Madison[24]. Unlike the dynamic MLC with a continuous range of leaf positions, the bmMLC leaves are either open or closed, similar to the

collimator design for the Tomotherapy system[129]. However, this system is limited by excessive leakage (5.4% interleaf leakage, 1.7% average transmission) and long delivery times. While all of these devices enable more conformal treatment delivery, none are optimal for small animal IMRT.

More recently, a Motorized Variable Collimator (MVC) has become commercially available for the Small Animal Radiation Research Platform (SARRP) (Xstrahl Inc., Suwanee, GA), which uses two sets of focused, orthogonal tungsten jaws. Very preliminary efforts using the MVC for jaws-only small animal IMRT have been presented from the Institute of Cancer Research, London[130]. This approach generates IMRT fluence maps first and then converts them to rectangular apertures. This process is known to degrade the dosimetry, which worsens when the shape and number of apertures is limited. Furthermore, the MVC is fundamentally limited by its inability to create asymmetric apertures, requiring the use of couch movements to deliver off-axis fields. This excessive couch translation introduces significant potential for motion errors and increased delivery times, which are already lengthy because only one aperture can be delivered at a time.

Clinical dose modulation devices have been developed to exploit the unique advantages of bi-directional collimation while also providing the flexibility of an MLC. In studies on the commissioning of a dual-layer micro MLC for clinical radiotherapy systems, the additional layer of leaves significantly reduced the leaf-end transmission[131,132], which can be as high as 30% for a typical single-layer MLC[133]. The ability to collimate fields in both directions with the second orthogonal layer MLC layer also enables higher resolution than a

standard single-layer MLC, for which the resolution perpendicular to leaf motion is determined by the physical leaf width.

The Sparse Orthogonal Collimator (SOC), with four pairs of double-focused orthogonal leaves, maintains the simplicity of a jaws-only system while achieving flexibility closer to that of a dual-layer MLC, as well as increased delivery efficiency. This makes the SOC ideal for small animal dose modulation when used in combination with the RAO-based treatment planning system detailed in Chapter 4. In this chapter, the complete design and fabrication of the SOC hardware is presented, as well as the software development and full system commissioning and testing.

5.2 Methods

5.2.1 SOC Design

In order to deliver rectangular apertures, theoretically only two pairs of orthogonal leaves are required (essentially "jaws-only" IMRT). However, increasing the number of leaves increases the delivery efficiency, as it enables the dose to certain regions of the fluence map to be delivered in parallel, as previously mentioned. Increasing this to more than two leaves per bank greatly increases the complexity of the system while providing only minor improvements in efficiency, as previously shown[114]. Therefore the preclinical SOC designed in this study features two leaves per bank.

This orthogonal system design is ideal for a miniaturized small animal system as the deliverable aperture resolution is dependent on the leaf motion step size rather than the leaf width. However, the simplicity of the SOC design requires that the two sets of orthogonal

collimator leaves have slightly different source-to-leaf distances, which could cause the delivered fluence rectangles to have an asymmetric penumbra. This is mitigated with a double-focused leaf design, where the leaves have curved geometry and move along an arc that matches the beam divergence. While the general SOC geometry is feasible for use with a variety of irradiators, the design detailed in this study was tailored to the X-RAD SmART small animal image-guided irradiation system at UCLA. Computer-aided design (CAD) models for all SOC system components were created using Autodesk Inventor (Autodesk, Inc., San Rafael, CA).

Designs for the double-focused SOC leaves are shown in Figure 5-1. The radii of curvature were chosen for a source-to-leaf distance (to the top of the upper leaf) of 14.94 cm, with 3 mm thick leaves and a gap of 0.5 mm between upper and lower leaf sets to avoid collision. The leaves are 3 mm thick to achieve >99.5% beam attenuation based on preliminary transmission measurements with the same tungsten alloy (95% W, 3.5% Ni, 1.5% Fe; density of 18 g/cm^3). The depth of the tongue and groove is 0.2 mm in order to keep the leaves interlocked without significantly affecting the penumbra. The heights of the tongue and groove are 1.4 and 1.6 mm, respectively. These dimensions are ideal firstly because a 0.1 mm tolerance is necessary on each side of the tongue for smooth movement. Also, this means that both leaves have a total of 1.4 mm of tungsten extending the 0.2 mm of the tongue and groove joint and will therefore have the same x-ray attenuation, preventing uneven SOC aperture penumbras. Each leaf also has a 1.35 mm thick, 1.45 mm wide outer tongue that slides along rails in the SOC housing for added leaf stability. These tongues are along the top edge for upper leaves and bottom edge for lower leaves. Each upper and lower leaf pair also has a mirroring pair for the opposing leaf bank, with the leaf connector tab on

the opposite end, enabling inter-digitation of opposing tongue and groove joints. Therefore, the geometry for each of the eight leaves is unique.

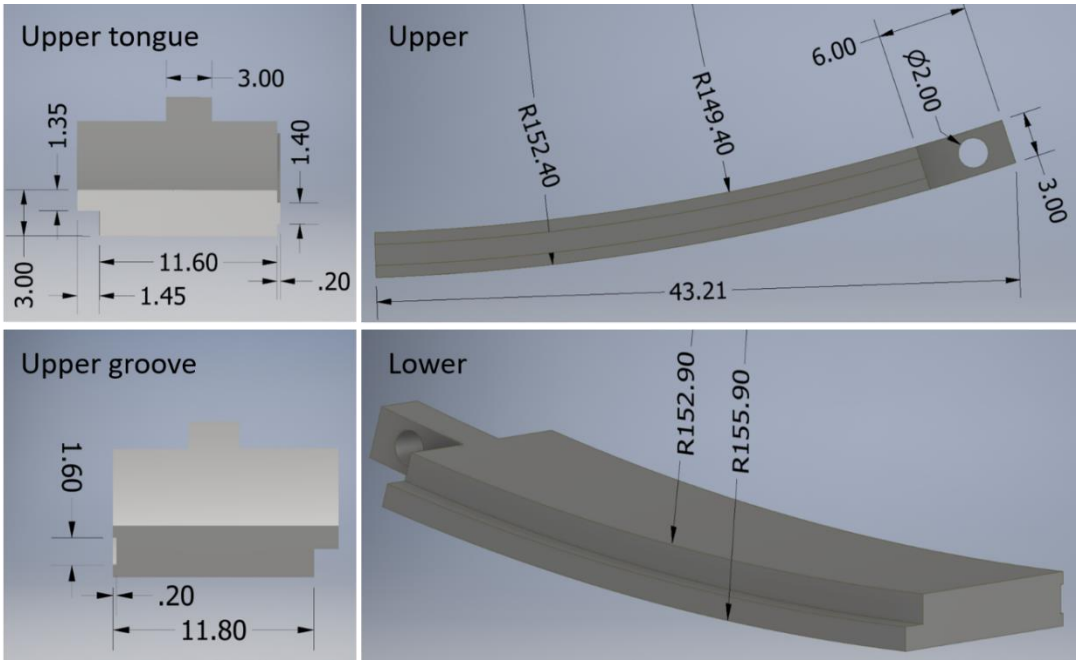

Figure 5-1 Leaf designs for the SOC, with dimensions shown in millimeters. Upper and lower leaf sets feature different radii of curvature and different geometry for the outer stabilizing tongues (along the top/bottom for upper/lower leaves, respectively). Each tongue and groove pair also has a mirroring pair with the tab on the opposite end.

The CAD model for the rest of the SOC system is shown in Figure 5-2. A custom rod with clevis and pin attaches the tab on each leaf to a stepper motor, which screws into a support structure in the housing. The outer leaf tongues slide along upper or lower rail systems for stability. A column of small (4 mm) tungsten cubes at the intersection of each orthogonal leaf bank shields the outside corners of the primary collimator field (4 x 4 cm at isocenter), which is larger than the SOC field (2.6 x 2.6 cm). The top of the housing features a detachable cable guide for the motor wires, which attach to a common socket at the back of the SOC. The housing top also has an adapter for mounting the system to the primary SmART collimator. The adapter is designed for a very tight fit onto the collimator (which

unfortunately has no other features to use for mechanical attachment) with a screw clamp for extra support. Figure 5-3 shows the whole SOC system mounted onto the SmART gantry.

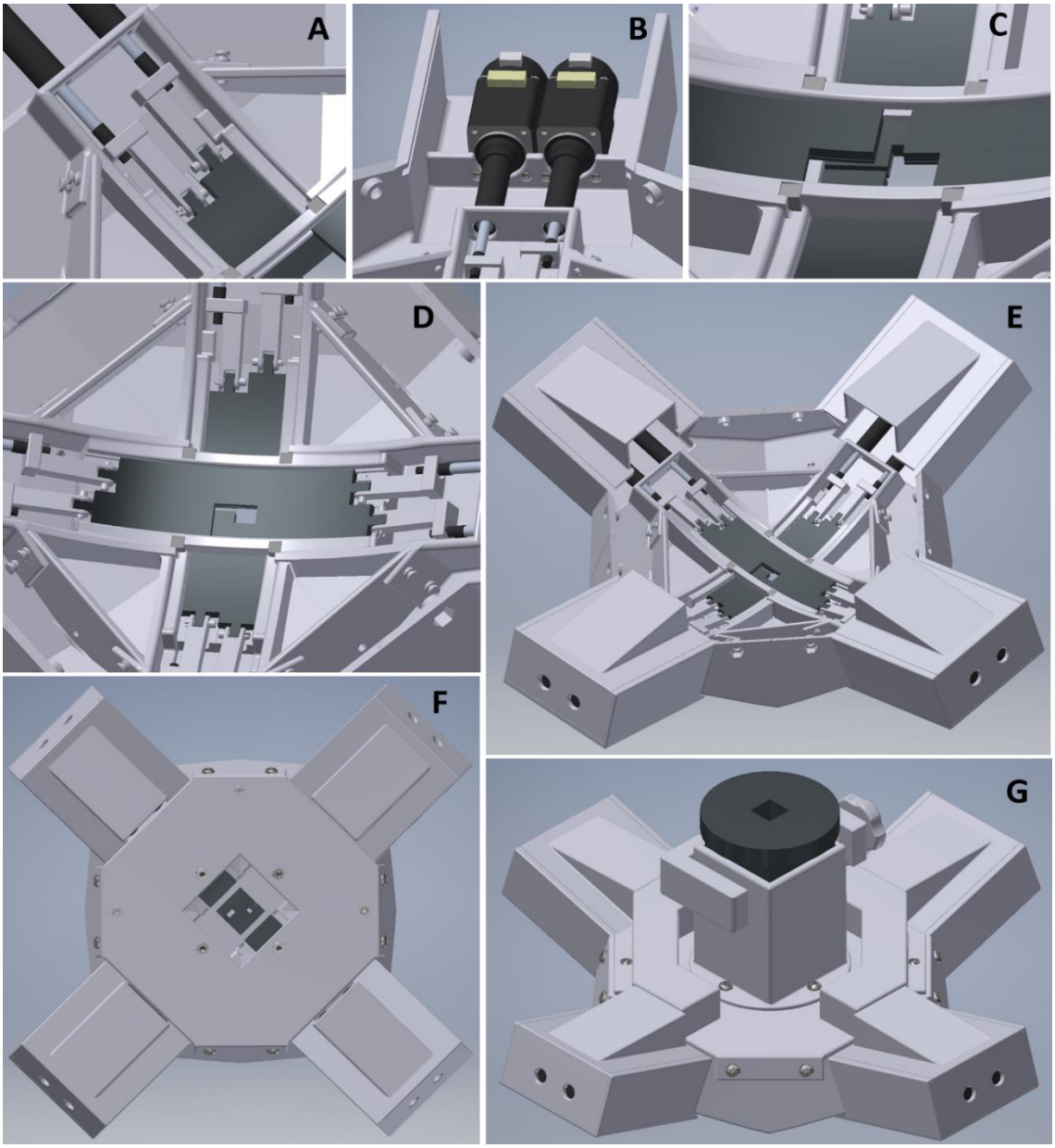

Figure 5-2 CAD model of the SOC. (A) Leaves connected to motor shafts with 3D printed rods and pins. (B) Stepper motor pair screwed into housing. (C) Outer leaf tongues slide along rails in housing. Shown in each corner of the SOC field are tungsten inserts for shielding the corners of the larger 4 x 4 cm primary collimator field. (D) All four orthogonal leaf banks. (E) Covers slide into the housing over each motor bank. (F) Main housing top attached, with mount for square primary collimator. (G) Complete SOC system with adapter to the primary 4x4 cm square SmART collimator. The collimator slides tightly into the adapter with a screw clamp for added support. The C-shaped attachment around the adapter guides the motor cables to the main socket on the back of the SOC.

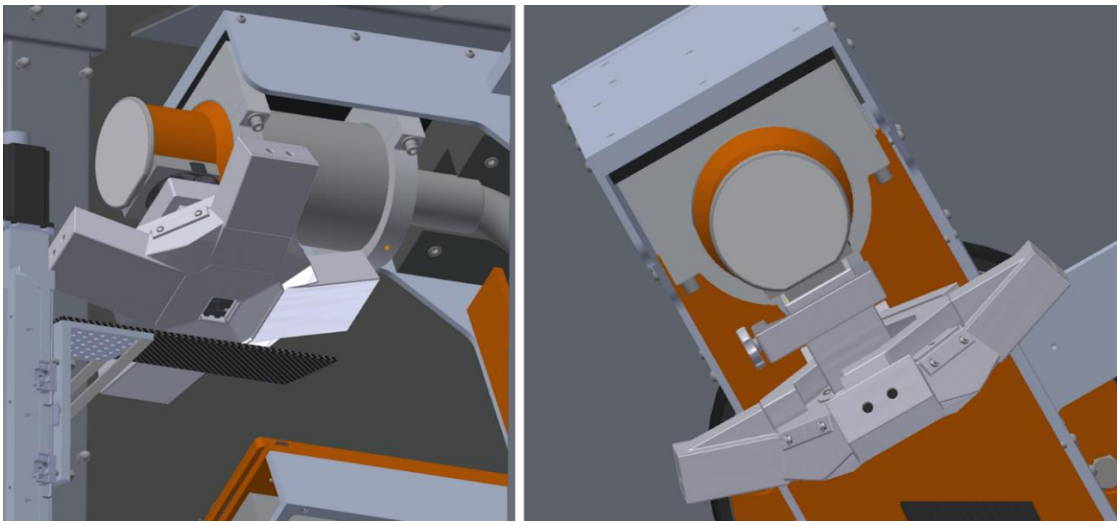

Figure 5-3 The SOC mounted onto the gantry of the SmART system via the primary 4 cm fixed collimator.

5.2.2 SOC Fabrication

The four pairs of leaves for the SOC were machined out of a Class 3 tungsten alloy (95% W, 3.5% Ni, 1.5% Fe; density 18 g/cm^3) by a machine shop (Figure 5-4). While tungsten is considerably more difficult to machine than a softer metal such as copper, its high density is necessary for achieving the desired attenuation with leaves thin enough for the small scale of the SOC.

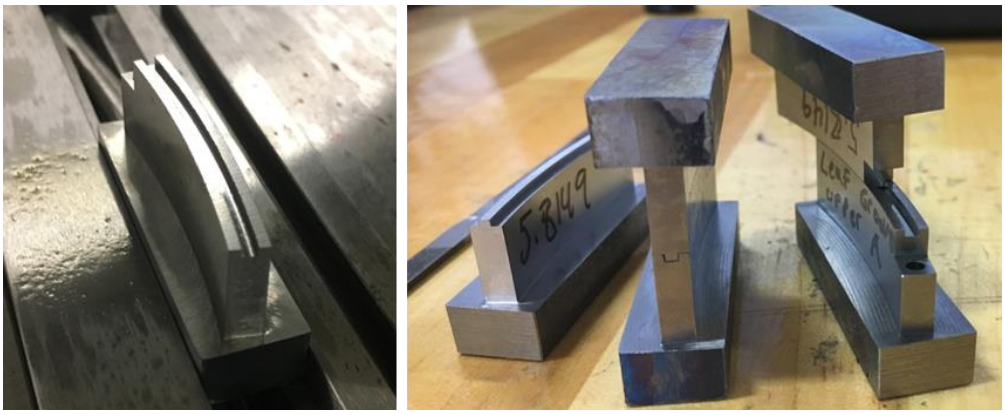

Figure 5-4 Machining of the prototype tungsten alloy leaves for the SOC.

The main housing for the SOC, shown in Figure 5-5, was fabricated out of plastic with stereolithography 3D printing (Formlabs Form 2, White Resin). The primary collimator adapter, which attaches the SOC to the 4 cm square collimator of the SmART system, was also 3D printed. Tungsten cubes (4 mm) were inserted into the housing between perpendicular leaf banks for shielding, since the primary collimator field is larger than the open SOC field.

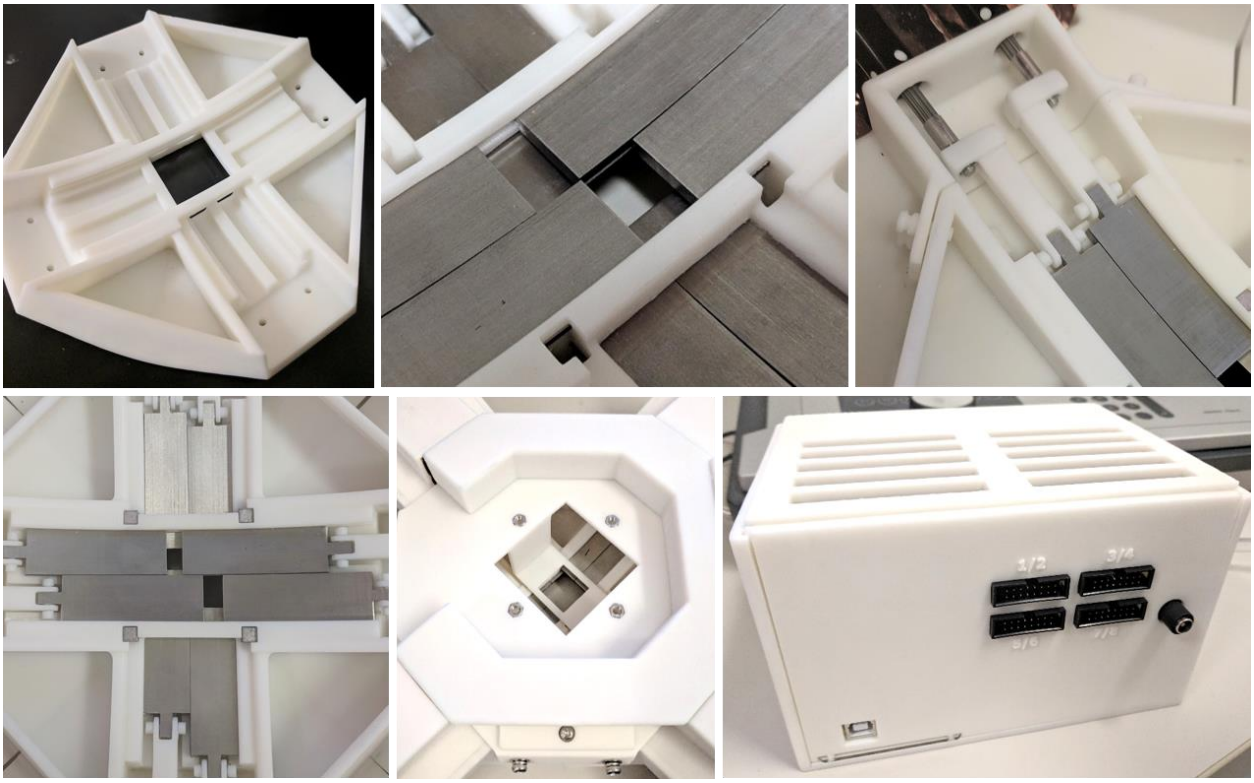

Figure 5-5 3D printed SOC housing: main SOC leaf housing (upper left); outer leaf tongues slide along housing rails (upper middle); leaves attached to motors with 3D printed rods and pins (upper right); housing with all 8 SOC leaves (lower left); housing top with opening for 4 x 4 cm primary collimator and cable guide attachment (lower middle); housing for Arduino board and motor driver boards (lower right).

The SOC leaves are driven by captive stepper motor linear actuators (Haydon Kerk Motion Solutions, Size 8) which have a maximum speed of over 4 cm/sec and resolution of 0.04 mm/step. Rotary encoders are installed for precise leaf position verification with

resolution of <0.02 mm. The motors are wired to stepper motor driver boards (EasyDriver V4.5), which are controlled with an Arduino Mega 2560 microcontroller. These boards enable microstepping with the motors to achieve even finer motor control of 0.005 mm per eighth step.

5.2.3 SOC Control Software

A graphical user interface (GUI) has been developed in Python for controlling the SOC leaf motion (Figure 5-6). The leaves can be moved by either manually dragging the leaf images in the GUI or by loading an aperture sequence from a JavaScript Object Notation (JSON) file. The aperture sequences can also be created or edited within the GUI and saved as a JSON. Leaf motion commands are then sent over a serial connection to the Mega 2560 board, which is loaded with an Arduino program. This program evaluates the new leaf positions for any potential collisions (and sends an error if necessary) then moves each motor the necessary number of steps, using the encoder feedback for verification. The controller proceeds with the treatment once it receives confirmation of successful leaf repositioning. There is also a leaf calibration feature, which allows the user to set a new "zero" position for the leaves.

These aperture sequence files are created in MATLAB following fluence map optimization with RAO and plan post-processing, as described in Chapter 4. The apertures are first shifted to the center of the SOC field, if necessary. The aperture boundaries are converted to a set of eight leaf positions, which are then written to a JSON file for loading into the SOC controller GUI. The couch angle (optional using a 3D printed rotating couch mount,

shown in Figure 5-9), gantry angle, and dwell time are also included, along with an option for manual or automatic sequence progression.

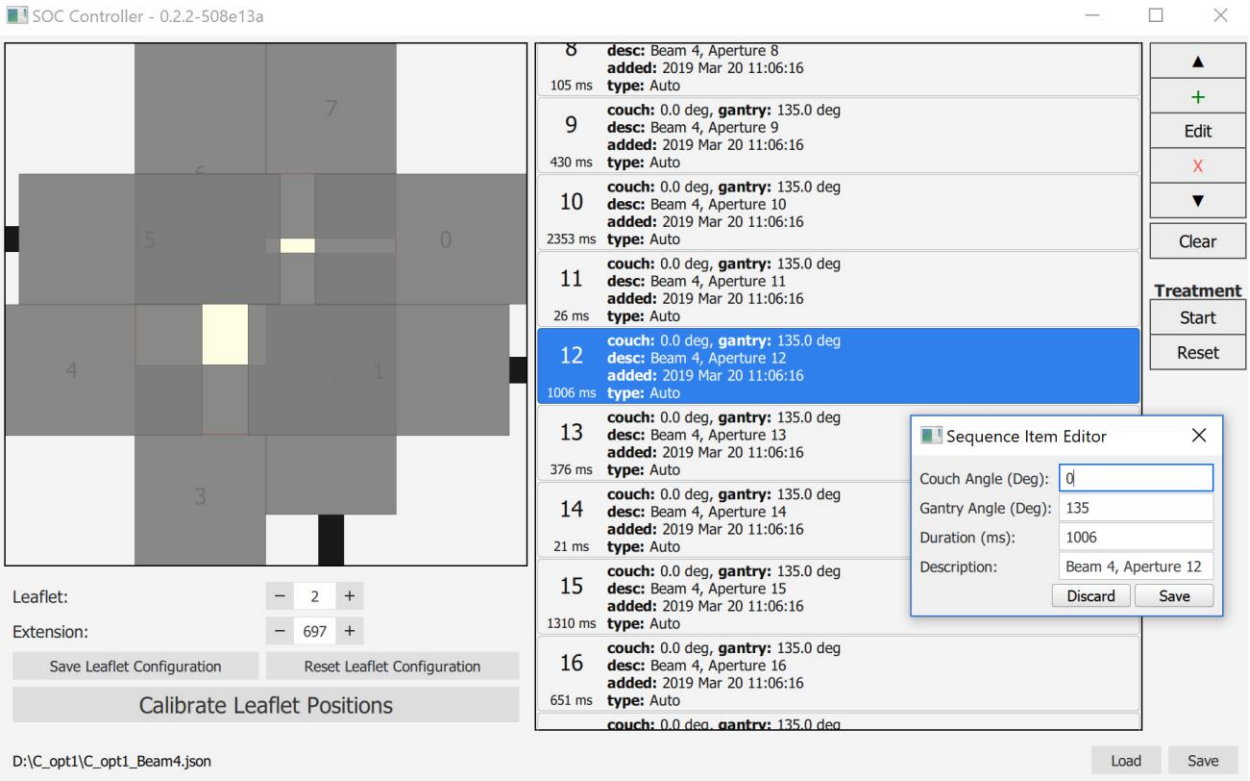

Figure 5-6 Graphic user interface for SOC control, with an aperture sequence loaded from a JavaScript Object Notation (JSON) file. Apertures can be edited and saved using the Sequence Item Editor shown. Leaves can also be controlled by dragging the gray "leaves" on the left. The "Calibrate Leaflet Positions" feature can also be used to set a new leaf "zero" position.

5.2.4 SOC Installation

Prior to initial installation and commissioning of the SOC, the SmART calibration software was used to verify the source-axis-distance (SAD), magnification factor, isocenter location, and center of the detector panel. A Winston-Lutz map of the primary 4 cm square collimator was also created using the system calibration software to factor into the overall system alignment measurements. For this test, PXI's standard 3 mm calibration BB phantom is first moved to the treatment isocenter. Using the projection on the flat panel detector, the

calibration software then measures the offset between the center of the collimator field and the treatment isocenter over a full gantry rotation.

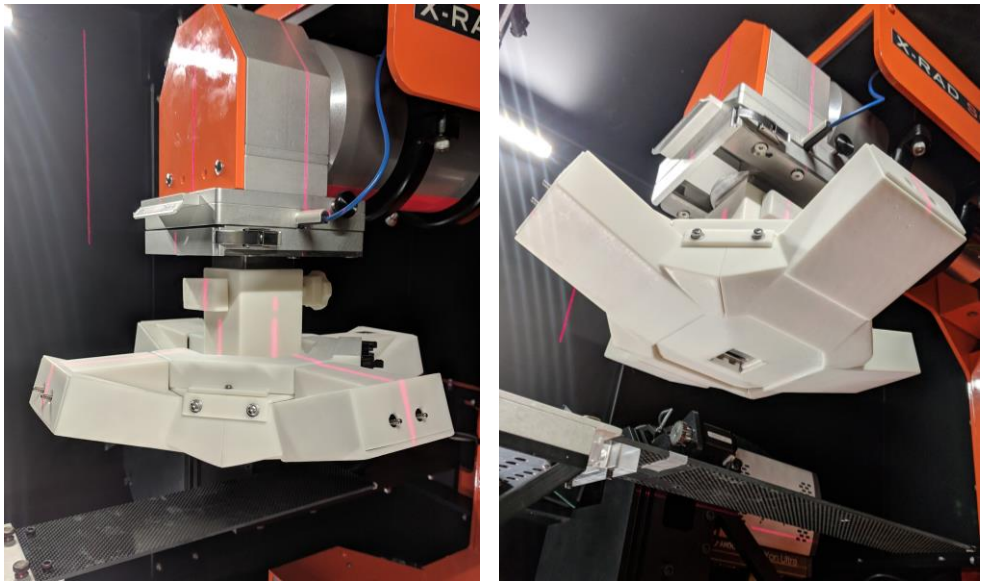

Figure 5-7. SOC installed on SmART system, attached to the 4 x 4 square primary collimator.

The SOC is installed on the head of the SmART by attaching it to the primary collimator with a 3D printed sleeve and clamp (Figure 5-7). Cabling from the electronics (driver boards and microcontroller) to the SOC is fed through a side hole in the cabinet, with shielded cable used inside the cabinet for noise suppression. The leaf positions are then manually calibrated using the fluoroscopy mode of the SmART calibration software. The leaves are extended individually to measure the position of the *x*- and *y*-axis of the SOC, determined by the inner edges of the upper and lower leaves, respectively (Figure 5-8, upper). The leaves are then moved the appropriate distance from each axis for an open field, based on the desired field size at isocenter (maximum 26 x 26 mm) and the measured magnification factor of the system to the flat panel detector. Using the calibration module of

the GUI, these leaf positions are saved as the new “zero” positions for the motor encoders (Figure 5-8, lower).

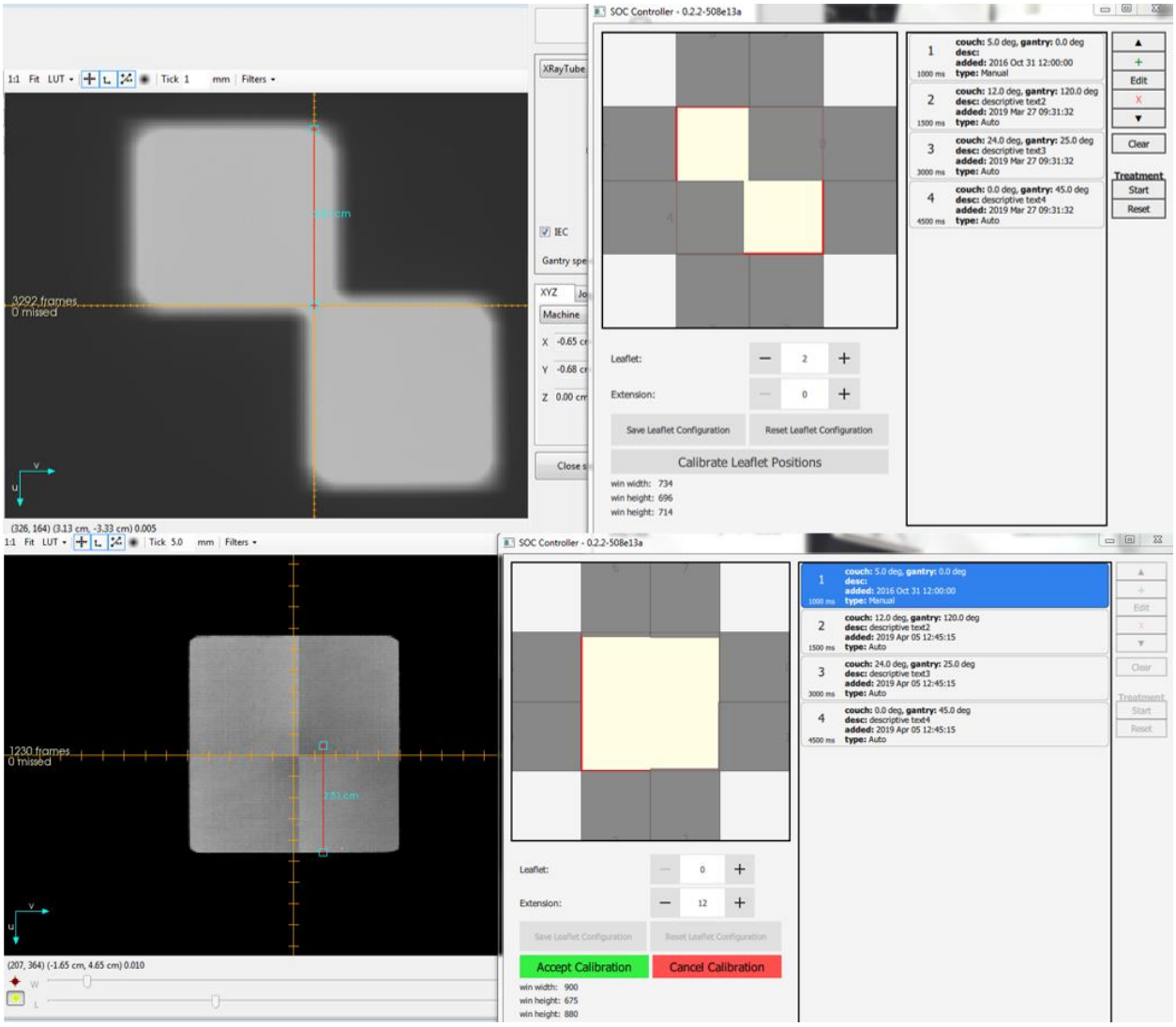

Figure 5-8 SOC leaf position calibration procedure using the fluoroscopy mode of the SmART system calibration software. (Upper) SOC axes are determined from the inner leaf edges. (Lower) open leaf positions are set to the desired distance from each axis and the new calibration is saved with the SOC GUI.

To verify that the leaves are properly aligned to each other and at the correct field size, a simple grid pattern is then delivered to film and the resulting dose distribution is

analyzed. A custom couch-mounted 3D printed film holder is used with standard-sized film squares for reproducible alignment.

5.2.5 SOC Commissioning Measurements

After initial installation, the mechanical accuracy and reproducibility of the SOC were evaluated. The AAPM Task Group 50 report, "Basic Applications of Multileaf Collimators"[134], includes a section for MLC Acceptance Testing, Commissioning, and Safety Assessment describing methods for performing many of the necessary QA tests and measurements for a new MLC. Although some procedures could not be directly translated due to hardware limitations (e.g. no light field or collimator rotation), a series of adapted tests were performed. All film measurements were performed with Gafchromic EBT3 film (lot #10161801) and analyzed with the FilmQA Pro software.

First, the mechanical axes alignment and rotational stability of the SOC were verified. Alignment of the SOC with the gantry axis was measured by exposing the same film, placed at the system isocenter, with both the open SOC field and the 40 mm square primary collimator alone and measuring the distance between field center points. The *x*- and *y*-axes for each collimator were defined by the center of the 50% isodose distribution. This was repeated at 1 cm below isocenter to reveal any angular misalignment. The rotational stability and effects of the extra SOC weight on the gantry alignment were then evaluated by repeating the Winston-Lutz Test previously described with the SOC installed on the primary collimator. A spoke shot pattern was also created for visual verification by exposing film perpendicular to the rotational axis with a 1 mm slit field at 45° increments.

To measure the leaf positioning accuracy, a series of abutting rectangular fields (26 x 4 mm) were delivered to film, and the dose at the matchlines between fields was analyzed. This was repeated for both upper and lower leaf sets (i.e. horizontal and vertical). A grid pattern was then delivered to verify the alignment between the upper and lower leaf sets, and a pixelwise comparison was performed between the 50% isodose distribution and the intended pattern. This grid pattern was delivered several times in a row to assess the leaf position repeatability by measuring the distance between 50% isodose lines. Grids were also compared between different instances of SOC installation and calibration to assess the calibration accuracy.

The transmission through the center of each leaf (mid-leaf), between each tongue and groove joint (inter-leaf), and between opposing leaf faces closed at the field midline (closed leaf) were also measured using film. Measurements were performed for both upper and lower leaf tiers, with the four leaves closed at the midline of the field. This was repeated at gantry angles of 90°, 180°, and 270° to identify any changes in leakage with potential leaf shifts during rotation. Transmission was calculated as the maximum leakage dose divided by the maximum open field dose for the same exposure time. The penumbra, calculated as the distance from 80 to 20% of the maximum dose, was determined for upper and lower leaf faces and edges (tongue and groove) by exposing film with each leaf extended individually to the midline. Because the leaves are double-focused, the leaf face penumbra should not change significantly with leaf position. To verify this, the penumbra was also measured for central square apertures with lengths of 26 (open field), 20, 10, and 5 mm at depths of 2 and 20 mm.

5.2.6 Dosimetric Testing

Three different test plans, either analogous (a highly concave target) or identical (the mouse whole liver and complex 2D "Audrey" plans) to those evaluated in Chapter 4, were delivered for end-to-end testing of the SOC treatment planning and delivery process (Table 5-1). All plans were delivered with a 225 kVp, 20 mA x-ray beam with 0.32 mm added copper filtration.

For the first experiment, the SOC's ability to deliver a 3D concave dose distribution was demonstrated. This type of plan is a hallmark of IMRT and an AAPM standard for IMRT commissioning[135]. A C-shaped target plan was created for a simple 3D printed block phantom (3.5 x 3.5 x 2 cm, Figure 5-9, right) using eight equally spaced coplanar beams, and film was inserted in the center (mid-axial plane) of the phantom to analyze the dose distribution perpendicular to the rotational axis.

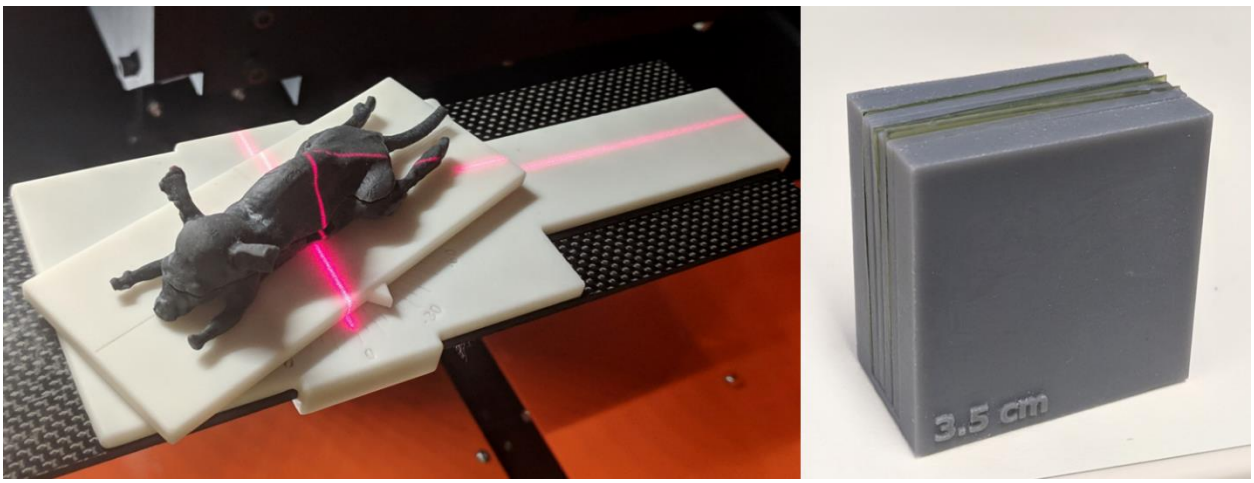

Figure 5-9 (Left) Mouse phantom modeled from mouse CT data and 3D printed with a flexible, tissue-equivalent material and a mid-coronal split for film measurement. Phantom is shown on the previously mentioned rotating couch mount. (Right) 3D printed block phantom for axial dose measurements.

For the second experiment, A 3D printed mouse phantom (Figure 5-9, left) modeled from mouse CT data was used to demonstrate a realistic application for the SOC, as described in Chapter 4. Mouse liver and kidney structures were transferred from a contrast-enhanced mouse CT, and the liver was targeted with a dose of 10 Gy using 5 beam angles optimized with the 4π algorithm[9,10,12-15,26-28,85,122]. Film was inserted between the two phantom halves for dose measurement.

To demonstrate the ability to optimize and deliver complex 2D dose distributions with the SOC, a third test plan with 1 mm resolution and three dose prescription levels (2, 4 and 6 Gy) was delivered. This plan, optimized to resemble an image of Audrey Hepburn as shown in Chapter 4, includes apertures with equivalent square sizes ranging from 1 to 20 mm, with a total of 551 apertures and an average aperture size of 2.35 mm. While this plan is arguably more complex than any foreseeable small animal applications for the SOC, it was developed to visualize the full IMRT capabilities of the system.

Table 5-1 SOC test plan parameters

Test plan	# of beams	Target dose levels	Average # apertures per beam	Average aperture size (mm)	Delivery time (min)[a]	Film measurement set up
C-shaped target	8	1 (10 Gy)	76.6	3.5 ± 1.4	~14	Cube phantom (mid-axial plane)
Mouse liver	5	1 (10 Gy)	101.6	1.8 ± 0.8	~19	Mouse phantom (mid-coronal plane)
Audrey Hepburn	1	3 (2, 4, 6 Gy)	551	2.4 ± 2.1	~19	Below 2 mm solid water

[a]Approximate delivery times were based on a 225 kV, 20 mA beam with an output of 0.461 cGy/mAs. The average leaf motion time was ~400 ms/aperture, accounting for ~20% of total delivery time.

For the C-shaped target and mouse phantom liver plans, the maximum, mean, and minimum structure doses were compared between the measured film dose and the calculated, or intended, dose distribution. A pixelwise comparison was performed for the C-shaped plan and mouse liver plan structures to assess the deviation from the intended dose for each pixel, with the maximum and mean absolute deviations reported. Gamma analysis was also performed to compare the calculated and measured dose distributions, for which the typical clinical criteria are 3% dose-difference and 3 mm distance to agreement (DTA)[136]. In previous studies, these criteria have been adapted for small animal radiotherapy to 4% and 0.3 mm to account for the approximate order of magnitude difference in imaging resolution[137,138]. Thus, 4%/0.3 mm criteria was used for analysis in this study.

5.3 Results

5.3.1 SOC Commissioning

The agreement between the SOC and primary collimator axes at the treatment isocenter was within 0.66 mm in the *x*-direction, and there was no measured offset in the *y*-direction. At 1 cm below isocenter, the measured offsets were 0.40 mm and 0.66 mm in the *x*- and *y*-directions, respectively. This suggests an angular misalignment between the SOC and the primary collimator of approximately 1.5° in *x* and 3.8° in *y*. These measurements are in close agreement with the Winston-Lutz tests, which showed a difference between the two collimators of 0.53 mm and 0 mm in *x* and *y* at the treatment isocenter. Over the full gantry rotation, as shown in Figure 5-10 (left), the maximum deviation of the SOC field center from the treatment isocenter was 1.04 mm in *x* (-1.04 to +0.88) and 1.65 mm in *y* (-1.65 to +0.1).

However, these shifts are reduced when the misalignment of the primary collimator is factored in, suggesting that the rotational stability of the SOC itself is within 1 mm in both directions. This means that this error can be reduced by defining virtual isocenter corrections in the SmART system software, which will adjust the couch to make up for systematic alignment error. This rotational stability is also evident in the spoke shot pattern in Figure 5-10 (right).

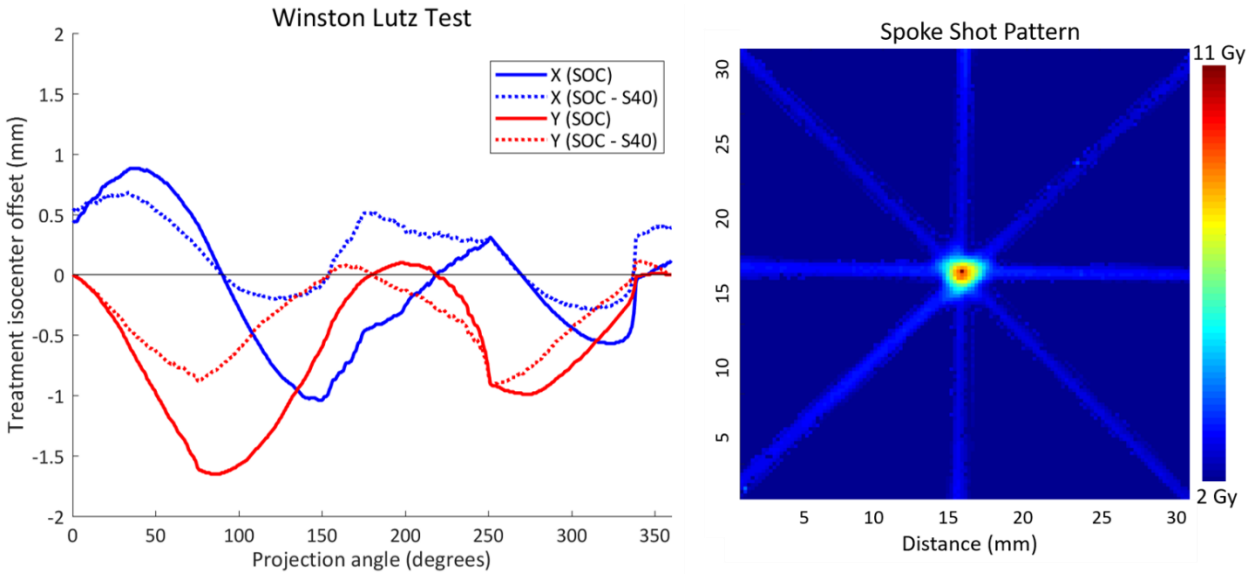

Figure 5-10 (Left) The measured offsets between the SOC field center and treatment isocenter at each projection angle in the x (blue) and y (red) directions are shown with solid lines. The difference between the offsets with the SOC (mounted on the primary collimator) and the primary collimator alone (S40) are shown with dotted lines. (Right) Spoke shot pattern from 1 mm slit SOC fields delivered at 8 equally spaced angles, measured perpendicular to the rotational axis and shown with a 2 Gy minimum dose cutoff.

The upper and lower leaf abutting fields patterns are shown in Figure 5-11 (left, center). Averaged over 6 line profiles, the maximum deviations from the average dose were 18.8 ± 3.1% (mean 4.4 ± 0.5%) and 15.5± 2.9% (mean 1.9 ± 0.2%) for the upper and lower leaf patterns, respectively. These measurements are within the AAPM Task Group 50[134] guideline that dose deviations >20% are indicative of leaf misalignment.

One of the measured grid dose patterns is also shown in Figure 5-11, and the accuracy and repeatability measurements are given in Table 5-2. The pixelwise comparison of the 50% isodose lines for nine grid patterns (from three different calibrations) with the ideal binary grid pattern had a match of 94.4%, with maximum deviations of 0.5 mm. When five sequentially delivered grid patterns were compared to one another to assess the intra-calibration repeatability, there was a slightly lower pixel match of 93% with a maximum deviation of 0.5 mm. This maximum deviation increased slightly to 0.8 mm for grids compared between three different SOC leaf calibrations.

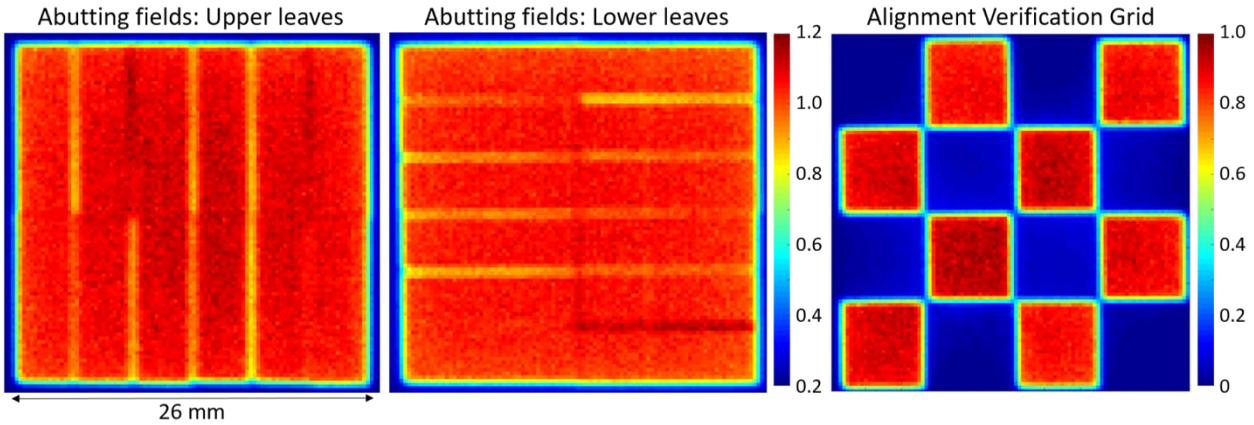

Figure 5-11 Abutting field film patterns for the upper (left) and lower (center) leaves, normalized to the average field dose. (Right) One of the alignment verification grid patterns delivered with the SOC, normalized to the maximum dose.

Table 5-2 Leaf positioning accuracy and repeatability measurements

	# of Grids	% Pixel Match	Maximum Deviation
Accuracy	9 (3 calibrations)	94.4 ± 0.01%	0.5 mm
Intra-calibration repeatability	5 (same calibration)	93%	0.5 mm
Inter-calibration repeatability	3 (3 calibrations)	91%	0.8 mm

The mid-leaf transmission through a single layer of SOC leaves was extremely low, with a maximum measurement of only 0.15 ± 0.05% of the full dose and a mean of $3x10^{-5}$% (Table 5-3). The inter-leaf leakage was 0.27 ± 0.05%, which is well below the AAPM recommended maximum of 3%[134]. There was no statistically significant difference in inter-leaf leakage between measurements at the four major gantry angles, with a maximum difference of +0.07%, suggesting minimal shifting of the SOC leaf pairs with gantry rotation. The maximum closed leaf transmission, measured along the central matchline of all four leaves, was 7.27 ± 3.40%. The rotational difference in closed leaf transmission was again not statistically significant, with a maximum difference of +1.16%. This leakage is likely due to geometrical imperfections in the machined leaf faces and the 3D printed SOC housing, but is still well within the AAPM recommendation of <25%[134]. Also, this transmission is irrelevant for SOC plan delivery, since it can be completely mitigated by using off-axis positions for the upper and lower closed leaf positions.

Table 5-3 SOC leaf transmission and penumbra measurements

Transmission (% full field dose)					
	Mid-leaf (n=8)		**Inter-leaf (n=12)**		**Closed leaf (n=4)**
Maximum transmission (0°)	0.15 ± 0.05% (mean $3x10^{-5}$%)		0.27 ± 0.22%		7.27 ± 3.40%
Maximum rotational variation (0° - 270°)	-		+0.07%		+1.16%
AAPM TG 50 recommendation[134]	<2%		<3%		<25%
Penumbra (80 to 20% dose distance, mm)					
	Upper (n=12)		**Lower (n=12)**		**Average**
	Tongue	*Groove*	*Tongue*	*Groove*	
Leaf edge	0.79 ± 0.04	0.81 ± 0.06	0.82 ± 0.04	0.75 ± 0.07	0.79± 0.05
Leaf face	0.80 ± 0.05		0.80 ± 0.1		0.80 ± 0.08
Square field size (n=4):	**26 mm**	**20 mm**	**10 mm**	**5 mm**	**Range**
2 mm depth	0.86 ± 0.09	0.97 ± 0.10	0.80 ± 0.07	0.80 ± 0.13	0.17
20 mm depth	1.56 ± 0.24	1.26 ± 0.25	1.15 ± 0.14*	1.00 ± 0.12**	0.55

*Significantly different from the 26 mm field penumbra (2-tailed t-test, 5% significance level)

** Significantly different from the 10 and 26 mm field penumbras (2-tailed t-test, 5% significance level)

The leaf penumbra measurements are also shown in Table 5-3. There was no significant difference in penumbra between upper and lower leaf faces, upper and lower leaf edges, or tongue and groove leaf edges. The average leaf edge and face penumbras were 0.79 ± 0.05 mm and 0.80 ± 0.08 mm, respectively, which also had no significant difference. This is beneficial because although leaf edges are not used to form aperture boundaries in a typical SOC plan, they could theoretically be used without resulting in an asymmetrical field penumbra (for example, the delivery of two diagonal quadrants with a single leaf layer). For measurements at 2 mm depth, there was no significant difference in penumbra with leaf position for square apertures 5 to 26 mm, with a range of 0.17 mm. There was slightly more variation in penumbra at 20 mm depth, with a range of 0.55 mm and significant differences between several of the field sizes (5 vs 10 mm, 5 vs 26 mm, and 10 vs 26 mm). It should be

noted that the source-to-leaf distance of the SOC was extended after machining of the current leaves in order to achieve superior dosimetry at the treatment isocenter. Therefore the radius of curvature of these leaves is slightly less than it would be for a fully double-focused system, which would theoretically result in a more consistent leaf penumbra. However, based on the system and setup geometry, the measured penumbra range at 2 mm depth suggests a focal spot size of 2.6 to 3.1 mm. Since the reported diameter is approximately 3 mm, the large focal spot is likely the main source of the measured penumbra.

5.3.2 Dosimetric Testing

Figure 5-12 shows the calculated (left) and measured (center) dose distributions for the C-shaped target plan. The gamma analysis with 4%/0.3 mm criteria revealed a pass rate of ~95% for pixels within the target structure, and 85% for the entire field shown. The maximum and mean absolute pixelwise dose differences were 4.12 and 0.59 Gy, respectively (Table 5-4), and the measured dose to the target had slightly higher maximum (15.8% of the prescription dose), mean (7.0%), and minimum (13.5%) doses. The 50% isodose lines are shown in Figure 5-12 (right), demonstrating excellent overall agreement between the calculated and measured dose distributions.

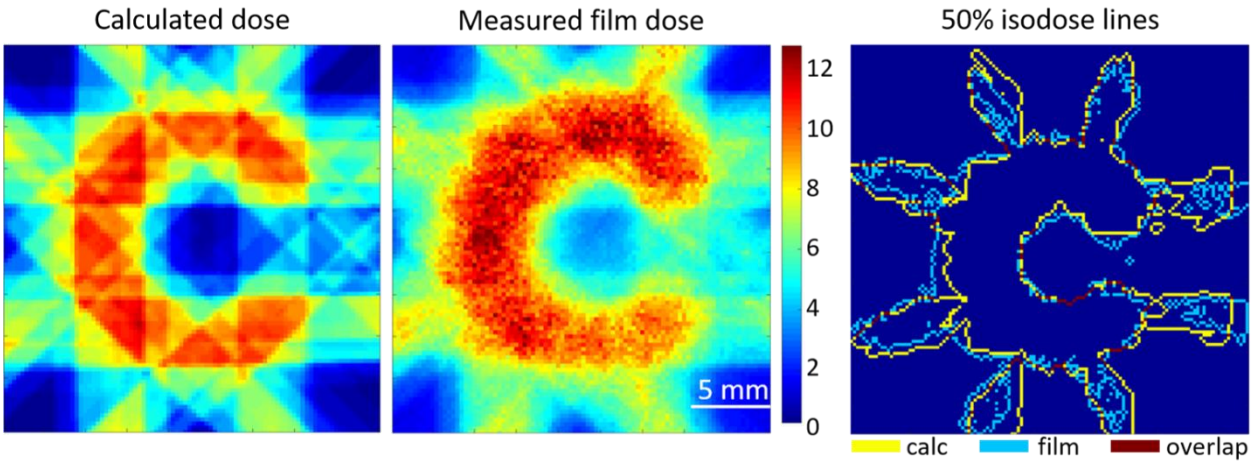

Figure 5-12 (Left) Calculated dose distribution of the C-shaped target plan perpendicular to the gantry rotation axis. (Center) Measured film dose distribution from the center of the solid water phantom for the C target plan delivered with the SOC. Both plans are shown with the same color scale, in units of Gy. (Right) A comparison of the calculated (yellow) and measured (blue) 50% isodose lines, with overlapping regions shown in red.

The results of the mouse phantom liver test plan are shown in Figure 5-13, with the liver and kidney dose comparisons given in Table 5-4. The maximum measured liver dose was 13.0% higher than the calculated dose, the mean was 10.2% lower, and the minimum was 11.0% higher. As evident in the film dose distribution and isodose comparison shown in Figure 5-13 (C) and (D), the lower left portion of the liver was cut off due to slight phantom misalignment. The affected pixels were omitted from the liver dose analysis, and the measured dose distribution was rotated slightly to account for the setup error. For the unaffected pixels within the liver, the gamma analysis showed a high pass rate of 98.2%. The measured SOC plan was also able to significantly spare the dose to the kidneys (based on the location of the kidney contours in relation to the liver in the measurement plane) with maximum and mean doses of 0.43 and 0.24 Gy, respectively. These are only 4.3% and 2.4% higher than the calculated doses, and all pixels in the kidneys met the 4%/0.3 mm gamma criteria.

Table 5-4 Comparisons between the measured and intended dose distributions for the C-shaped target plan and the mouse phantom whole liver plan[a]

		Structure Dose Deviations (measured – calculated)			Pixelwise Dose Comparison		
Plan	*Structure*	*Max*	*Mean*	*Min*	*Max Diff*	*Mean Diff*	*Gamma Pass Rate*
C Target	C	+1.58 (15.8%)	+0.70 (7.0%)	+1.35 (13.5%)	4.12 (41.2%)	0.59 (5.91%)	94.9%
Mouse Liver	Liver	+1.30 (13.0%)	-1.02 (10.2%)	+1.10 (11.0%)	3.50 (35.0%)	1.19 (11.9%)	98.2%
	Kidneys	+0.43 (4.3%)	+0.24 (2.4%)	+0.11 (1.1%)	0.43 (4.3%)	0.24 (2.4%)	100%

[a]Maximum, mean, and minimum dose differences written as [Gy (% prescription dose)]; Max and Mean Diff are absolute pixelwise dose differences; gamma analysis was performed with 4%/0.3 mm criteria for dose/distance

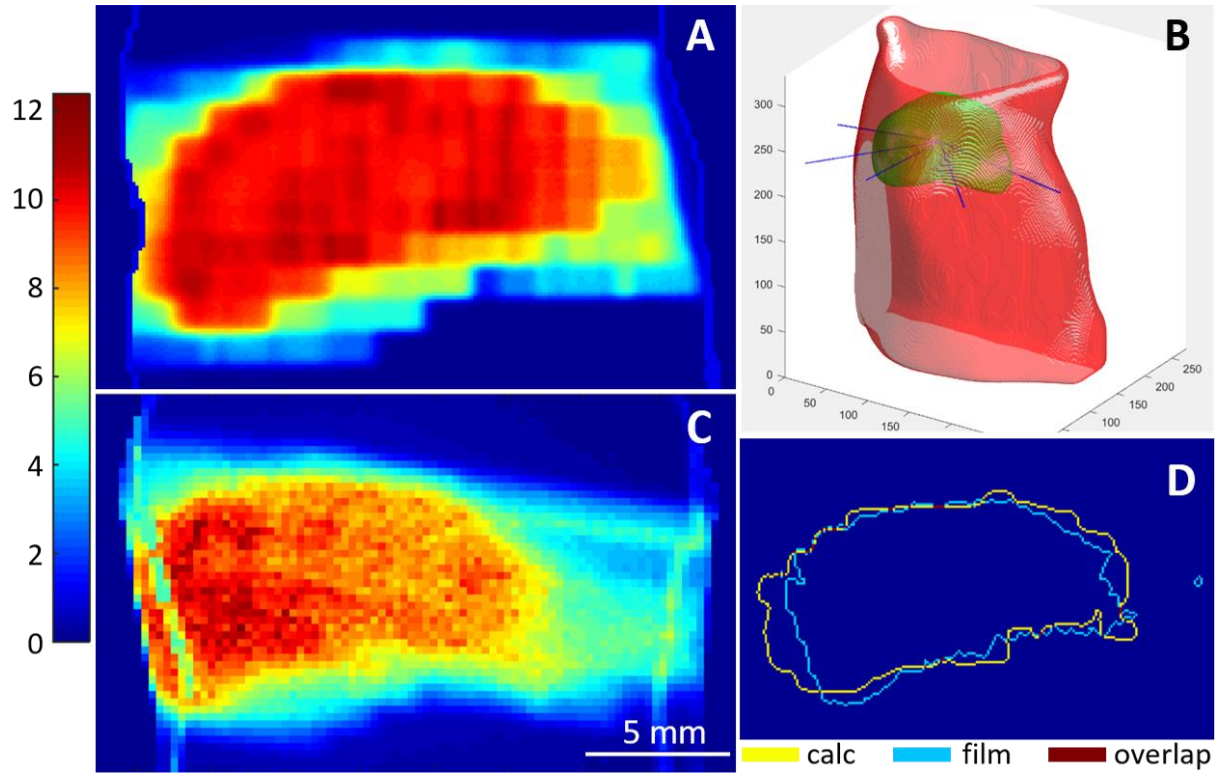

Figure 5-13 (A) Mid-coronal view of the calculated dose for the mouse phantom whole liver plan (units of Gy). (B) The 5 optimal coplanar beam angles selected with the 4π algorithm. (C) Measured film dose from the mouse phantom, treated with the whole liver plan, at the plane shown in (A) (units of Gy). (D) A comparison of the calculated (yellow) and measured (blue) 60% isodose lines, with overlapping regions shown in red. Target structure was rotated to account for slight phantom misalignment, which also resulted in the truncated lower left portion of the target.

The calculated and measured doses for the 2-dimensional Audrey test plan are shown in Figure 5-14. The maximum and minimum measured film doses were both 1.1 Gy higher than the calculated dose distribution (12.2% of the maximum intended dose), with a mean pixelwise absolute dose difference of 1.6 Gy. Although this plan shows some discrepancies in absolute dose prediction for very small apertures sizes, the sources of which are discussed in Chapter 4, the spatial distribution is extremely similar to the calculated plan, validating the overall accuracy of the SOC hardware and control software.

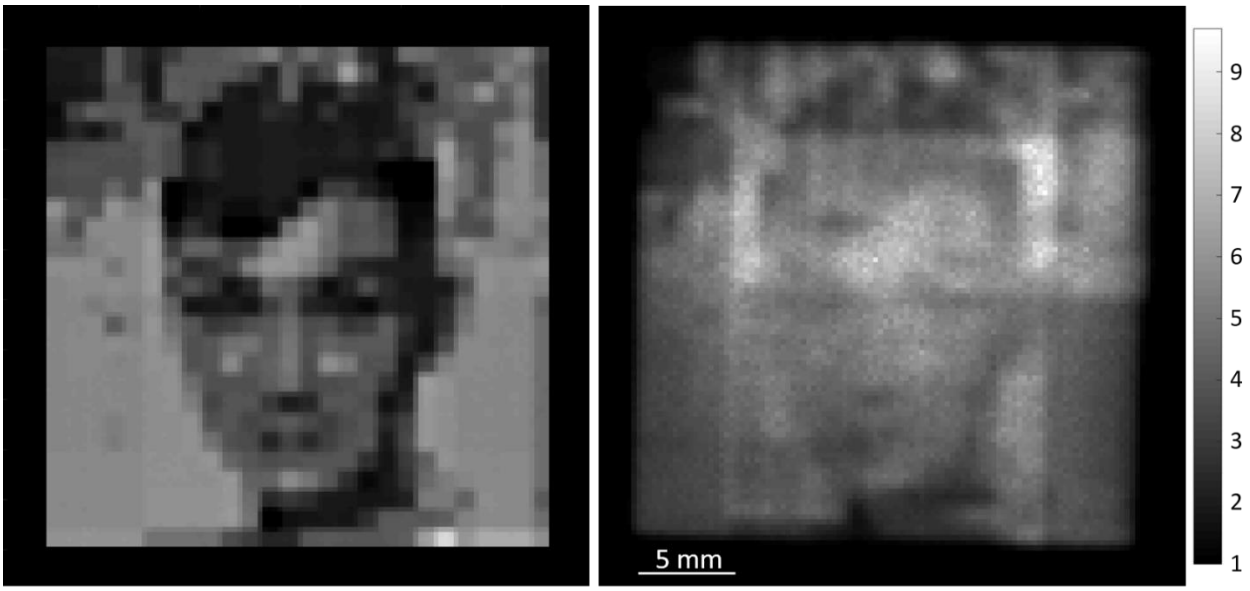

Figure 5-14 (Left) Calculated Audrey test plan with 4 dose levels and an average aperture size of 2.35 mm. (Right) Measured dose distribution of the Audrey plan delivered with the SOC. Both plans are shown with the same color scale, in units of Gy.

5.4 Discussion

In addition to the planning dosimetry capability of SOC for preclinical x-ray IMRT shown in Chapter 4, the engineering feasibility, fabrication, and delivery dosimetry performance of the SOC is demonstrated in this chapter. Compared to the MLC, we believe

that the SOC is better suited for preclinical applications. First of all, SOC resolution is independent of the leaf width in both collimation directions, avoiding the engineering challenge of further reducing the MLC leaf width. Consequently, the SOC has substantially fewer moving components than the MLC, making miniaturization feasible and more robust. SOC modulation resolution depends on leaf step size, which is determined by the stepper motors, and can therefore in theory be on the order of a micron. In practice, this mechanical resolution is limited by the resolution of the motor encoders and the accuracy of the housing fabrication, but is still well below a millimeter for the described SOC design. The current RAO formulation described in Chapter 4, however, does have a finite beamlet resolution due to the discretized nature of the rectangles, which does not take full advantage of the resolution capabilities of the SOC geometry. Further investigation of a multi-resolution approach must be conducted to better exploit this design.

The SOC design is also advantageous over a conventional MLC because it makes closed leaf end transmission inconsequential. While this is significantly lessened with a dual-layer MLC, this configuration still has a region of higher transmission where the closed leaf matchlines intersect. These matchlines are not necessary with the SOC, since it is possible to block the entire SOC field without even fully closing opposing leaf pairs. The maximum transmission in this SOC configuration would be from the photons in the center point of the field, passing through both upper and lower tongue and groove joints, which would only be approximately 0.07% based on our interleaf transmission measurements. In general, these low transmission levels are a major advantage of the SOC leaf design, with our measurements suggesting an average mid-leaf transmission through both layers of only about 0.02%.

Although the inherent delivery efficiency of the SOC design is lower than that of a typical MLC system, the ability to deliver two fields in diagonal quadrants simultaneously can potentially reduce delivery times by up to 50% compared to jaws-only IMRT. These reductions are even greater when we consider the added time from off-axis aperture couch shifts with a system like the motorized variable collimator. Also, the SOC aperture optimization can be easily tuned to select fewer, larger apertures for plans where short delivery times are a priority. Additionally, although currently the leaf repositioning time is ~400 ms/aperture and accounts for approximately 20% of the overall delivery time, we believe there is significant room for reduction with more optimized leaf motion control.

Overall, the preliminary results from the SOC are promising. The SOC leaves have a very consistent penumbra, varying by only 0.17 mm with leaf position at 2 mm depth and with no measurable difference between the upper and lower sets, despite the current discrepancy between the beam divergence and leaf radii. Using just the quick, simple leaf position calibration procedure described, abutting field patterns were delivered with <20% dose difference at the matchlines, as recommended by AAPM guidelines[134]. In the C-shaped target experiment, the SOC achieved a highly concave dose distribution that agreed well with the intended 50% isodose area and had a gamma pass rate of 94.9% within the target for 4%/0.3 mm criteria. An end-to-end test of a realistic SOC application was performed with the mouse phantom whole liver plan, demonstrating all steps from the mouse CT scan to the final treatment delivery. With this plan, a conformal dose was delivered to the mouse liver while significantly sparing dose to the kidneys. The measured and intended target doses

were again in close agreement, with a gamma pass rate of 98.2%. The ability to create and deliver a highly complex 2D dose distribution was also demonstrated with Audrey plan.

However, there is still a significant degree of error and uncertainty with the current SOC system. In addition to the dosimetric error discussed in Chapter 4, there are also various sources of geometrical uncertainty. The first is misalignment of the SOC with the primary collimator, which we measured to be approximately 0.7 mm at a gantry angle of 0°. Combined with the existing misalignment between the primary collimator and the gantry axis, this resulted in measured deviations from the treatment isocenter of up to 1.65 mm for a full gantry rotation. There is also uncertainty in the leaf calibration procedure, with leaf position deviations of up to 0.8 mm observed between calibrations. Leaf position repeatability measurements with the same calibration also showed differences of up to 0.5 mm. Since this is well below the resolution of the encoders, it is more likely due to slight shifting of the motors within the SOC housing, or inconsistencies in the leaf movement relative to the motors.

The largest source of geometric error is currently the subject setup. The treatment planning process is not yet fully automated and currently takes several hours for complex plans, although there is significant potential for acceleration. Therefore planning cannot yet be realistically performed with the subject on the couch, and the subject setup in the planning CT must be recreated for treatment delivery. Although this is standard practice in clinical treatment, the SmART system software lacks the highly automated tools used for reproducible patient setup in the clinic. Subject setup for SOC treatment is a much more manual process with greater uncertainty, likely on the order of a couple millimeters or

degrees of misalignment. Even with a fast, fully integrated treatment planning system, this error will not be completely mitigated until a more permanent (or at least more reproducible) SOC installation is possible, since the SOC must currently be reinstalled and recalibrated between imaging and treatment. It should also be noted that all measurements (apart from the Winston-Lutz test) were performed with EBT3 film, which has an inherent uncertainty of ~2%[139,140] in dose and was limited by our scanning resolution of 96 dpi, which was used by default. This could be increased for higher resolution analysis, but at the expense of increased noise.

Although these sources of geometric and dosimetric error add up to significant uncertainties with current SOC treatment, the majority of this error could be substantially reduced with integration into the SmART system. The x-ray beam is currently controlled with the console during SOC treatment, requiring the user to manually start and stop the beam. Integration with the SmART software would enable automated beam control, which is especially beneficial for pausing the beam if any hardware errors are detected. This would also allow us to develop a more accurate, automated calibration procedure using the projected leaf positions on the flat panel detector. More permanent installation on the SOC gantry, or at least a custom adapter to bypass the primary 4 x 4 cm collimator attachment, could significantly reduce the treatment isocenter misalignment and the potential for setup error between imaging and treatment.

5.5 Conclusions

The sparse orthogonal collimator was designed as a simple, more practical dose modulation device for small animal IMRT. This SOC design is driven by a novel direct aperture optimization algorithm that uses only rectangular apertures for complex dose modulation. With the complete SOC hardware and commissioned planning system, we demonstrated extremely low leaf transmission, consistent penumbra, and the ability to deliver conformal, complex dose distributions in close agreement with intended treatment plans. This novel system could considerably enhance our ability to perform clinically translatable animal radiation research in both cancer and non-cancer related fields.

6 REFERENCES

1. International Agency for Research on Cancer GLOBOCAN 2018. *Cancer Fact Sheets: All Cancers.* Lyon, France: World Health Organization;2019.
2. Delaney G, Jacob S, Featherstone C, Barton M. The role of radiotherapy in cancer treatment: estimating optimal utilization from a review of evidence-based clinical guidelines [published online ahead of print 08/05]. *Cancer.* 2005;104(6):1129-1137.
3. Bryant AK, Banegas MP, Martinez ME, Mell LK, Murphy JD. Trends in Radiation Therapy among Cancer Survivors in the United States, 2000-2030 [published online ahead of print 01/18]. *Cancer Epidemiol Biomarkers Prev.* 2017;26(6):963-970.
4. Zou W, Dong L, Kevin Teo BK. Current State of Image Guidance in Radiation Oncology: Implications for PTV Margin Expansion and Adaptive Therapy [published online ahead of print 06/24]. *Seminars in radiation oncology.* 2018;28(3):238-247.
5. Mittauer K, Paliwal B, Hill P, et al. A New Era of Image Guidance with Magnetic Resonance-guided Radiation Therapy for Abdominal and Thoracic Malignancies. *Cureus.*10(4).
6. Pollard JM, Wen Z, Sadagopan R, Wang J, Ibbott GS. The future of image-guided radiotherapy will be MR guided. *Br J Radiol.* 2017;90(1073).
7. de Pooter JA, Mendez Romero A, Wunderink W, Storchi PR, Heijmen BJ. Automated non-coplanar beam direction optimization improves IMRT in SBRT of liver metastasis [published online ahead of print 07/01]. *Radiotherapy and oncology : journal of the European Society for Therapeutic Radiology and Oncology.* 2008;88(3):376-381.
8. Dong P, Lee P, Ruan D, et al. 4pi non-coplanar liver SBRT: a novel delivery technique. *Int J Radiat Oncol Biol Phys.* 2013;85(5):1360-1366.
9. Dong P, Lee P, Ruan D, et al. 4pi noncoplanar stereotactic body radiation therapy for centrally located or larger lung tumors [published online ahead of print 03/26]. *International journal of radiation oncology, biology, physics.* 2013;86(3):407-413.
10. Rwigema JC, Nguyen D, Heron DE, et al. 4pi noncoplanar stereotactic body radiation therapy for head-and-neck cancer: potential to improve tumor control and late toxicity [published online ahead of print 12/09]. *International journal of radiation oncology, biology, physics.* 2015;91(2):401-409.
11. Dong P, Nguyen D, Ruan D, et al. Feasibility of prostate robotic radiation therapy on conventional C-arm linacs [published online ahead of print 07/12]. *Practical radiation oncology.* 2014;4(4):254-260.
12. Tran A, Zhang J, Woods K, et al. Treatment planning comparison of IMPT, VMAT and 4π radiotherapy for prostate cases. *Radiation Oncology.* 2017;12(1):10.

13. Nguyen D, Rwigema JC, Yu VY, et al. Feasibility of extreme dose escalation for glioblastoma multiforme using 4π radiotherapy. *Radiation oncology (London, England).* 2014;9.

14. Yu VY, Tran A, Nguyen D, et al. Significant Cord and Esophagus Dose Reduction by 4π Non-Coplanar Spine Stereotactic Body Radiation Therapy and Stereotactic Radiosurgery. *International journal of radiation oncology, bioogy, physics.* 2016;96(2).

15. Yu VY, Tran A, Nguyen D, et al. The development and verification of a highly accurate collision prediction model for automated noncoplanar plan delivery. *Medical Physics.* 2015;42(11):6457-6467.

16. Kahn J, Tofilon PJ, Camphausen K. Preclinical models in radiation oncology. *Radiation Oncology.* 2012;7(1):223.

17. Rosenthal N, Brown S. The mouse ascending: perspectives for human-disease models [published online ahead of print 09/01]. *Nature cell biology.* 2007;9(9):993-999.

18. Coleman CN, Higgins GS, Brown JM, et al. Improving the Predictive Value of Preclinical Studies in Support of Radiotherapy Clinical Trials [published online ahead of print 05/08]. *Clinical cancer research : an official journal of the American Association for Cancer Research.* 2016;22(13):3138-3147.

19. Mak IW, Evaniew N, Ghert M. Lost in translation: animal models and clinical trials in cancer treatment [published online ahead of print 02/04]. *American journal of translational research.* 2014;6(2):114-118.

20. Denayer T, Stöhr T, Van Roy M. Animal models in translational medicine: Validation and prediction. *New Horizons in Translational Medicine.* 2014;2(1):5-11.

21. Day C-P, Merlino G, Van Dyke T. Preclinical Mouse Cancer Models: A Maze of Opportunities and Challenges. *Cell.* 2015;163(1):39-53.

22. Zhou H, Rodriguez M, van den Haak F, et al. Development of a micro-computed tomography-based image-guided conformal radiotherapy system for small animals [published online ahead of print 04/17]. *International journal of radiation oncology, biology, physics.* 2010;78(1):297-305.

23. Jensen MD, Hrinivich WT, Jung JA, et al. Implementation and commissioning of an integrated micro-CTRT system with computerized independent jaw collimation [published online ahead of print 08/10]. *Medical Physics.* 2013;40(8):081706.

24. Prajapati S, Cox B, Swader R, et al. Design of an open-source binary micro-multileaf collimator (bmMLC) for a small animal micro-radiotherapy system. *Journal of Medical Devices.* 2018;11(4).

25. Stewart JM, Lindsay PE, Jaffray DA. Two-dimensional inverse planning and delivery with a preclinical image guided microirradiator [published online ahead of print 10/05]. *Medical Physics.* 2013;40(10):101709.

26. Woods K, Nguyen D, Tran A, et al. Viability of Non-Coplanar VMAT for Liver SBRT as Compared to Coplanar VMAT and Beam Orientation Optimized 4pi IMRT [published online ahead of print 04/23]. *Advances in radiation oncology.* 2016;1(1):67-75.

27. Woods K, Lee P, Kaprealian T, Yang I, Sheng K. Cochlea-sparing acoustic neuroma treatment with 4π radiotherapy. *Advances in radiation oncology.* 2018;3(2):100-107.

28. Murzin VL, Woods K, Moiseenko V, et al. 4pi plan optimization for cortical-sparing brain radiotherapy [published online ahead of print 03/10]. *Radiotherapy and oncology : journal of the European Society for Therapeutic Radiology and Oncology.* 2018;127(1):128-135.

29. Woods K, Nguyen D, Neph R, Ruan D, O'Connor D, Sheng K. A Sparse Orthogonal Collimator for Small Animal Intensity Modulated Radiation Therapy, Part I: Planning System Development and Commissioning. In submission.

30. Woods K, Neph R, Nguyen D, Sheng K. A Sparse Orthogonal Collimator for Small Animal Intensity Modulated Radiation Therapy, Part II: Hardware Development and Commissioning. In submission.

31. Chang DT, Swaminath A, Kozak M, et al. Stereotactic body radiotherapy for colorectal liver metastases: a pooled analysis [published online ahead of print 03/25]. *Cancer.* 2011;117(17):4060-4069.

32. Lawrence TS, Robertson JM, Anscher MS, Jirtle RL, Ensminger WD, Fajardo LF. Hepatic toxicity resulting from cancer treatment [published online ahead of print 03/30]. *International journal of radiation oncology, biology, physics.* 1995;31(5):1237-1248.

33. Wahl DR, Stenmark MH, Tao Y, et al. Outcomes After Stereotactic Body Radiotherapy or Radiofrequency Ablation for Hepatocellular Carcinoma [published online ahead of print 12/03]. *Journal of clinical oncology : official journal of the American Society of Clinical Oncology.* 2015;34(5):452-459.

34. Price TR, Perkins SM, Sandrasegaran K, et al. Evaluation of response after stereotactic body radiotherapy for hepatocellular carcinoma [published online ahead of print 10/26]. *Cancer.* 2011;118(12):3191-3198.

35. Rusthoven KE, Kavanagh BD, Cardenes H, et al. Multi-institutional phase I/II trial of stereotactic body radiation therapy for liver metastases [published online ahead of print 03/04]. *Journal of clinical oncology : official journal of the American Society of Clinical Oncology.* 2009;27(10):1572-1578.

36. Mornex F, Girard N, Merle P, et al. [Tolerance and efficacy of conformal radiotherapy for hepatocellular carcinoma in cirrhotic patients. Results of the French RTF1 phase II trial] [published online ahead of print 10/13]. *Cancer radiotherapie : journal de la Societe francaise de radiotherapie oncologique.* 2005;9(6-7):470-476.

37. Wang PM, Hsu WC, Chung NN, et al. Feasibility of stereotactic body radiation therapy with volumetric modulated arc therapy and high intensity photon beams for hepatocellular carcinoma patients [published online ahead of print 01/15]. *Radiation oncology (London, England).* 2014;9:18.

38. Thomas E, Chapet O, Kessler ML, Lawrence TS, Ten Haken RK. Benefit of using biologic parameters (EUD and NTCP) in IMRT optimization for treatment of intrahepatic tumors [published online ahead of print 05/14]. *International journal of radiation oncology, biology, physics.* 2005;62(2):571-578.

39. Dong P, Lee P, Ruan D, et al. 4pi non-coplanar liver SBRT: a novel delivery technique [published online ahead of print 11/17]. *International journal of radiation oncology, biology, physics.* 2012;85(5):1360-1366.

40. Yu VY, Tran A, Nguyen D, et al. The development and verification of a highly accurate collision prediction model for automated noncoplanar plan delivery. *Medical Physics.* 2015;42(11):6457-6467.

41. Romeijn HE, Ahuja RK, Dempsey JF, Kumar A. A Column Generation Approach to Radiation Therapy Treatment Planning Using Aperture Modulation [published online ahead of print 2005]. *SIAM J Optim.* 2005;15(3):838-862.

42. van't Riet A, Mak AC, Moerland MA, Elders LH, van der Zee W. A conformation number to quantify the degree of conformality in brachytherapy and external beam irradiation: application to the prostate [published online ahead of print 02/01]. *International journal of radiation oncology, biology, physics.* 1997;37(3):731-736.

43. J Deacon MJPGGS. The radioresponse of human tumors and the initial slope of the cell survival curve. *Radiotherapy and oncology : journal of the European Society for Therapeutic Radiology and Oncology.* 1985;2(4).

44. Fertil B, Malaise EP. Intrinsic radiosensitivity of human cell lines is correlated with radioresponsiveness of human tumors: analysis of 101 published survival curves [published online ahead of print 09/01]. *International journal of radiation oncology, biology, physics.* 1985;11(9):1699-1707.

45. Kutcher GJ, Burman C. Calculation of complication probability factors for non-uniform normal tissue irradiation: The effective volume method gerald. *International Journal of Radiation Oncology*Biology*Physics.* 1989;16(6):1623-1630.

46. Lyman JT. Complication probability as assessed from dose-volume histograms [published online ahead of print 01/01]. *Radiation research Supplement.* 1985;8:S13-19.

47. Dawson LA, Normolle D, Balter JM, McGinn CJ, Lawrence TS, Ten Haken RK. Analysis of radiation-induced liver disease using the Lyman NTCP model [published online ahead of print 07/04]. *International journal of radiation oncology, biology, physics.* 2002;53(4):810-821.

48. Dawson LA, Eccles C, Craig T. Individualized image guided iso-NTCP based liver cancer SBRT [published online ahead of print 09/20]. *Acta oncologica (Stockholm, Sweden).* 2006;45(7):856-864.

49. Tai A, Erickson B, Khater KA, Li XA. Estimate of radiobiologic parameters from clinical data for biologically based treatment planning for liver irradiation [published online ahead of print 02/12]. *International journal of radiation oncology, biology, physics.* 2008;70(3):900-907.

50. Podgorsak EB, Pike GB, Olivier A, Pla M, Souhami L. Radiosurgery with high energy photon beams: a comparison among techniques [published online ahead of print 03/01]. *International journal of radiation oncology, biology, physics.* 1989;16(3):857-865.

51. Timmerman RD, Park C, Kavanagh BD. The North American experience with stereotactic body radiation therapy in non-small cell lung cancer. *Journal of Thoracic Oncology.* 2007;2(7):S101-S112.

52. Yang J, Fowler JF, Lamond JP, Lanciano R, Feng J, Brady LW. Red shell: defining a high-risk zone of normal tissue damage in stereotactic body radiation therapy [published online ahead of print 04/20]. *International journal of radiation oncology, biology, physics.* 2010;77(3):903-909.

53. Timmerman R, Kavanagh B. Stereotactic Body Radiation Therapy *Lippincott Williams & Wilkins.* 2004.

54. Derycke S, Van Duyse B, De Gersem W, De Wagter C, De Neve W. Non-coplanar beam intensity modulation allows large dose escalation in stage III lung cancer [published online ahead of print 1998/01/13]. *Radiother Oncol.* 1997;45(3):253-261.

55. Christian JA, Bedford JL, Webb S, Brada M. Comparison of inverse-planned three-dimensional conformal radiotherapy and intensity-modulated radiotherapy for non-small-cell lung cancer [published online ahead of print 2006/12/26]. *Int J Radiat Oncol Biol Phys.* 2007;67(3):735-741.

56. Hsieh CH, Liu CY, Shueng PW, et al. Comparison of coplanar and noncoplanar intensity-modulated radiation therapy and helical tomotherapy for hepatocellular carcinoma [published online ahead of print 05/25]. *Radiation oncology (London, England).* 2010;5:40.

57. Yang W, Jones R, Lu W, et al. Feasibility of non-coplanar tomotherapy for lung cancer stereotactic body radiation therapy [published online ahead of print 07/07]. *Technology in cancer research & treatment.* 2011;10(4):307-315.

58. Papp D, Bortfeld T, Unkelbach J. A modular approach to intensity-modulated arc therapy optimization with noncoplanar trajectories [published online ahead of print 2015/06/18]. *Phys Med Biol.* 2015;60(13):5179-5198.

59. Velec M, Moseley JL, Dawson LA, Brock KK. Dose Escalated Liver Stereotactic Body Radiation Therapy at the Mean Respiratory Position. *Int J Radiat Oncol.* 2014;89(5):1121-1128.

60. Bisi MA, Selaimen CM, Chaves KD, Bisi MC, Grossi ML. Vestibular schwannoma (acoustic neuroma) mimicking temporomandibular disorders: a case report [published online ahead of print 12/01]. *Journal of applied oral science : revista FOB.* 2006;14(6):476-481.

61. Kaylie DM, Gilbert E, Horgan MA, Delashaw JB, McMenomey SO. Acoustic neuroma surgery outcomes [published online ahead of print 09/25]. *Otology & neurotology : official publication of the American Otological Society, American Neurotology Society [and] European Academy of Otology and Neurotology.* 2001;22(5):686-689.

62. Patel S, Nuno M, Mukherjee D, et al. Trends in surgical use and associated patient outcomes in the treatment of acoustic neuroma [published online ahead of print 06/23]. *World neurosurgery.* 2012;80(1-2):142-147.

63. Darrouzet V, Martel J, Enee V, Bebear JP, Guerin J. Vestibular schwannoma surgery outcomes: our multidisciplinary experience in 400 cases over 17 years [published online ahead of print 04/06]. *Laryngoscope.* 2004;114(4):681-688.

64. Jereczek-Fossa BA, Zarowski A, Milani F, Orecchia R. Radiotherapy-induced ear toxicity [published online ahead of print 09/16]. *Cancer treatment reviews.* 2003;29(5):417-430.

65. Combs SE, Engelhard C, Kopp C, et al. Long-term outcome after highly advanced single-dose or fractionated radiotherapy in patients with vestibular schwannomas - pooled results from 3 large German centers [published online ahead of print 02/24]. *Radiotherapy and oncology : journal of the European Society for Therapeutic Radiology and Oncology.* 2015;114(3):378-383.

66. De Marzi L, Feuvret L, Boulé T, et al. Use of gEUD for predicting ear and pituitary gland damage following proton and photon radiation therapy. *Br J Radiol.* 2015;88(1048).

67. Lunsford LD, Niranjan A, Flickinger JC, Maitz A, Kondziolka D. Radiosurgery of vestibular schwannomas: summary of experience in 829 cases [published online ahead of print 01/25]. *Journal of neurosurgery.* 2005;102 Suppl:195-199.

68. Hasegawa T, Kida Y, Kato T, Iizuka H, Yamamoto T. Factors associated with hearing preservation after Gamma Knife surgery for vestibular schwannomas in patients who retain serviceable hearing [published online ahead of print 10/04]. *Journal of neurosurgery.* 2011;115(6):1078-1086.

69. Ikonomidis C, Pica A, Bloch J, Maire R. Vestibular Schwannoma: The Evolution of Hearing and Tumor Size in Natural Course and after Treatment by LINAC Stereotactic Radiosurgery [published online ahead of print 11/17]. *Audiology & neuro-otology.* 2015;20(6):406-415.

70. Roos DE, Potter AE, Zacest AC. Hearing preservation after low dose linac radiosurgery for acoustic neuroma depends on initial hearing and time [published online ahead of print 07/12]. *Radiotherapy and oncology : journal of the European Society for Therapeutic Radiology and Oncology.* 2011;101(3):420-424.

71. Milligan BD, Pollock BE, Foote RL, Link MJ. Long-term tumor control and cranial nerve outcomes following gamma knife surgery for larger-volume vestibular schwannomas [published online ahead of print 12/20]. *Journal of neurosurgery.* 2011;116(3):598-604.

72. van der Putten L, de Bree R, Plukker JT, et al. Permanent unilateral hearing loss after radiotherapy for parotid gland tumors [published online ahead of print 06/20]. *Head Neck.* 2006;28(10):902-908.

73. Chen WC, Jackson A, Budnick AS, et al. Sensorineural hearing loss in combined modality treatment of nasopharyngeal carcinoma. *Cancer.* 2017;106(4):820-829.

74. Bhandare N, Antonelli PJ, Morris CG, Malayapa RS, Mendenhall WM. Ototoxicity after radiotherapy for head and neck tumors [published online ahead of print 01/24]. *International journal of radiation oncology, biology, physics.* 2007;67(2):469-479.

75. Hua C, Bass JK, Khan R, Kun LE, Merchant TE. Hearing loss after radiotherapy for pediatric brain tumors: effect of cochlear dose [published online ahead of print 04/09]. *International journal of radiation oncology, biology, physics.* 2008;72(3):892-899.

76. Pan CC, Eisbruch A, Lee JS, Snorrason RM, Ten Haken RK, Kileny PR. Prospective study of inner ear radiation dose and hearing loss in head-and-neck cancer patients [published online ahead of print 04/09]. *International journal of radiation oncology, biology, physics.* 2005;61(5):1393-1402.

77. Thomas C, Di Maio S, Ma R, et al. Hearing preservation following fractionated stereotactic radiotherapy for vestibular schwannomas: prognostic implications of cochlear dose [published online ahead of print 11/06]. *Journal of neurosurgery.* 2007;107(5):917-926.

78. Kano H, Kondziolka D, Khan A, Flickinger JC, Lunsford LD. Predictors of hearing preservation after stereotactic radiosurgery for acoustic neuroma [published online ahead of print 03/17]. *Journal of neurosurgery.* 2009;111(4):863-873.

79. Timmer FCA, Radboud University Nijmegen Medical Center DIfBC, Behavior DoOH, et al. Gamma knife radiosurgery for vestibular schwannomas: Results of hearing preservation in relation to the cochlear radiation dose. *The Laryngoscope.* 2016;119(6):1076-1081.

80. Foote KD, Friedman WA, Buatti JM, Meeks SL, Bova FJ, Kubilis PS. Analysis of risk factors associated with radiosurgery for vestibular schwannoma [published online ahead of print 09/22]. *Journal of neurosurgery.* 2001;95(3):440-449.

81. Arthurs BJ, Lamoreaux WT, Giddings NA, et al. Gamma Knife radiosurgery for vestibular schwannoma: case report and review of the literature [published online ahead of print 12/22]. *World journal of surgical oncology.* 2009;7:100.

82. Perks JR, St George EJ, El Hamri K, Blackburn P, Plowman PN. Stereotactic radiosurgery XVI: Isodosimetric comparison of photon stereotactic radiosurgery techniques (gamma knife vs. micromultileaf collimator linear accelerator) for acoustic neuroma--and potential clinical importance [published online ahead of print 11/25]. *International journal of radiation oncology, biology, physics.* 2003;57(5):1450-1459.

83. Plowman PN, Doughty D. Stereotactic radiosurgery, X: clinical isodosimetry of gamma knife versus linear accelerator X-knife for pituitary and acoustic tumours. *Clinical oncology.* 1999;11(5):321-329.

84. Rwigema JC, Nguyen D, Heron DE, et al. 4pi noncoplanar stereotactic body radiation therapy for head-and-neck cancer: potential to improve tumor control and late toxicity [published online ahead of print 12/09]. *International journal of radiation oncology, biology, physics.* 2014;91(2):401-409.

85. Yu VY, Landers A, Woods K, et al. A Prospective 4π Radiotherapy Clinical Study in Recurrent High Grade Glioma Patients [published online ahead of print 2018/04/06]. *International journal of radiation oncology, biology, physics.* 2018;101(1):144-151.

86. Kutcher GJ, Burman C. Calculation of complication probability factors for non-uniform normal tissue irradiation: the effective volume method [published online ahead of print

06/01]. *International journal of radiation oncology, biology, physics.* 1989;16(6):1623-1630.

87. Watanabe S, Yamamoto M, Kawabe T, et al. Stereotactic radiosurgery for vestibular schwannomas: average 10-year follow-up results focusing on long-term hearing preservation. *J Neurosurg.* 2016;125(Suppl 1):64-72.

88. Milligan BD, Pollock BE, Foote RL, Link MJ. Long-term tumor control and cranial nerve outcomes following gamma knife surgery for larger-volume vestibular schwannomas. *J Neurosurg.* 2012;116(3):598-604.

89. Yomo S, Arkha Y, Delsanti C, Roche PH, Thomassin JM, Regis J. Repeat gamma knife surgery for regrowth of vestibular schwannomas [published online ahead of print 12/04]. *Neurosurgery.* 2008;64(1):48-54; discussion 54-45.

90. Karunamuni R, Bartsch H, White NS, et al. Dose-Dependent Cortical Thinning After Partial Brain Irradiation in High-Grade Glioma [published online ahead of print 02/09]. *International journal of radiation oncology, biology, physics.* 2016;94(2):297-304.

91. RTOG 0825. Phase III double-blind placebo-controlled trial of conventional concurrent chemoradiation and adjuvant temozolomide plus bevacizumab versus conventional concurrent chemoradiation and adjuvant temozolomide in patients with newly diagnosed glioblastoma. *Radiat Ther Oncol Group.* 2014.

92. Karunamuni RA, Moore KL, Seibert TM, et al. Radiation sparing of cerebral cortex in brain tumor patients using quantitative neuroimaging [published online ahead of print 01/26]. *Radiotherapy and oncology : journal of the European Society for Therapeutic Radiology and Oncology.* 2016;118(1):29-34.

93. Nguyen D, Thomas D, Cao M, O'Connor D, Lamb J, Sheng K. Computerized triplet beam orientation optimization for MRI-guided Co-60 radiotherapy. *Medical Physics.* 2016;43(5667).

94. Gondi V, Pugh SL, Tome WA, et al. Preservation of memory with conformal avoidance of the hippocampal neural stem-cell compartment during whole-brain radiotherapy for brain metastases (RTOG 0933): a phase II multi-institutional trial [published online ahead of print 10/29]. *Journal of clinical oncology : official journal of the American Society of Clinical Oncology.* 2014;32(34):3810-3816.

95. Seibert TM, Karunamuni R, Bartsch H, et al. Radiation Dose-Dependent Hippocampal Atrophy Detected With Longitudinal Volumetric Magnetic Resonance Imaging [published online ahead of print 01/10]. *International journal of radiation oncology, biology, physics.* 2017;97(2):263-269.

96. van Hoof SJ, Granton PV, Verhaegen F. Development and validation of a treatment planning system for small animal radiotherapy: SmART-Plan [published online ahead of print 11/05]. *Radiotherapy and oncology : journal of the European Society for Therapeutic Radiology and Oncology.* 2013;109(3):361-366.

97. Wong J, Armour E, Kazanzides P, et al. High-resolution, small animal radiation research platform with x-ray tomographic guidance capabilities [published online ahead of print

07/22]. *International journal of radiation oncology, biology, physics.* 2008;71(5):1591-1599.

98. Butterworth KT, Prise KM, Verhaegen F. Small animal image-guided radiotherapy: status, considerations and potential for translational impact. *Br J Radiol.* 2015;88(1045).

99. Verhaegen F, Granton P, Tryggestad E. Small animal radiotherapy research platforms [published online ahead of print 05/28]. *Physics in medicine and biology.* 2011;56(12):R55-83.

100. *UCLA Center for Medical Countermeasures against Radiation (CMCR) - UCLA*. https://www.uclahealth.org/radonc/countermeasures-against-radiation.

101. Yu C, Luxton G. TLD dose measurement: a simplified accurate technique for the dose range from 0.5 cGy to 1000 cGy [published online ahead of print 08/07]. *Medical Physics.* 1999;26(6):1010-1016.

102. Davis SD, Ross CK, Mobit PN, Van der Zwan L, Chase WJ, Shortt KR. The response of lif thermoluminescence dosemeters to photon beams in the energy range from 30 kV x rays to 60Co gamma rays [published online ahead of print 12/05]. *Radiat Prot Dosimetry.* 2003;106(1):33-43.

103. Villarreal-Barajas JE, Khan RF. Energy response of EBT3 radiochromic films: implications for dosimetry in kilovoltage range [published online ahead of print 01/16]. *J Appl Clin Med Phys.* 2014;15(1):4439.

104. Barton MB, Jacob S, Shafiq J, et al. Estimating the demand for radiotherapy from the evidence: a review of changes from 2003 to 2012 [published online ahead of print 05/17]. *Radiotherapy and oncology : journal of the European Society for Therapeutic Radiology and Oncology.* 2014;112(1):140-144.

105. Harrington KJ, Billingham LJ, Brunner TB, et al. Guidelines for preclinical and early phase clinical assessment of novel radiosensitisers [published online ahead of print 2011/07/21]. *Br J Cancer.* 2011;105(5):628-639.

106. Hackam DG, Redelmeier DA. Translation of research evidence from animals to humans. *Jama.* 2006;296(14):1731-1732.

107. Liu FF, Okunieff P, Bernhard EJ, et al. Lessons learned from radiation oncology clinical trials [published online ahead of print 09/18]. *Clinical cancer research : an official journal of the American Association for Cancer Research.* 2013;19(22):6089-6100.

108. Stuben G, Landuyt W, van der Schueren E, van der Kogel AJ. Different immobilization procedures during irradiation influence the estimation of alpha/beta ratios in mouse lip mucosa [published online ahead of print 11/01]. *Strahlentherapie und Onkologie : Organ der Deutschen Rontgengesellschaft [et al]*. 1993;169(11):678-683.

109. Kitakabu Y, Shibamoto Y, Sasai K, Ono K, Abe M. Variations of the hypoxic fraction in the SCC VII tumors after single dose and during fractionated radiation therapy: assessment without anesthesia or physical restraint of mice [published online ahead of print 04/01]. *International journal of radiation oncology, biology, physics.* 1991;20(4):709-714.

110. Nikjoo H, Lindborg L. RBE of low energy electrons and photons [published online ahead of print 04/30]. *Physics in medicine and biology.* 2010;55(10):R65-109.

111. Chow JC, Leung MK, Lindsay PE, Jaffray DA. Dosimetric variation due to the photon beam energy in the small-animal irradiation: a Monte Carlo study [published online ahead of print 11/26]. *Medical Physics.* 2010;37(10):5322-5329.

112. Verhaegen F, van Hoof S, Granton PV, Trani D. A review of treatment planning for precision image-guided photon beam pre-clinical animal radiation studies [published online ahead of print 03/19]. *Zeitschrift fur medizinische Physik.* 2014;24(4):323-334.

113. Pidikiti R, Stojadinovic S, Speiser M, et al. Dosimetric characterization of an image-guided stereotactic small animal irradiator [published online ahead of print 03/30]. *Physics in medicine and biology.* 2011;56(8):2585-2599.

114. Nguyen D, Ruan D, O'Connor D, et al. A novel software and conceptual design of the hardware platform for intensity modulated radiation therapy [published online ahead of print 02/05]. *Medical Physics.* 2016;43(2):917-929.

115. Chambolle A, Pock T. A First-Order Primal-Dual Algorithm for Convex Problems with Applications to Imaging. *Journal of Mathematical Imaging and Vision.* 2011;40(1):120-145.

116. Pock T, Chambolle A. Diagonal preconditioning for first order primal-dual algorithms in convex optimization. Paper presented at: Computer Vision (ICCV), 2011 IEEE International Conference on2011.

117. Pock T, Cremers D, Bischof H, Chambolle A. An algorithm for minimizing the Mumford-Shah functional. Paper presented at: Computer Vision, 2009 IEEE 12th International Conference on2009.

118. Condat L. A Primal–Dual Splitting Method for Convex Optimization Involving Lipschitzian, Proximable and Linear Composite Terms. *Journal of Optimization Theory and Applications.* 2013;158(2):460-479.

119. Nguyen D, O'Connor D, Yu VY, et al. Dose domain regularization of MLC leaf patterns for highly complex IMRT plans [published online ahead of print 04/04]. *Medical Physics.* 2015;42(4):1858-1870.

120. Schaue D, McBride WH. Links between Innate Immunity and Normal Tissue Radiobiology. *Radiat Res.* 2010;173(4):406-417.

121. Huang XW, Yang J, Dragovic AF, Zhang H, Lawrence TS, Zhang M. Antisense oligonucleotide inhibition of tumor necrosis factor receptor 1 protects the liver from radiation-induced apoptosis [published online ahead of print 05/06]. *Clinical cancer research : an official journal of the American Association for Cancer Research.* 2006;12(9):2849-2855.

122. Dong P, Lee P, Ruan D, et al. 4π non-coplanar liver SBRT: a novel delivery technique. *International journal of radiation oncology, biology, physics.* 2013;85.

123. Van't Riet A, Mak AC, Moerland MA, Elders LH, van der Zee W. A conformation number to quantify the degree of conformality in brachytherapy and external beam

irradiation: application to the prostate. *International Journal of Radiation Oncology* Biology* Physics.* 1997;37(3):731-736.

124. Ashland Inc. *Efficient Protocols for Calibration and Dosimetry.* 2016.

125. Ma CM, Coffey CW, DeWerd LA, et al. AAPM protocol for 40-300 kV x-ray beam dosimetry in radiotherapy and radiobiology [published online ahead of print 07/07]. *Medical Physics.* 2001;28(6):868-893.

126. Tryggestad E, Armour M, Iordachita I, Verhaegen F, Wong JW. A comprehensive system for dosimetric commissioning and Monte Carlo validation for the small animal radiation research platform. *Physics in medicine and biology.* 2009;54(17):5341-5357.

127. Earl MA, Afghan MK, Yu CX, Jiang Z, Shepard DM. Jaws-only IMRT using direct aperture optimization [published online ahead of print 02/07]. *Medical Physics.* 2007;34(1):307-314.

128. Kim Y, Verhey LJ, Xia P. A feasibility study of using conventional jaws to deliver IMRT plans in the treatment of prostate cancer [published online ahead of print 04/04]. *Physics in medicine and biology.* 2007;52(8):2147-2156.

129. Mackie TR. History of tomotherapy [published online ahead of print 06/23]. *Physics in medicine and biology.* 2006;51(13):R427-453.

130. Reinhart AM, Nill S, Oelfke U. μIMRT on the SARRP using the motorised variable collimator. Paper presented at: Fourth International Conference on Precision Image-Guided Small Animal Radiotherapy Research2018; Lisbon, Portugal.

131. Liu Y, Shi C, Tynan P, Papanikolaou N. Dosimetric characteristics of dual-layer multileaf collimation for small-field and intensity-modulated radiation therapy applications [published online ahead of print 08/21]. *J Appl Clin Med Phys.* 2008;9(2):2709.

132. Giantsoudi D, Stathakis S, Liu Y, Shi C, Papanikolaou N. Monte Carlo Modeling and Commissioning of a Dual-layer Micro Multileaf Collimator [published online ahead of print 04/02]. *Technology in cancer research & treatment.* 2009;8(2):105-114.

133. Tangboonduangjit P, Metcalfe P, Butson M, Quach KY, Rosenfeld A. Matchline dosimetry in step and shoot IMRT fields: a film study [published online ahead of print 10/09]. *Physics in medicine and biology.* 2004;49(17):N287-292.

134. Boyer A, Biggs P, Galvin J, et al. *Basic Applications of Multileaf Collimators.* Madison, WI: Medical Physics Publishing;2001.

135. Ezzell GA, Burmeister JW, Dogan N, et al. IMRT commissioning: multiple institution planning and dosimetry comparisons, a report from AAPM Task Group 119 [published online ahead of print 12/10]. *Med Phys.* 2009;36(11):5359-5373.

136. Low DA, Harms WB, Mutic S, Purdy JA. A technique for the quantitative evaluation of dose distributions [published online ahead of print 06/03]. *Medical Physics.* 1998;25(5):656-661.

137. Noblet C, Chiavassa S, Smekens F, et al. Validation of fast Monte Carlo dose calculation in small animal radiotherapy with EBT3 radiochromic films [published online ahead of print 04/08]. *Physics in medicine and biology.* 2016;61(9):3521-3535.

138. Noblet C, Delpon G, Supiot S, Potiron V, Paris F, Chiavassa S. A new tissue segmentation method to calculate 3D dose in small animal radiation therapy [published online ahead of print 02/28]. *Radiation oncology (London, England).* 2018;13(1):32.

139. Casanova Borca V, Pasquino M, Russo G, et al. Dosimetric characterization and use of GAFCHROMIC EBT3 film for IMRT dose verification [published online ahead of print 03/09]. *J Appl Clin Med Phys.* 2013;14(2):4111.

140. Devic S, Seuntjens J, Sham E, et al. Precise radiochromic film dosimetry using a flat-bed document scanner [published online ahead of print 08/27]. *Medical Physics.* 2005;32(7):2245-2253.